Dissertation, Karlsruher Institut für Technologie (KIT)

Deformation of metallic multilayers: an atomistic study of the relationship between structure and deformation mechanisms.

Zur Erlangung des akademischen Grades
Doktor der Ingenieurwissenschaften
der KIT-Fakultät für Maschinenbau
Karlsruher Institut für Technologie (KIT)

genehmigte
Dissertation
von

Adrien Gola

Tag der mündlichen Prüfung: 15.01.2019
Hauptreferent: Prof. Dr. Peter Gumbsch
Korreferent: Prof. Dr. Lars Pastewka

Abstract

The mechanical properties of metallic multilayer materials differ from the bulk because of the properties of interfaces between the layers. These differences become greater as the layer thickness is reduced to the nanoscale. This thesis describes two FCC metallic multilayer materials, $Cu_{1-x}Ag_x$|Ni and Cu|Au stacked along their $[111]$ axis. These systems form semi-coherent interfaces with networks of partial Shockley dislocations arranged in a regular triangular pattern. The two systems represent two alternatives to fine tune the interfaces properties. The first one, the $Cu_{1-x}Ag_x$|Ni system, uses an alloying element, Ag, to fine tune the lattice mismatch between the layers. The second, the Cu|Au system, is a fully miscible binary system. As such the multilayer stack is a metastable form of the system inevitably leading to intermixing at the interface.

Molecular dynamics (MD) and a combination of molecular dynamics and Monte Carlo methods were used to study the structure and strengthening mechanism of these composite materials. Calculations were carried out on various geometries and loading conditions, from representative volume elements to realistic geometries such as nanopillar compression or nanoscratching setups. With the help of large scale MD calculations it was possible to reach system sizes directly comparable to experiments.

Ag was found to be a good candidate for alloying in the Cu|Ni binary system as it only forms a solid solution with Cu and therefore should only alter the Cu layers. As Ag was added to the Cu layer, it increased the lattice mismatch with the Ni layer, effectively increasing the density of the network of misfit dislocation at the interface. The excess of Ag in the Cu layer segregated at preferential sites at the interfaces and pinned the dislocation network. Molecular dynamics simulations demonstrated that these modifications increased the strength of the $Cu_{1-x}Ag_x$|Ni systems. This model shows that using a well chosen alloying element in a binary multilayer system is a route for tuning the strength of a system under various loading conditions.

A custom EAM potential for the Cu|Au system was developed and compared with pre-existing EAM potentials. This new potential allowed to successfully describe the unary as well as the stable binary phases existing for this binary system. Investigation of the interface of the Cu|Au system showed that the interface structure and properties were highly sensitive

to the intermixing between the two species, with a strong increase of the interface shear strength with intermixing. It was also noticed that this system was sensitive to defects and heterogeneities in its structure which lead, under tribological load, to the formation of vortex instabilities at the interfaces. Finally, catastrophic failure was observed of the system under compression as shear band nucleation was triggered by surface flaws. The observation and understanding of the effect of defects on the mechanical responses of multilayer systems can thus lead to a better material design by avoiding or embracing these defects.

Kurzfassung

Die mechanischen Eigenschaften von mehrlagigen metallischen Laminaten unterscheiden sich von homogenen Metallen, da diese durch die Eigenschaften der Grenzflächen zwischen den Schichten bestimmt werden. Der Einfluss der Grenzflächen steigt, wenn die Schichtdicke auf der Nanoskala reduziert wird. In dieser Arbeit werden die zwei mehrlagigen metallischen Materialien, $Cu_{1-x}Ag_x$|Ni und Cu|Au untersucht. Beide werden entlang der [111]-Achse ihrer kfz-Gitter gestapelt. Diese Systeme bilden semikohärente Grenzflächen mit Netzwerken von partiellen Shockley-Versetzungen, die in einem regelmäßigen Dreiecksmuster angeordnet sind. Die beiden Systeme bieten Alternativen zur Feinabstimmung der Grenzflächeneigenschaften. Das $Cu_{1-x}Ag_x$|Ni-System verwendet das Legierungselement Ag um die Gitterfehlanpassung präzise einzustellen. Das Cu|Au-System ist ein vollständig mischbares binäres System. Somit ist das Laminat eine metastabile Form des Systems, die zwangsläufig zu einer Mischung an der Grenzfläche führt.

Molekulardynamik (MD) und Monte-Carlo-Methoden wurden verwendet, um die Struktur und die mechanischen Eigenschaften dieser Verbundwerkstoffe zu untersuchen. Die Berechnungen wurden für verschiedene Geometrien und Belastungsbedingungen durchgeführt, von repräsentativen Volumenelementen bis hin zu realistischen Geometrien wie zum Beispiel der Kompression eines Nanopillars oder von Kratzversuchen auf Nanoebene. Mit Hilfe von großen MD-Berechnungen konnten Systemgrößen erreicht werden, die direkt mit Experimenten vergleichbar sind.

Ag bietet sich als Kandidat für die Legierung im Cu|Ni-Binärsystem an, da es lediglich in Cu löslich ist und daher nur die Cu-Schichten verändern sollte. Das Zulegieren von Ag zur Cu-Schicht erhöhte die Fehlanpassung des CuAg Gitters bezüglich des Ni-Gittern und erhöhte damit die Versetzungsdichte Grenzfläche. Der Überschuss an Ag in der Cu-Schicht fällt an bevorzugten Stellen des Versetzungsnetzwerks der Grenzfläche aus. Die Molekulardynamiksimulationen zeigten, dass diese Modifikationen die Stärke der $Cu_{1-x}Ag_x$|Ni-Systeme erhöhten. Dieses Modell zeigt, dass die Verwendung eines gut gewählten Legierungselements in einem binären Mehrschichtsystem ein Weg ist, um die Festigkeit des Systems unter verschiedenen Lastbedingungen einzustellen.

Für das Cu|Au-System wurde ein EAM-Potential entwickelt und mit bereits vorhandenen EAM-Potentialen verglichen. Dieses neue Potential ermöglicht es, sowohl die unären als auch die stabilen binären Phasen dieses Binärsystems erfolgreich zu beschreiben. Die Untersuchung der Grenzfläche des Cu|Au-Systems ergab, dass die Struktur und die Grenzfläche sehr empfindlich auf die Vermischung zwischen den beiden Spezies reagiert, wobei die Scherfestigkeit der Grenzfläche mit der Vermischung stark ansteigt.

Weitere Molekulardynamiksimulationen haben gezeigt, dass dieses System empfindlich auf Defekte und Heterogenitäten in seiner Struktur reagiert. So führt zum Beispiel tribologische Belastung zur Bildung von Wirbelinstabilitäten in dem Laminat und Oberflächenfehler können zur Bildung von Scherbändern und darauf folgendem katastrophalen Versagen der Strukturen führen. Die Beobachtung und das Verständnis der Wirkung von Defekten auf die mechanische Antwort von Mehrschichtsystemen kann somit zu einem besseren Materialdesign führen.

Dissemination

Journal publications based on the present dissertation.

- **Adrien Gola**, Peter Gumbsch, and Lars Pastewka, *Atomic-scale simulation of structure and mechanical properties of $Cu_{1-x}Ag_x|Ni$ multilayer systems*, Acta Mater. **150**, 236–247 (2018)
- **Adrien Gola**, and Lars Pastewka, *Embedded-atom method potential for studying mechanical properties of binary Cu-Au alloys*, Modelling Simul. Mater. Sci. Eng. **26**, 055006 (2018)
- **Adrien Gola**, Thomas Kreuter, Guang-Ping Zhang, Lars Pastewka, and Ruth Schwaiger, *Surface flaws control strain localization in the deformation of Cu|Au nanolaminates*, – manuscript in preparation
- **Adrien Gola**, Peter Gumbsch, and Lars Pastewka, *Fluid-like vortices of composite metals under tribological load*, – manuscript in preparation

Other journal publications unrelated to this dissertation.

- Andreas Klemenz, **Adrien Gola**, Michael Moseler, and Lars Pastewka, *Contact mechanics of graphene-covered metal surfaces*, Appl. Phys. Lett. **112**, 061601 (2018)
- Gianpietro Moras, Andreas Klemenz, Thomas Reichenbach, **Adrien Gola**, Hiroshi Uetsuka, Michael Moseler, and Lars Pastewka, *Shear melting of silicon and diamond and the disappearance of the polyamorphic transition under shear* – Accepted at Phys. Rev. Mater.

Book chapter.

- **Adrien Gola**, and Lars Pastewka, *Structure of interfaces in Cu|Au nanolaminates*, NIC Series **49**, 247 (2018)

Contributed talks to conferences.

- **Adrien Gola**, Peter Gumbsch, Lars Pastewka, *Tailored interfaces for high-performance nanolayered materials: $Cu_{1-x}Ag_x$|Ni nanolayers*, European Materials Research Society Fall meeting, Warsaw, Poland (Sept. 19, 2015)
- **Adrien Gola**, Lars Pastewka, *Molecular dynamics study of the interface strength of Cu|Au multilayer nanopillar systems*, Materials Research Society Spring meeting, Phoenix, United States (Apr. 1, 2016)
- **Adrien Gola**, Ruth Schwaiger, Lars Pastewka, *Molecular dynamics study of the interface strength of Cu|Au multilayer nanopillar systems*, 8th Multiscale Materials Modeling international conference, Dijon, France (Oct. 13, 2016)
- **Adrien Gola**, Peter Gumbsch, Lars Pastewka, *Combined Monte-Carlo/Molecular Dynamics study of the strength of $Cu_{1-x}Ag_x$|Ni multilayer*, European Materials Research Society Spring meeting, Strasbourg, France (May 23, 2017)

Contributed poster to conferences.

- **Adrien Gola**, Peter Gumbsch, Lars Pastewka, *Combined Monte-Carlo/Molecular Dynamics Study of the Strength of $Cu_{1-x}Ag_x$|Ni Multilayer Systems*, Materials Research Society Fall meeting, Boston, United States (Nov. 29, 2017)

Contents

Part I.

Introduction

1. Introduction

1.1 Motivation

Over the past decades the technological challenges have pushed research towards advanced engineered materials, such as thin films materials (Was and Foecke, 1996). Thin film materials exhibit a broad range of unique properties from mechanical to electrical, including tribological, thermal, magnetic or biological properties. Thanks to this wide range of characteristics associated with the large amount of possible material combinations, thin film materials are good candidates for numerous applications where a surface has to sustain severe conditions. Thin film materials can be found in application such as hard coatings, tribological contacts or micro-electro-mechanical systems (Clemens et al., 1999). The definition of thin film materials is broad and ranges from free standing films, to coatings and multilayers. The focus of this thesis will be on problems related to metallic multilayer materials, often called nanolaminates or nanolayered composites.

In nature, heterogeneous multilayered materials have existed for a long time, exhibiting for example high toughness in shell of mollusks (Currey, 1977). It has only been a few decades since a new class of materials composed of alternated metallic layers started to emerge. The first mention of such system was by Palatnik and Il'Inskii (1964). They found that the strength of laminated copper chromium was several times higher than that of a chromium bulk counterpart. Similarly, Koehler (1970) proposed guidelines to obtain a "strong solid". He outlined that such a "strong solid" should be made out of two thin crystals having similar lattice parameters and thermal expansion with dissimilar shear moduli to prevent dislocation transmission. Using these parameters he proposed Cu|Ni as a theoretical good candidate for such application. but it is only in the 1990's that metallic multilayered system have been considered and studied as the capacity to produce such system experimentally became viable (Was and Foecke, 1996). Simultaneously, the increase in computational power allowed scientist to use computational models to study similar systems (Allen and Tildesley, 2017, Dodson, 1988).

In this thesis, the mechanical properties and thermodynamic stability of metallic multilayers at the nanoscale will be investigated.

1.2 Mechanical properties of multilayered materials

Contrary to bulk composites, where the rule of mixtures can be applied to describe the mechanical properties, the unique mechanical properties of multilayered materials can be traced back to two interconnected factors, the reduction in layer thickness and the importance of interfaces in the system (Misra et al., 2004).

The impact of layer thickness reduction on the structure has first been observed for metallic monolayer in the 1960's and early 1970's. A linear scaling of the layer thickness with the average grain size, and a columnar growth of these grains have been observed for these metallic monolayers with thickness down to few hundreds of ångström (Smith et al., 1960, Donovan and Heinemann, 1971). Likewise, Adams et al. (1993) reported a similar linear scaling in metallic multilayer systems. As a consequence of the different grain size observed in different metallic monolayers, they follow the the well-known Hall-Petch relationship (Griffin et al., 1987, Venkatraman and Bravman, 1992). This relationship predicts a strengthening of a polycrystalline materials proportional to average grain diameter $\propto d^{-\frac{1}{2}}$ (Hall, 1951, Petch, 1953). Petch (1953) rationalized this relationship with the dislocation pile-up model. This model states that dislocations stored in a pile-up against a grain boundary generate a stress across the boundary lowering the critical stress barrier to overcome to generate dislocation in the neighboring grain. As dislocation pile-up are also seen at interfaces the Hall-Petch can be extended to metallic multilayer in this case the strengthening is proportional to the layer thickness $\propto \lambda^{-\frac{1}{2}}$ (Anderson and Li, 1995, Friedman and Chrzan, 1998, Misra et al., 1998). This scaling has been observed by Anderson et al. (1999) for Cu/Ni multilayer systems having a layer thickness going from more than 100 nm down to less than 20 nm. They observed deviations from this scaling below 20 nm. This deviation from the Hall-Petch relationship comes from the fact that at small layer thickness the grains (layers) can no longer store dislocation pile-ups. This scaling breaks down at small length scale (Misra et al., 1998).

When the number of dislocations in pile-ups become too small, the strengthening follows a confined layer slip (CLS) model that involve dislocation loops bounded by two interfaces. The strengthening in this CLS model is proportional to the inverse of the layer thickness along the dislocation slip plane (Anderson et al., 1999, Phillips et al., 2003). This model has been further refined by Misra et al. (2005) to take into account interface reactions as the former model was overestimating the strengthening for small λ and underestimating it for

large λ. In their refined CLS model the strengthening is proportional to $ln(\lambda/b)/\lambda$, with b being the Burgers vector of the dislocation. In their model Misra et al. (2005) took into account the interface response to the stress field of the dislocation as well as the interaction between dislocations already present at the interfaces (either deposited by another loop or misfit dislocations).

At even smaller scale, $\lambda \approx 1-2$ nm, the Hall-Petch and CLS models stop to describe the strength of a multilayer system. The strength of such multilayer system is determined by the interfacial barrier to slip transmission which is intrinsic to the materials composing the multilayer stack (Misra et al., 2005). Thus, from about $1-2$ nm and down to smaller scales, the strength does not depend on the layer thickness as long as interface structure remains stable.

The interface density in multilayered materials is extremely important. By design in multilayer systems the ratio between the interface area and the system volume is extremely large. The interface acts as buffer between the different materials ; it accommodates the property difference of these materials. As some examples of variations that can occur one can cite the accommodation of misfit in lattice constant, crystal structure variation or elastic modulus from one layer to the next (Was and Foecke, 1996, Misra et al., 1998, Clemens et al., 1999, Anderson et al., 1999, Misra and Krug, 2001, Wang and Misra, 2011, Gumbsch and Daw, 1991). Under deformation, the interfaces can as well act as a source, sink or barrier to dislocations (Hoagland et al., 2006). One of the first strengthening model proposed by Koehler (1970) made abstraction of the layer thickness and only involve difference of shear moduli resulting in an image force on the dislocation at the approach of the interface. The coherency stresses arising from accommodating the lattice mismatch is also a source of strengthening for multilayered materials as it create a stress fields near the interfaces that can either repel or attract incoming dislocations.

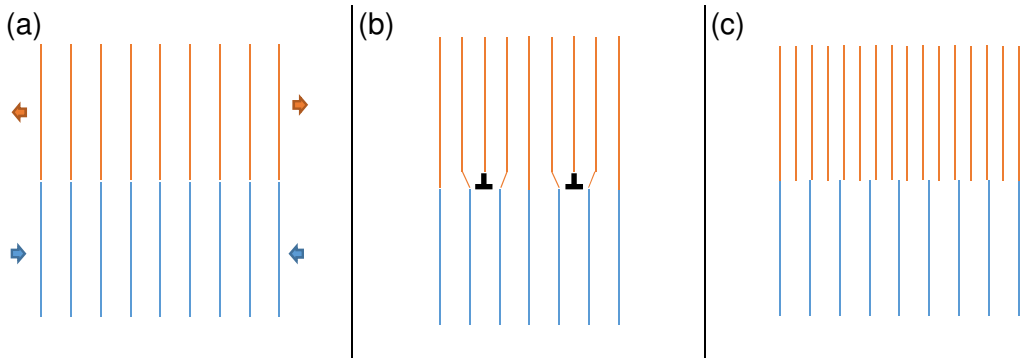

Figure 1.1: Schematic representation of the alignment of the crystallographic planes with the lattice mismatch. (a) coherent interface, (b) semi-coherent interface, (c) incoherent interface.

Up to now the interfaces have been considered as a flat plane of contact between two metals without considering their structure. Three types of interfaces can be distinguished in crystalline metallic multilayers, as shown in figure 1.1. These interfaces are sorted according to the degree of coherency across the interface. The first type of interfaces are the fully coherent ones (Fig. 1.1(a)), these interfaces show a continuity of the atomic planes across the interfaces between the two crystals. In this case the metal with the larger (smaller) lattice parameter experiences a compressive (tensile) strain to accommodate for the lattice mismatch. The lattice mismatch is here defined as

$$\delta_{12} = 2\frac{a_1 - a_2}{a_1 + a_2} \tag{1.1}$$

where a_1 and a_2 are the equilibrium lattice constants of each layer. These coherent interfaces are only possible for small lattice mismatch and up to a certain critical layer thickness. Indeed, for a given lattice mismatch the coherency strain energy increase with the layer thickness. This increase of energy determines a critical layer thickness after which the coherent interface is thermodynamically unfavorable (Frank and Merwe, 1949). The critical thickness is inversely proportional to the lattice mismatch (Matthews and Blakeslee, 1974). For example the critical thickness for Cu|Ni bilayer has been estimated and experimentally observed at around 2 nm (Hoagland et al., 2004, Liu et al., 2011).

The second kind of interfaces are the semi-coherent ones (Fig. 1.1(b)). They are observed for systems having layers of thickness greater than the critical thickness. In this case misfit dislocations are observed at the interface accommodating the lattice mismatch between the two crystal structures. In FCC/FCC systems for example, the misfit dislocations appear as a network grid with 90° junctions at (100) interfaces, or triangular network at close-packed (111) interfaces with dislocations split 120° apart (Cullen et al., 1973). The spacing between these misfit dislocations only depends on the lattice mismatch and the rotation angle between the two FCC crystals (Shao et al., 2013).

The third type of interfaces are incoherent interfaces (Fig. 1.1(c)). There is no correspondence of atomic planes across the interface in this case. This occurs if the lattice mismatch is too large or if the crystal structures are incompatible.

The structure of the heterointerface therefore depends on lattice parameters, and it is decisive for the control of the mechanical properties of these materials (Feng et al., 2017, Béjaud et al., 2018). These size effects can be exploited to design materials with mechanical strengths orders of magnitude larger than their bulk counterparts (Misra and Krug, 2001, Wang and Misra, 2011). To put it in a nutshell, at a given layer thickness, the mechanical properties of a multilayer system are strongly dominated by the interface structure. Therefore this thesis

will focus on investigating the possibilities to fine tune the interface properties and their stability as it is a key to design multilayered systems.

1.3 This thesis

The work described in this thesis was carried out as part of a Helmholtz-CAS (Chinese Academy of Science) joint research group. The research carried by the members of this group explores the possibility of tailoring metallic multilayered nano structures and the impact of such tailoring on their mechanical properties. With the aim of better understanding the relationship between structure and properties, this research could open the way to the development of application oriented multilayered materials. The work in this joint research group is carried in parallel using experimental and computational modeling techniques. The idea here is to use information coming from experimental samples to build and validate numerical models, and then use numerical simulations to shed some light on phenomena happening at length and time scales not yet accessible experimentally. This includes dislocation nucleation, the interfaces evolution under strain or segregation processes. The work presented in this manuscript is the computational modeling part of this joint project and employs atomic-scale modeling techniques, mainly molecular dynamics (MD) and Monte-Carlo (MC).

Two specific material systems have been studied in this thesis, Cu|Ni and Cu|Au. The difference between the two systems reside mainly in the lattice mismatch and the miscibility of the components. Using Eq. (1.1) with the experimental lattice constants of Cu, Ni and Au at 300 K (Massalski et al., 1990) gives $\delta_{CuNi} \approx 2.55\%$ and $\delta_{CuAu} \approx 12.05\%$.

While the Cu-Ni binary system shows a miscibility gap of up to 630 K (Fig. 1.2), the Cu-Au binary system is miscible at all concentrations and has stable intermetallic compounds, $CuAu_3$, CuAu and Cu_3Au (Fig. 1.3). The two multilayered systems have face centered cubic (FCC) structures and can be grown along their [111] axis when prepared experimentally (Tu and Berry, 1972, Schweitz et al., 2001). The interfaces of these structures are semi-coherent, exhibiting a triangular array of misfit dislocations with alternating FCC and hexagonal close packed (HCP) stacking regions (Fig. 1.5(a)). Theses regions are separated by a triangular network of Shockley partial dislocations (Fig. 1.5(b)) (Shao et al., 2013).

These systems represent two approaches to fine tune in a systematic manner the lattice mismatch and defects at the interfaces. This can shed light on the role of dislocations and defects at the interfaces for mechanical performance. As the density of the dislocation network depends directly on the mismatch in lattice parameter between the constituent

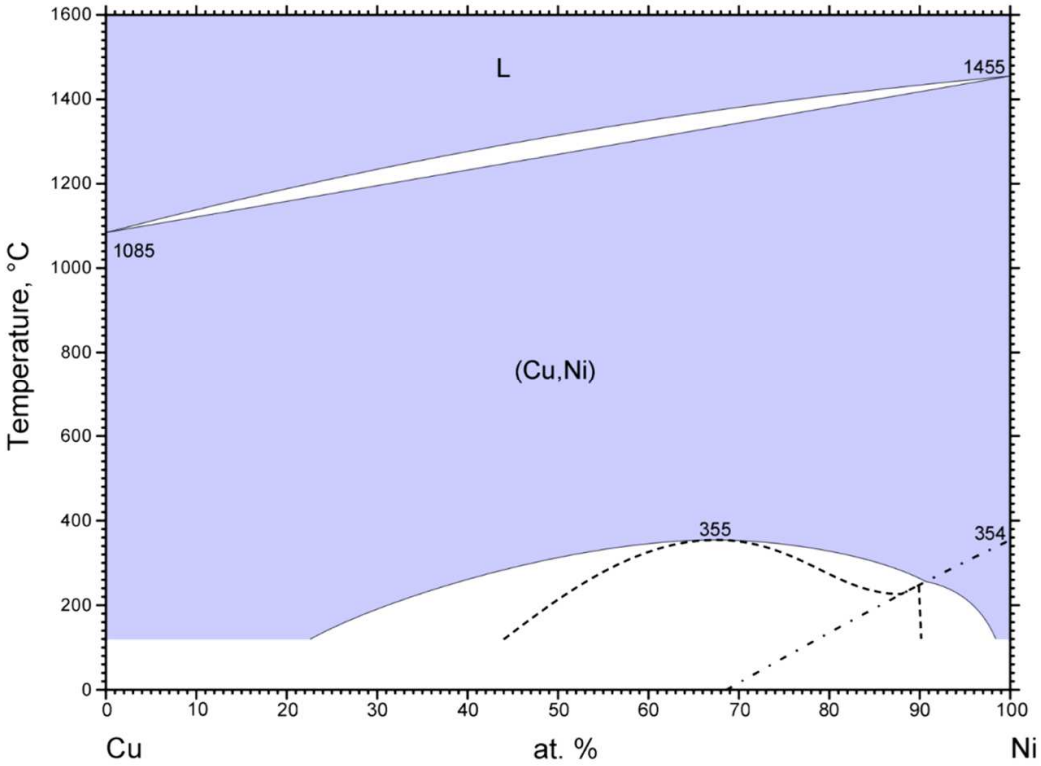

Figure 1.2: Experimental binary phase diagram of Cu-Ni (Massalski et al., 1990).

materials, alloying Ag to the Cu|Ni multilayer stack is an interesting option. Indeed, Ag is miscible with Cu (up to $x = 3\%$ in $Cu_{1-x}Ag_x$ at 1000 K, Fig. 1.4(a)) but not miscible with Ni (Fig. 1.4(b)). Therefore Ag will remain on the Cu side of the multilayer. Since the lattice parameter of $Cu_{1-x}Ag_x$ alloys is known to increase with increasing silver content (Madelung, 1991, Subramanian and Perepezko, 1993), alloying Ag to Cu could therefore be used to engineer the interface of the multilayer stack and thereby tune its mechanical properties. This proposition is probed here with atomic-scale calculations employing a combination of Monte-Carlo and molecular dynamics techniques.

For the Cu|Au system, fine tunning involves annealing the system to achieve intermixing at the interface and thus to smooth out the lattice mismatch over a finite interface region (Zhang, 2014). This system is particularly interesting experimentally for its strong contrast in electronic microscopy which allows to easily characterize the different layers (Goldstein et al., 2017).

In the next chapter the main numerical methods used for this thesis will be introduced. Then the effect of Ag and Cu-Au intermixing on the interface structure will be characterized. Finally, for each of the systems investigations will be carried out to determine how these structure changes affect their mechanical properties.

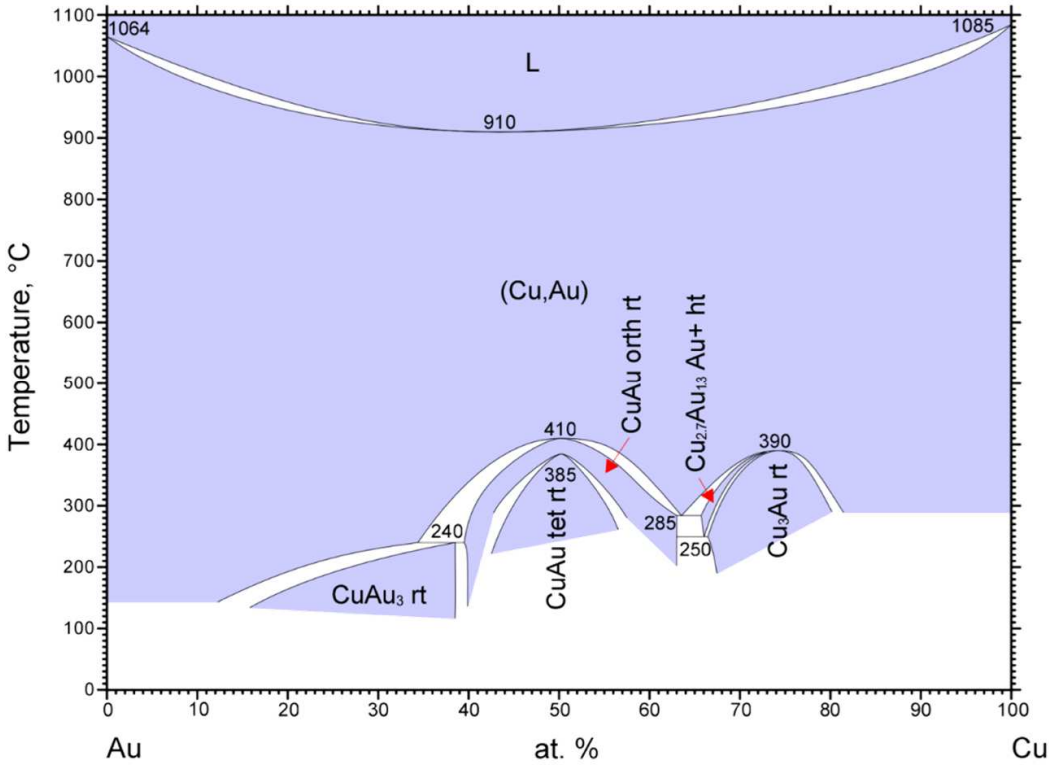

Figure 1.3: Experimental binary phase diagram of the Cu-Au (Massalski et al., 1990).

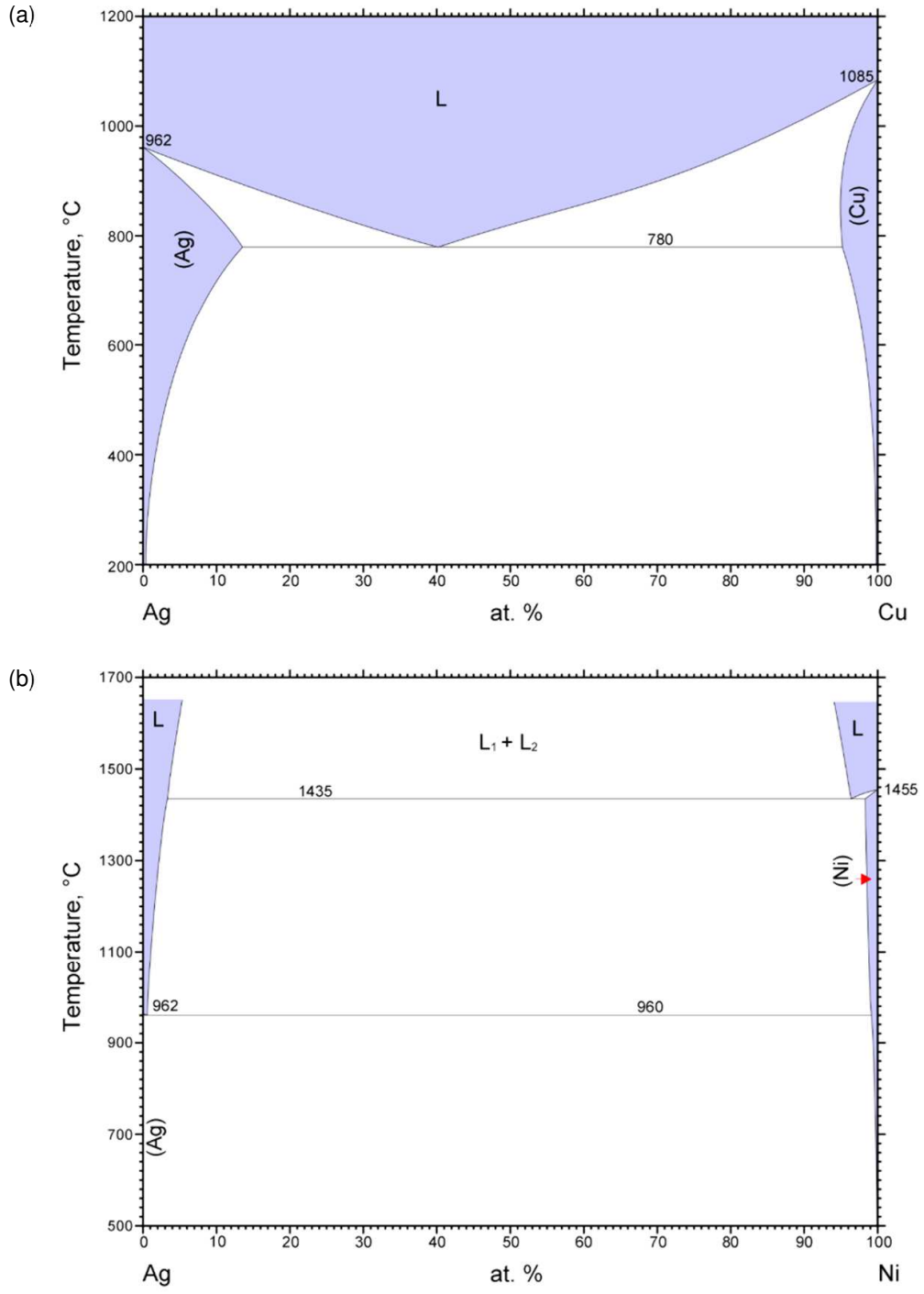

Figure 1.4: Experimental binary phase diagram of (a) Ag-Cu and (b) Ag-Ni (Massalski et al., 1990).

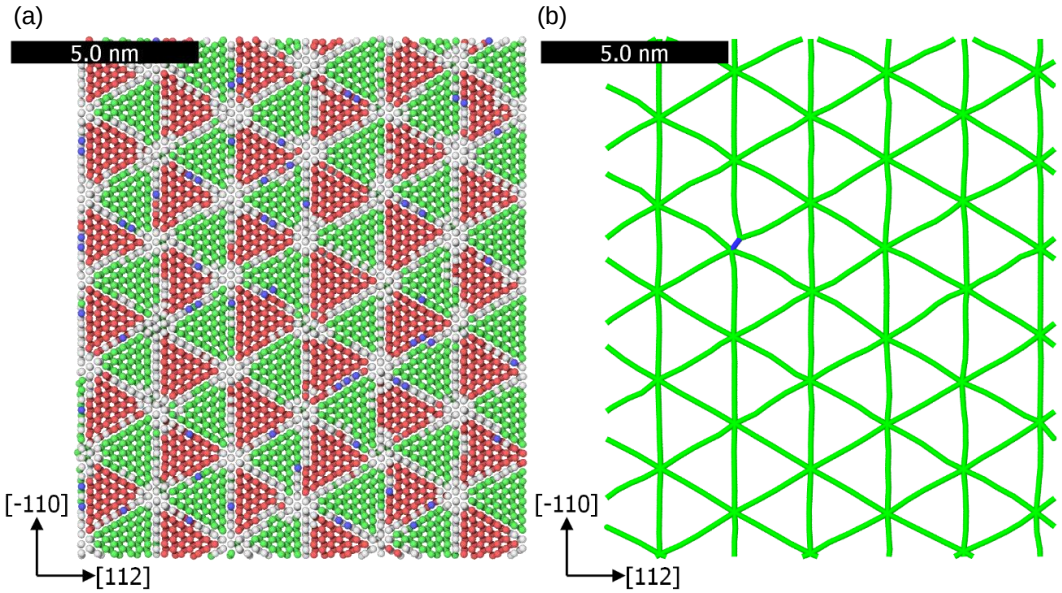

Figure 1.5: Molecular dynamic model of the Cu|Au $(111)/(111)$ interface showing (a) the local crystalline structure as determined by common neighbor analysis (Honeycutt and Andersen, 1987, Stukowski, 2012). Atoms in green are FCC, atoms in red are HCP, atoms in blue are BCC and atoms in white are in an undefined coordination structure. And (b) the network of misfit dislocation obtained with the dislocation extraction algorithm (Stukowski et al., 2012): Perfect dislocations are in blue, Shockley partials in green.

2. Methods

2.1 Interatomic potentials

Energies in MD are derived from models describing the interaction between atoms. The total potential energy $E_{\text{pot}}(\{\vec{r}_i\})$ of an atomistic system is a function of the positions of all atoms $\vec{r}_i$. Different models for E_{pot} exist, one of the most accurate description considers the electronic degrees of freedom explicitly (often involving the Born-Oppenheimer approximation), such as density functional theory (DFT). However, because of limitations in computational resources, in the early days of molecular dynamics the interatomic potentials consisted mainly of idealized pair potential. The interaction energy between two atoms in a pair potential solely depends on the distance between the atoms. A simple empirical example is the 12/6 Lennard-Jones potential shown in Eq. (2.1).

$$E^{\text{LJ}}(r) = 4\varepsilon\left(\left(\frac{\sigma}{r}\right)^{12} - \left(\frac{\sigma}{r}\right)^{6}\right) \tag{2.1}$$

This simple potential could be fitted to describe interaction between noble gas atoms. The attractive part of the functional of the form $-1/r^6$ has a physical origin in that it describes the Van der Waals interaction (mainly the London dispersion interaction (Israelachvili, 2011)) between two atoms with a negative energy well of depth ε. The term $1/r^{12}$ is on the other hand empirical, it correspond to a rapidly rising repulsive interaction at distance $r \approx \sigma$ mimicking the Pauli repulsion between two atoms. This last term is conveniently the square of the first term. This makes the Lennard-Jones potential a good candidate for efficient evaluation on computers.

The simplicity of these pair potentials comes with many limitations. They do not describe correctly the elastic constants of cubic crystals C_{11}, C_{12} and C_{44}. They predict a Cauchy pressure $C_p = C_{12} - C_{44}$ equal to zero and a Poisson's ratio exactly equal to 0.25. Theses limitations, while working to some extend for noble gas crystals, do not work for most of the

metals. Another limitation is the bad description of metallic atoms near a free surface (Gupta, 1981).

2.1.1. Embedded-atom method potentials

Due to the limitation of pair potentials and the increase of computational power some more complex and accurate "many-body" interatomic potentials were developed in the early 1980s. One of the most commonly used many-body interatomic potential for metals is the embedded atom method (EAM) (Daw and Baskes, 1984). The basic idea behind EAM potentials is to consider an atom in a solid as an impurity embedded in a matrix comprised of all the other atoms.

In the embedded atom method, the total energy of an atomic configuration is given by $E = \sum_i E_i$ with

$$E_i = F_{\sigma_i}(\rho_i) + \frac{1}{2}\sum_{j \neq i} \phi_{\sigma_i \sigma_j}(r_{ij}) \tag{2.2}$$

Here latin i, j denote atom indices and Greek σ_i, σ_j denote the species of atoms i and j, respectively. The symbol r_{ij} is the distance between two atoms, $r_{ij} = |\vec{r}_i - \vec{r}_j|$, where $\vec{r}_i$ denotes the position of atom i. The total energy then depends on the local density of atoms ρ_i through the "embedding" functional $F_\alpha(\rho)$. The heuristic rationale here is that the nucleus of atom i is embedded in a gas of nearly free electrons whose density depends on the density of atoms in the neighborhood of atom i, an argument which can be supported by quantum-mechanical considerations (Gupta, 1981, Cleri and Rosato, 1993, Tománek et al., 1985). The density is computed from

$$\rho_i = \sum_{j \neq i} f_{\sigma_i|\sigma_j}(r_{ij}) \tag{2.3}$$

where $f_{\sigma_i|\sigma_j}(r_{ij})$ is some function that drops to zero as $r_{ij} \to r_c$. The function $f_{\sigma_i|\sigma_j}(r_{ij})$ describes the contribution of an atom of species σ_j to the local density of an atom of species σ_i. Here, r_c is the range or cutoff radius of the embedded atom potential. The cutoff value in an EAM potential usually lie between the second and third nearest neighbor for a FCC crystal. This distance can be critical for FCC crystals to describe certain properties such as the stacking fault energies. The function $\phi_{\sigma_i \sigma_j}(r)$ in Eq. (2.2) is a pair-potential and symmetric with respect to exchange of the species σ_i and σ_j. The function $f_{\sigma_i|\sigma_j}(r)$ does not necessarily share this symmetry.

Most formulations of the embedded-atom method use an expression like Eq. (2.2). The major difference between different formulations is how the atomic species enter Eqs. (2.2) and

(2.3). For example, the widely used formulation of Daw & Baskes (Daw and Baskes, 1984) uses $f_{\sigma_i|\sigma_j}(r_{ij}) = f_{\sigma_j}(r)$, i.e. the contribution of atom j to the density of atom i depends only on the type σ_j on atom j and not on the type σ_i of atom i. The formulation given in Eqs. (2.2) and (2.3) is due to Finnis & Sinclair (Finnis and Sinclair, 1984). This latter formulation is employed in chapter 6 since it gives most flexibility.

2.1.2. Alloy-averaged interatomic potentials

In the case of an alloyed system it can be useful to reduce the stoichiometric degrees of freedom of a system, for example when studying properties sensitive to variation in chemical environment. Examples are solute energies or energy of a dislocation interacting with a single solute atom.

The averaged embedded atom method was first introduced by Smith and Was (1989) and then Varvenne et al. (2016). The potential energy of an alloy-averaged system can be defined within the embedded atom method framework. For a random solid solution one can define a set of occupation variables $\{s_i^\sigma\}$ where $s_i^\sigma = 1$ if atom i has type σ, otherwise it is equal to zero. Considering a system with N_T atom types, Eq (2.2) can be re-written as

$$E = \sum_i^N \sum_\sigma^{N_T} s_i^\sigma F^\sigma(\rho_i) + \frac{1}{2} \sum_{j \neq i}^N \sum_{\sigma_1,\sigma_2}^{N_T} s_i^{\sigma_1} s_j^{\sigma_2} \phi^{\sigma_1\sigma_2}(r_{ij}) \tag{2.4}$$

with the density defined as

$$\rho_i = \sum_{j \neq i} \sum_\sigma^{N_T} s_i^\sigma f^\sigma(r_{ij}) \tag{2.5}$$

Assuming a perfectly random solid solution, i.e. uncorrelated occupation variables, the averaged value $\left\langle s_i^{\sigma_1} s_j^{\sigma_2} \right\rangle$ can be simplified as $\left\langle s_i^{\sigma_1} \right\rangle \left\langle s_j^{\sigma_2} \right\rangle$ where $\left\langle s_i^{\sigma_1} \right\rangle$ correspond to the average concentration c^σ. One can now derive the configurational average of Eq. (2.4) as

$$E = \sum_i^N \sum_\sigma^{N_T} c^\sigma \left\langle F^\sigma(\rho_i) \right\rangle + \frac{1}{2} \sum_{j \neq i}^N \sum_{\sigma_1,\sigma_2}^{N_T} c^{\sigma_1} c^{\sigma_2} \phi^{\sigma_1\sigma_2}(r_{ij}) \tag{2.6}$$

In order to further simplify Eq. (2.6), one need to introduce the main approximation of the alloy-averaged method by expanding the embedding function in a Taylor series around the average electron density $\langle \rho_i \rangle$ as

$$\langle F^{\sigma}(\rho_i) \rangle = F^{\sigma}(\langle \rho_i \rangle) + F'^{\sigma}(\langle \rho_i \rangle)(\rho_i - \langle \rho_i \rangle) + O(\rho_i - \langle \rho_i \rangle)^2 \tag{2.7}$$

Due to averaging the first order term in Eq. (2.7) vanishes. And by neglecting the second order term in Eq. (2.7) one can now write

$$E = \sum_{i}^{N} F^{\alpha}(\langle \rho_i \rangle) + \frac{1}{2} \sum_{j \neq i}^{N} \phi^{\alpha\alpha}(r_{ij}) \tag{2.8}$$

$$\begin{aligned} \text{with } F^{\alpha}(\langle \rho_i \rangle) &= \sum_{\sigma}^{N_T} c^{\sigma} F^{\sigma}(\langle \rho_i \rangle), \\ \langle \rho_i \rangle &= \sum_{i}^{N} \sum_{\sigma}^{N_T} c^{\sigma} \rho_i^{\sigma}, \\ \phi^{\alpha\alpha}(r_{ij}) &= \sum_{\sigma_1, \sigma_2}^{N_T} c^{\sigma_1} c^{\sigma_2} \phi^{\sigma_1 \sigma_2}(r_{ij}). \end{aligned} \tag{2.9}$$

Equation (2.8) has the form of an EAM potential for an average-atom of type α. This average atom represents a new species having the average properties of a random alloy.

In chapter 3, this method is used to compute the energetics of single Ag atoms within a $Cu_{1-x}Ag_x$ matrix. The method introduces an alloy-averaged EAM potential that describes the mean interaction between averaged $\langle Cu_{1-x}Ag_x \rangle$ atoms and hence introduces a single synthetic atom type for the random alloy. This synthetic atom type homogenizes the structural disorder of the alloy while still faithfully reproducing energy differences and hence eliminate sampling thousands of disordered configurations. The solute energy of single Ag atoms in a matrix of average-atom $\langle Cu_{0.90}Ag_{0.10} \rangle$ is computed in order to study the Ag's energy at the interface at different point of interests (i.e along dislocation lines, dislocation nodes) in chapter 3.

Recent work employing thermodynamic integration along alchemical mutation of random alloys into average-atom solids (Nöhring and Curtin, 2016) have shown that free-energy differences between the true random alloy and the average-atom solid are on the order of $\sim 10\,\text{meV}$ at $300\,\text{K}$. Similar corrections are expected to apply for the energy differences

computed in this work. All energies obtained here with the average-atom potential method are at least an order of magnitude larger than this energy scale. Conclusions drawn from these calculations therefore still apply to free energies, where these corrections must be taken into account.

2.2 Molecular dynamics

Molecular dynamics is used in this thesis to describe the dynamical behavior of the systems under external load. Molecular dynamics allow to describe the evolution of a given configuration in time and in the phase space. This set of data build a so-called trajectory of the N-particles of a system. The interactions between particles are modeled using interatomic potentials (also called force fields) described in the previous section 2.1. In molecular dynamics the N-particles of a configuration move according to Newton's equations of motion. The integration in MD give the information on the position, velocity of the system at a time $t + \Delta t$. These information are usually obtained using the velocity Verlet algorithm that uses Taylor expansions at $t + \Delta t$. The time step Δt must be small enough so that the derivative can be approached by finite difference approximations. A good approximation for Δt is some order of magnitude lower than the atomic vibration (Howe, 1997). For a metal this is typically a few femtoseconds. At the date of the writing of this thesis this allow for a maximum time calculation in the order of the nanoseconds for systems of up to millions of atoms using an EAM potential. Indeed, this thesis describes calculations of up to 400 million atoms, among the biggest calculations carried out to date.

The aforementioned method let the system evolve in the N, V, E ensemble. However performing calculations at fixed temperature is possible by coupling the simulation cell to an external heat bath. Similarly fixed pressure calculation can be done by rescaling the periodic boundaries and the atomic positions of a system (Shinoda et al., 2004, Berendsen et al., 1984, Schneider and Stoll, 1978). All these techniques are fairly standard and described in many text books (Allen and Tildesley, 2017) and their details will not be repeated here.

2.3 Monte Carlo

2.3.1. Metropolis Monte Carlo

In part II the multilayer system is composed of Cu, Ni and Ag. As described in the introduction Ag is used there as a solute in the Cu layer. The atomic inter-diffusion in an

alloy has a high energy barrier. This means that it requires a long time in order to statistically occur. As mentioned in section 2.2, the timescale accessible with classical MD is too short to relax the system to its thermodynamic equilibrium by purely dynamical means when starting from a random solid solution structure. Practically this mean that MD can only model a metastable configuration of a solid which might not reflect an experimental setup.

Another path to study atomistic models is the Monte Carlo (MC) method (Binder and Heermann, 2002). One well known MC algorithm was presented by Metropolis et al. (1953). In this article Metropolis proposed a technique where the atoms carry out random displacements that are accepted given the probability $A_c = \min\{1; \exp[-\Delta E/k_B T]\}$. This lead to a set of configurations that sample the Boltzmann distribution. Contrary to MD method that is in most flavors deterministic, MC methods use (usually) unphysical displacements that sample the configuration space in a manner that allow to compute equilibrium properties.

Later on Kikuchi et al. (1991, 1992) showed that the Metropolis algorithm could also be used to study dynamic properties, which allowed to combine it with a MD method to circumvent the time limitation inherent to this method. A MC/MD method has been used in this thesis to bring the systems closer to their thermodynamic equilibrium with a sequential algorithm that alternates MD and MC sequences (Neyts and Bogaerts, 2013). The idea here is that the MD runs are perfectly suited to simulate fast processes such as local stress relaxation, while the MC runs can account for slower processes i.e. atomic diffusion.

2.3.2. Atom-swap Monte Carlo

During the MC runs atom swap trial moves within the metropolis algorithm (Metropolis et al., 1953) have been used. One MC step consist of :

1. Picking two random atoms of types σ_i, σ_j with $\sigma_i \neq \sigma_j$. In a system having an energy E_0
2. Swapping their types and rescaling their velocities to conserve the kinetic energy.
3. Computing the new energy E_1 and accepting the move with the probability $A_c = \min\{1; \exp[-\Delta E/k_B T]\}$ where k_B is the Boltzmann's constant and T is the calculation temperature.

With this algorithm, atoms are picked and swapped within the system which means that the system is bound to evolve at fixed composition.

2.3.3. Parallel variance-constrained semi-grand canonical ensemble Monte Carlo

This method is described in detail by Sadigh et al. (2012). What follows is a short overview of the method and its advantages.

One technical limitation of the previously described Monte Carlo methods is the lack of efficient parallelization (Frenkel and Smit, 2002). This limitation is quite critical when it comes to model system with millions of particles. The bottleneck comes from the fact that in the atom-swap ensemble the number of atoms in the system is fixed, thus trial steps are performed by randomly picking atom pairs in the full simulation volume. Technically the simulation volume is split in sub-volumes spread on the parallel processors. This means that the parallel processors are not independent with regards to performing local trial move and energy change evaluation.

In order to make all the trial events independent from each other one has to switch to the semi-grand canonical (SGC) statistical ensemble where the number of particles is fixed but the relative concentration of the species can vary. This corresponds to a system in a contact with an infinite reservoir, in this case independent trial moves can be envisioned as an atom swap to and from the infinite reservoir. In order to limit concentration fluctuation the authors in Sadigh et al. (2012) used a subset of the SGC ensemble called the variance-constrained SGC (VC-SGC) where two parameters ϕ and κ are used to constrain the fluctuations of concentration around a targeted value c_0. In this case the system can be seen as in contact with a finite reservoir.

Due to the parallelization of the VC-SGC method, one has to perform a composite trial move split in two steps to satisfies detailed balance. Step 1 consists of N_{CPU} synchronous moves, with one move localized on each processor i, where one particle is randomly selected and its type is swapped, each move is accepted with the probability

$$A_v^{loc}(i) = \min\{1; \exp[-(\Delta E_i + N\Delta c_i(\phi + 2\kappa N c_0))/k_B T]\} \tag{2.10}$$

where ΔE_i and Δc_i are the local energy and concentration changes, respectively. Step 2 is a global move that considers the swaps that were accepted during step 1 and accept all of them together with the probability

$$A_v^{glob} = \min\left\{1; \exp\left[-(\kappa N^2 \Delta c_{tot}\left\{\Delta c_{tot} - 2[\hat{c}(\sigma^N) - c_0]\right\})/k_B T\right]\right\} \tag{2.11}$$

where Δc_{tot} is the total change in concentration and $\hat{c}(\sigma^N)$ the concentration of the system state σ^N.

The outcome of these two methods have been compared, atom-swap and variance constrained MC, on a CuAg|Ni bilayer system in appendix A

2.4 Nested Sampling

While the number of available interatomic potentials has grown since the 1980s, it is still a complex task to obtain a transferable interatomic potential that can fully describe a material system, e.g. its thermodynamic properties, mechanical properties, diffusion properties, etc. In the case of a missing feature in the available interatomic potentials, it might be useful to create a new one to fit specific needs. EAM potentials can be fitted to targeted properties defined experimentally or via ab-initio calculations such as cohesive energy, lattice constants, elastic constants. Nowadays, these properties can rapidly be computed in order to enter in an optimization procedure. This allows to fit EAM mathematical functions.

Thermodynamic data is more difficult to obtain in such a stream-lined fashion. For example accessing the melting temperature of one single composition via the voids methods (Solca et al., 1997) or the melt-crystal equilibrium (Morris et al., 1994) requires careful calculations setup and statistical sampling (Zhang and Maginn, 2012). This is a particular cumbersome task for binary alloys where the composition has to be varied.

In order to test effectively thermodynamic properties of EAM potentials a nested sampling (NS) algorithm (Skilling, 2004, 2006, Pártay et al., 2010, 2014, Baldock et al., 2016) has been used to compute the temperature/composition phase diagram of the binary Cu-Au system in part III. This algorithm is of particular interest for thermodynamics of complex systems as it is independent of temperature, i.e. thermal sensitive properties are obtained during a post processing step and not during the actual calculation. Additionally, it does not rely on any prior knowledge on the system, thereby yielding results unbiased by the researcher that in some method (such as obtaining the melting point from melt-crystal equilibration) has to input guesses for the stable phases and transition temperatures.

In brief, the NS algorithm directly constructs the phase-space volume $\chi(H)$ as a function of enthalpy H. Considering the partition function of a system at constant pressure composed of N particles of mass m

$$Z(N,P,\beta) = \frac{\beta P}{N!}\left(\frac{2\pi m}{\beta h^2}\right)^{3N/2}\int dH \frac{\partial \chi}{\partial H} e^{-\beta H}, \tag{2.12}$$

where h is Planck's constant, $\frac{\partial \chi}{\partial H}$ the density of states and $\beta = 1/k_B T$. One can approximate it as

$$Z(N,P,\beta) \approx \frac{\beta P}{N!}\left(\frac{2\pi m}{\beta h^2}\right)^{3N/2} \sum_i (\chi_{i-1} - \chi_i)\, e^{-\beta H_i} \tag{2.13}$$

with a set of suitably chosen configuration i. As described below, the NS algorithm provides just such a series of configuration i of decreasing enthalpy, H_i. Each of these enthalpies are bound to a volume of configuration space χ_i nested in the volume χ_{i-1}. Once the partition function is known, thermodynamic properties can easily be computed, e.g. heat capacity :

$$C_P(T) = -k_B \beta^2 \frac{\partial \langle H \rangle}{\partial \beta} \text{ , with } \langle H \rangle = -\frac{\partial \ln(Z)}{\partial \beta} \tag{2.14}$$

where $\langle H \rangle$ is the expected value of the enthalpy. Peaks within $C_p(T)$ indicate phase transitions. These peaks can be fitted with Gaussians. This yields the transition temperatures and a measure for their error.

An NS run starts with K random phase-space configurations uniformly distributed within the phase-space volume bounded by the enthalpy H_0. The K random configurations are initially constrained to have a cell volume smaller than V_0, corresponding to a volume where the system can be assimilated to an ideal gas. This represents a total configuration space χ_0. After this initialization the algorithm execute the following loop:

1. Record and discard the n-th configuration with the highest enthalpy H_n, set $H_{\text{limit}} = H_n$. Since all H_K cover phase space (up to H_{limit}) uniformly, discarding the configuration with the highest enthalpy H_{limit} leads to $K-1$ remaining configurations that cover a phase space volume approximately $K/(K+1)$ smaller than the initial one.

2. An additional configuration k is then added to the $K-1$ configurations by cloning one of the a random $K-1$ remaining configurations and propagating it using a combination of molecular dynamics (Burkoff et al., 2016) and Markov chain Monte Carlo steps with the constraint $H_k < H_{limit}$.

3. return to step (1) or exit the loop if a convergence criteria has been reached (number of iterations, effective temperature threshold).

This generates a series of decreasing enthalpy values H_i with corresponding phase space volumes $\chi_i = \chi_0[K/(K+1)]^i$, which constitutes a discretization of $\chi(H)$.

2.5 Molecular Dynamic trajectory post-processing

In this section the post-processing methods used in this thesis are described. All of these methods are implemented in the Open Visualization Tool (OVITO), a powerful and widespread software for the visualization and analysis of atomistic calculations (Stukowski, 2010).

2.5.1. Local structure analysis

The local crystalline structures is primarily analyzed using the common neighbor analysis (CNA) as invented by Honeycutt and Andersen (1987) and extended by Stukowski (2012). This method analyses the bonds between nearest neighbors. For each atom the bonds are determined using a given cutoff radius. The extension developed by Stukowski (2012) determines automatically the optimal cutoff radius for each particle. For one central atom the algorithm determines for each pair formed with one of the N nearest neighbors the number of common neighbors the two atoms share, the total number of bonds between these common neighbors and lastly the longest chain of bonds connecting the common neighbors. These $N \times 3$ numbers correspond to a specific signature for each local crystalline structure.

More recently, the polyhedral template matching (PTM) method was developed by Larsen et al. (2016). This method is more reliable than the CNA, especially when dealing with small crystal distortions caused by thermal vibrations. This method contrary to the CNA does not rely on atomic bonds, instead for each atom it computes the convex hull formed by the nearest neighbors. The nearest neighbors for each of the local structures (simple cubic, BCC, FCC, HCP, icosahedral) form a particular polyhedron that can be stored in some database. The algorithm then compares the computed convex hull to the one in the database to assign to each atom a local structure. Through the identification process the PTM method analyses the lattice orientation for each atom as well as the alloy structures (e.g. $L1_0$ or $L1_2$ for FCC).

2.5.2. Dislocation extraction algorithm

The dislocation extraction algorithm (DXA) was used throughout this thesis to identify dislocations and their Burgers vectors. This algorithm counts and classifies the dislocations

present in the systems. This method, developed by Stukowski et al. (2012), extracts dislocations information solely from the atomic positions of an MD trajectory. In order to locate the dislocation lines, the algorithm is based on the principle that the local structure inside the core of dislocation differs from the one in a perfect crystal. These two type of regions in the system can be qualified as "good" and "bad" crystals. To identify the "good" and "bad" crystals the algorithm first uses the CNA. Then based on the principle defined by Frank (1951), a Burgers circuit must not cross a "bad" crystal region, the algorithm creates a surface mesh between the "good" and "bad" regions on which Burgers circuits can be build for each dislocation.

2.5.3. Local atomic strain analysis

In order to quantify elastic and plastic rearrangements rather than defects (that are the carriers of plasticity that may disappear at sinks), it is possible to compute the local strain tensor from the analysis of Falk and Langer (1998) within local neighbor spheres of radius that include just an atom's nearest neighbors. This techniques computes the atomic neighborhood in a reference frame and then extracts the deformation gradient tensor $\mathbf{F}$ necessary to transform the vectors connecting the atom of interest to its reference neighborhood to the deformed configuration in a least-squares sense. Then from the deformation gradient the local Green-Lagrangian strain tensor is computed (Shimizu et al., 2007), $\gamma = (\mathbf{F}^T\mathbf{F} - \mathbf{I})/2$. With this method one can visualize the total amount of local deformation a system has experienced, i.e. where dislocations have slipped.

Part II.

$Cu_{1-x}Ag_x|Ni$ multilayer systems

3. Monocrystalline layers: Structure

3.1 Introduction

This part will focus on the study of metallic multilayer systems composed of two FCC metals, a $Cu_{1-x}Ag_x$ alloy with $x = 0\%, 5\%, 10\%$ and Ni. Here, Ag is used as a way to fine tune the lattice mismatch between two layers of FCC metals. First the structure of such multilayer system and the effect of Ag on this structure is investigated, with a focus on the interfaces. The structure will be compared in both monocrystalline and polycrystalline setup. Once the equilibrium structure is properly defined the mechanical impact of Ag alloying in the Cu|Ni system will be studied.

In this chapter Monte Carlo and classical molecular dynamics methods are used to equilibrate the structure close to the thermodynamic equilibrium of such mono crystalline bilayer. The material system is based on the Cu|Ni multilayer that has been widely studied experimentally and theoretically (Rao and Hazzledine, 2000, Misra and Krug, 2001, Hoagland et al., 2002, Mastorakos et al., 2011, Liu et al., 2011, Chen et al., 2012, Yan et al., 2013a, Shao et al., 2013).

3.2 Methods

3.2.1. Interatomic potential

A ternary Cu-Ni-Ag embedded atom method (EAM) potential was employed to model the multilayer system (Zhou et al., 2004). To characterize the applicability of the potential to mechanical deformations, the stacking faults in the three phases are computed. Following standard procedures (Zimmerman et al., 2000), the properties of stacking faults are computed by continuously displacing two blocks of a crystalline system, separated by a $\{111\}$ plane, rigidly along the $[112]$ direction. The systems had periodic boundaries along the $[112]$ and $[\bar{1}10]$ directions and a free boundary along the $[\bar{1}\bar{1}1]$ direction. After each rigid displacement,

Table 3.1: Stacking fault energies γ_{SF} for Cu, Ni and Ag computed with the ternary EAM potential by Zhou, Wadley and Johnson (Zhou et al., 2004) used in the present work. Results obtained with the classic ternary EAM potential by Daw, Baskes and Foiles (Foiles et al., 1986) and by experiments (Carter and Ray, 1977, Carter and Holmes, 1977, Li et al., 2011) are given for reference.

γ_{SF} (mJ m^{-2})	Cu	Ni	Ag
Experimental	45	144	16
Zhou, Wadley and Johnson	23	99	6
Daw, Baskes and Foiles	18	15	2

the potential energy of the system was minimized by allowing the atoms to move along the $[\bar{1}\bar{1}1]$ axis until the norm of the force vector falls below 10^{-8} eV Å^{-1}.

Table 3.1 shows calculated values of stacking fault energies in comparison with experimental values. Stacking fault energies are consistently lower than the corresponding experimental values. Energies are underestimated by about $1/2$ for pure face-centered cubic (FCC) phase of Cu and by $1/3$ for Ni, and about a third of the experimental value is found for Ag. Even though this deviation of stacking fault energies from experiment is important for Ag, the Zhou et al. potential (Zhou et al., 2004) gives stacking fault energies in the correct order of magnitude and relative order. Moreover, the calculations will only include Ag in solid solution or segregated in small clusters. This deviation in Ag bulk properties should therefore have a negligible impact on the final results. To put these numbers into context, the widely used ternary EAM potential by Daw, Baskes and Foiles (Foiles et al., 1986) underestimates the stacking fault energies much more dramatically (see Tab. 3.1).

3.2.2. Multilayer system

The multilayer cell used in the simulations is shown in Fig. 3.1 with x-, y- and z-axes oriented along the $[112]$, $[\bar{1}10]$ and $[\bar{1}\bar{1}1]$ directions, respectively. The simulation cell is periodic in all directions and consists of two crystals of $Cu_{1-x}Ag_x$ and Ni with a layer thickness of approximately 6nm in the $[\bar{1}\bar{1}1]$ direction. The lateral cell size needs to be commensurate with the lattice constant of both, $Cu_{1-x}Ag_x$ solid solution (lattice constants $a_{Cu} = 3.65$ Å to $a_{Cu_{0.90}Ag_{0.10}} = 3.71$ Å at 300 K, Fig. 3.2) and Ni ($a_{Ni} = 3.53$ Å), phases. The nominal mistmatch δ between the two phases and the residual mismatch $\Delta\varepsilon$ between two crystalline supercells can be defined as (Gumbsch, 1992)

$$\delta = \frac{2(a_{Cu_{1-x}Ag_x} - a_{Ni})}{a_{Cu_{1-x}Ag_x} + a_{Ni}}, \Delta\varepsilon = \frac{2(na_{Cu_{1-x}Ag_x} - ma_{Ni})}{na_{Cu_{1-x}Ag_x} + ma_{Ni}}, \tag{3.1}$$

where n and m are the numbers of unit cells of the $Cu_{1-x}Ag_x$ and Ni supercells that constitute the individual layers in the multilayer stack. The choice of simulation cell size minimizes $\Delta\varepsilon$ while keeping the overall size small enough for the simulation methods. The final simulation cells have $n/m = 29/30$ for Cu|Ni, $23/24$ for $Cu_{0.95}Ag_{0.05}$|Ni and $19/20$ for $Cu_{0.90}Ag_{0.10}$|Ni. Such different unit cell ratios reflect the difference in the density of the misfit dislocation network, manifested in an increase in interface energy with misfit (see e.g. Gumbsch (1992)). Table 3.2 reports the exact number of unit cells and the resulting residual misfits. These ratios depend on Ag content because increasing Ag content changes the lattice constant of the CuAg solid solution. It therefore also changes the misfit of the interface (see Fig. 3.2). Note that the chosen layer thickness of 6 nm can readily be realized in experiments (Mitlin et al., 2004).

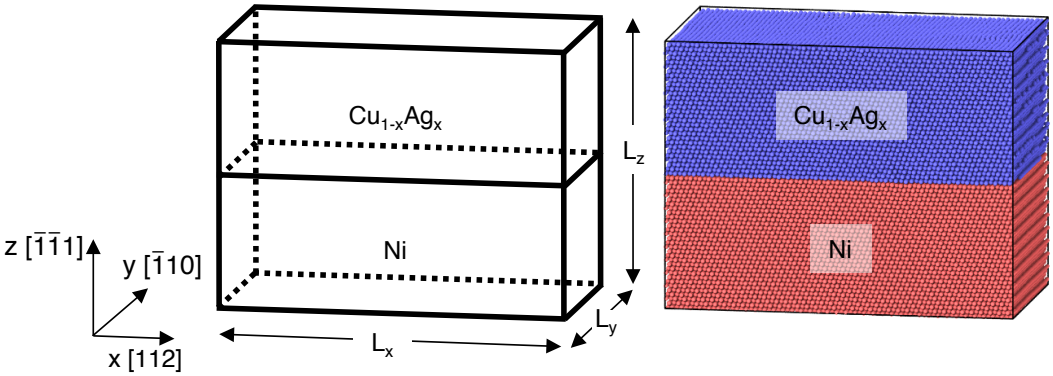

Figure 3.1: (a) Illustration of $Cu_{1-x}Ag_x$|Ni multilayer simulation geometry; (b) snapshot of the final atomic realization of the $Cu_{1-x}Ag_x$|Ni multilayer system with $L_z = 12\,\text{nm}$.

The initial $Cu_{1-x}Ag_x$ phases are prepared as solid solutions. For this a Cu FCC crystal is generated. Then a random fraction x of atoms is selected from this crystal. This fraction of atoms is mutated to Ag, arriving at a random solid solution with stoichiometry $Cu_{1-x}Ag_x$ and FCC structure.

3.2.3. Monte Carlo / molecular dynamics (MC/MD) relaxation

A combined Monte Carlo (MC) / molecular dynamics (MD) method (Neyts and Bogaerts, 2013) is used to relax the initial systems. The combined MC/MD method consists of repeating sequences of: N_{atoms} MC steps followed by a 20 ps MD run at isobaric-isothermal (NPT) conditions. Here N_{atoms} is the total number of atoms in the simulation. At the end of each sequence the last MD configuration is used as starting configuration for the next MC/MD sequence. The MC steps use the Atom-swap Monte Carlo method described in section 2.3.2. The MD run uses a Nosé-Hoover thermostat and an Andersen barostat (Shinoda et al., 2004) and relaxes stresses due to the swapped atoms. Relaxation time constants for the

Table 3.2: Minimum simulation cell size used for the simulations. The numbers m and n denote the number of unit cells of the $Cu_{1-x}Ag_x$ and Ni layer, respectively. A ratio $m/n \neq 1$ is necessary to accommodate the nominal mismatch δ of the two phases. The remaining residual mismatch is denoted by $\Delta\varepsilon$. The exact system size along the $[112]$ and $[\bar{1}10]$ directions is given after relaxation at 300 K.

	Cu|Ni	$Cu_{0.95}Ag_{0.05}$|Ni	$Cu_{0.90}Ag_{0.10}$|Ni
Ratio m/n	29/30	23/24	19/20
System size $L_x \times L_y$ (Å)	129.79×74.93	103.90×59.97	86.53×49.98
Nominal mismatch δ (%)	3.34	4.16	4.97
Residual mismatch $\Delta\varepsilon$ (%)	-0.047	-0.094	-0.11
Number of atoms	106260	67452	46460

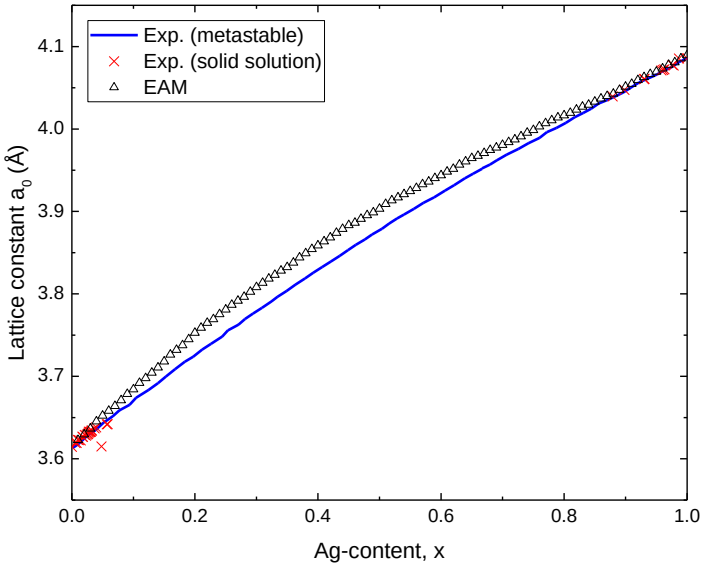

Figure 3.2: Calculated lattice constant a_0 of the $Cu_{1-x}Ag_x$ metastable solid solution computed at 0 K (black triangles). Experimental values are shown for stable (Subramanian and Perepezko (1993), red crosses) and metastable (Madelung (1991), blue line) solid solution. Values have been obtained at room temperature are given for reference.

thermostat and the barostat are 1ps and 5ps, respectively. The barostat controls the length of the three Cartesian cell vectors independently but does not allow the cell to tilt. This sequence of repeating MC/MD steps is a heuristic approach to relax the systems towards their thermodynamic equilibrium, a state that is inaccessible by direct molecular dynamics calculations because of long interdiffusion time scales.

3.3 Results

3.3.1. Structure of pure and solid solution multilayers

Due to the mismatch in lattice constant between the $Cu_{1-x}Ag_x$ and Ni phases, the system forms a regular triangular pattern of misfit dislocations at the interface. This leads to alternating zones of hexagonal close packed (HCP, stacking faults) and FCC stacking within the perfect FCC lattice. The stacking faults are color-coded in Fig. 3.3(a). HCP and coherent FCC regions are separated by a network of $\frac{1}{6}a_0\langle 112\rangle$ Shockley partial dislocations merging into spiral shaped nodes that are shown by the green lines in Fig. 3.3(b). The distance between two nodes is equal to 7.5 nm at 300 K for the perfect Cu|Ni interface. Larger cells with smaller residual mismatch (ratios $n/m = 59/61$ and $88/91$) give corrections to the node spacing $\lesssim 0.05\%$. This distance depends solely on lattice mismatch and is in agreement with values reported in Ref. (Shao et al., 2013).

After relaxation, atomic stresses $\sigma_i = w_i/V_i$ are computed from the atom-resolved virial w_i and atomic volumes V_i obtained from a Voronoi analysis. The atom-resolved virial w_i is defined as

$$w_i = m_i v_i v_i + \sum_{j=1, j\neq i}^{N} \vec{F}_{ij}\vec{r}_{ij} \tag{3.2}$$

where $\vec{F}_{ij}$ is the force on atom i due to the pair interaction with atom j. To resolve the virial per atom, pair-contributions (Thompson et al., 2009) to the virial are equally split between the two atoms participating in a pair. The stress per atom on the Cu side of the interface (Fig. 3.3(b, d, f)) reveals that the partial dislocation pattern affects the local stress, creating regions of tensile stress at the nodes of the misfit dislocation network and compressive stress within the HCP and FCC stacked regions.

Figure 3.3(c) and (d) shows that the perfect network of dislocations is perturbed by alloying Ag to the Cu layer in a random solid solution. Node spacing is reduced to an average of 4.6 ± 0.3 nm as the lattice mismatch increases from 3.5% to 5% by increasing Ag content from 0% to 10%. Figure 3.3(d) shows individual atoms that feel a highly compressive local hydrostatic stress (blue dots in Fig. 3.3(d)), which are all Ag atoms. Figure 3.3(c) also shows that with addition of Ag the node regions become more spread out.

3.3.2. Monte Carlo/Molecular Dynamics relaxation

The experimental Cu|Ni binary phase diagram (Massalski et al., 1990, Dey, 1968) has a miscibility gap at 600 K, with $Cu_{0.6\pm0.15}Ni_{0.4\pm0.15}$ and $Cu_{0.10\pm0.15}Ni_{0.90\pm0.15}$ at the bound-

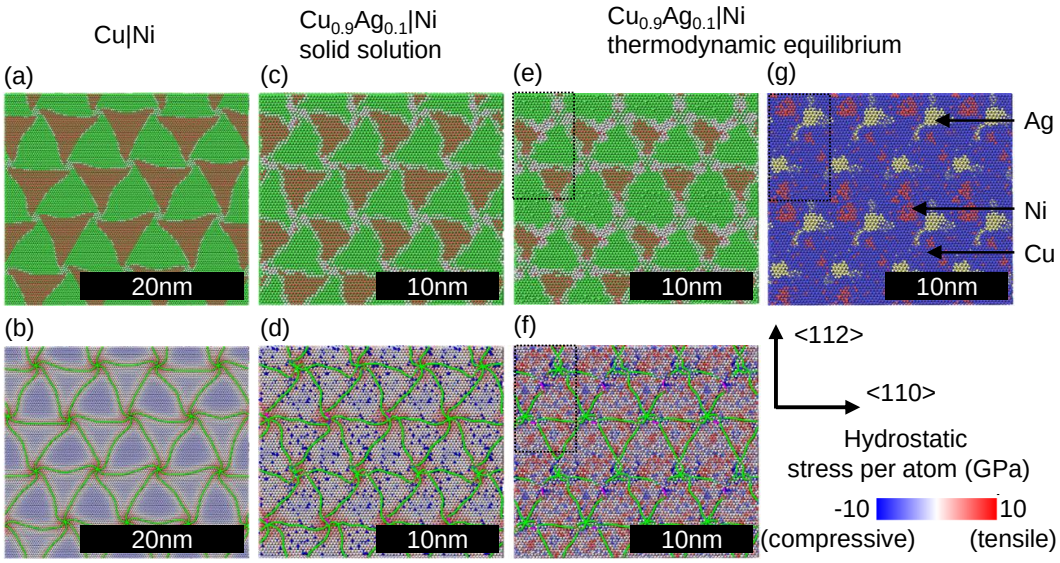

Figure 3.3: Interface structure on the Cu-rich side after annealing at 300 K and minimization of (a, b) Cu|Ni and (c, d) $Cu_{0.90}Ag_{0.10}$|Ni random solid solution. Panels (e-g) show $Cu_{0.90}Ag_{0.10}$|Ni after MC/MD relaxation and minimization. The atoms in panels (a, c, e) are colored after their local atomic environment as determined by common neighbor analysis (Honeycutt and Andersen, 1987, Stukowski, 2012). Atoms in green are FCC, atoms in red are HCP and atoms in white have other local environments. Panels (b, d, f) are color-coded according to the hydrostatic stress on the Cu side of the interface. The dark blue colored atoms (high compressive stress) in panel (d) are all Ag. The green lines in panels (b, d, f) are interfacial dislocations obtained with the dislocation extraction algorithm (Stukowski et al., 2012): Perfect dislocations are in blue, Shockley partials in green and stair-rod in purple. Panel (g) is color-coded according to the atom type at the interface. The black rectangles show the supercell used for the MC/MD calculations.

aries of this gap. After approximately 650 MC/MD sequences (at 600 K), the pure Cu|Ni periodic bilayer system equilibrates to a $Cu_{0.7}Ni_{0.3}$ layer and a $Cu_{0.3}Ni_{0.7}$ layer. The detailed composition is shown in Fig. 3.4(a) and is inside of the experimental miscibility gap. This occurs because the atom-swap Monte Carlo technique does not model the grand-canonical ensemble but rather constrains the overall composition of the system. In addition, the misfit between the layers introduced in the system cannot be removed by the the atom-swap Monte Carlo technique. The Cu|Ni interface, that was initially atomically sharp, has become smeared out over a distance of approximately 5 Å after MC/MD relaxation.

Ag atoms in layers of initial composition $Cu_{0.95}Ag_{0.05}$ and $Cu_{0.90}Ag_{0.10}$ remain in the Cu layer but segregate into clusters as shown in Figs. 3.3(g) and 3.4(b) at both 300 K and 600 K. The local environment of the Ag atoms is classified by the adaptive common neighbor analysis (Honeycutt and Andersen, 1987, Stukowski, 2012). This analysis shows that Ag is mainly (75%) within an FCC environment. The remaining 25% are mostly classified as either HCP or BCC. Visual inspection of the environment of Ag atoms shows that Ag appears to segregate into small clusters of bulk Ag. Additional MC/MD calculations have

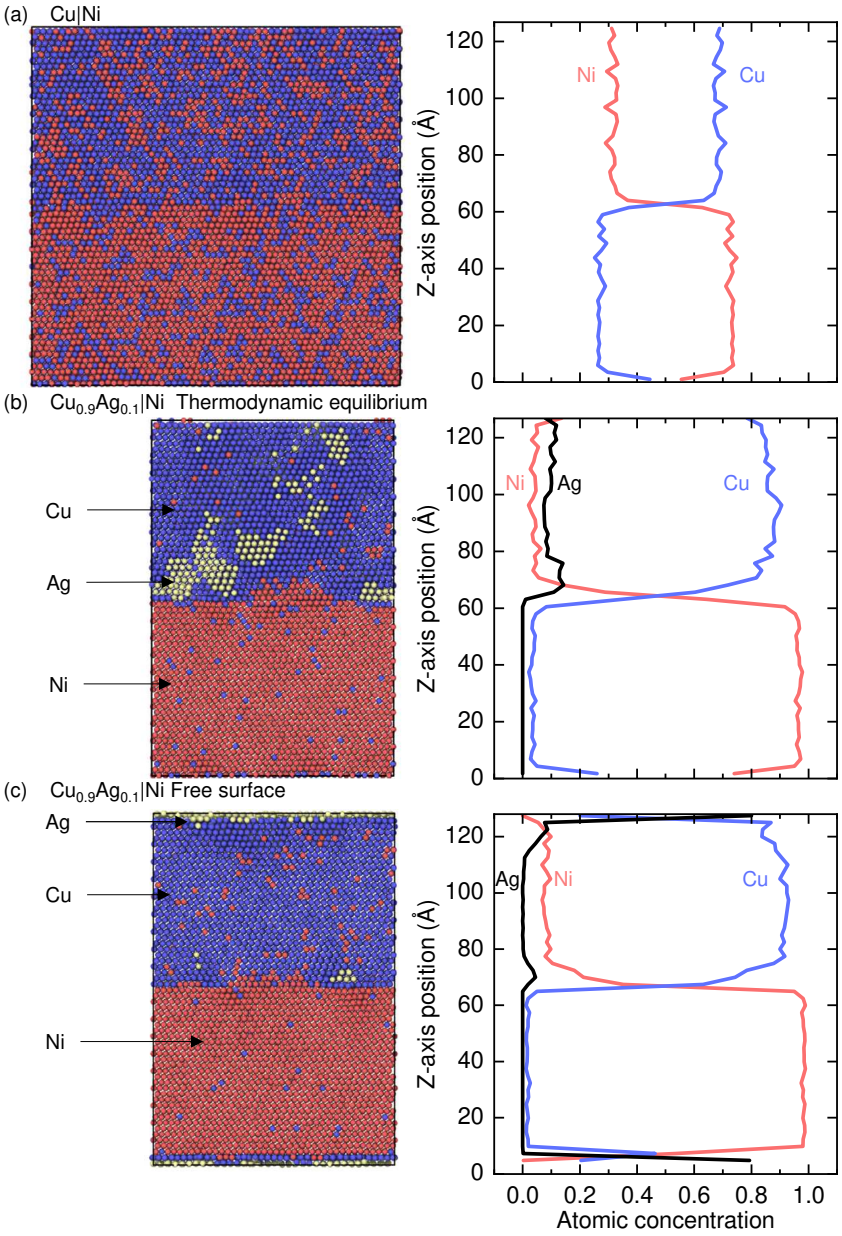

Figure 3.4: Atomic concentration profile along the [111] direction after MC/MD relaxation of a (a) Cu|Ni bilayer system at 600 K, (b) $Cu_{0.90}Ag_{0.10}$|Ni periodic bilayer system at 300 K and (c) $Cu_{0.90}Ag_{0.10}$|Ni bilayer system with a free {111} surface at 300 K. The snapshots on the left show the final stage of the MC/MD relaxations. Atoms are colored after their type.

been performed outside of the miscibility gap at composition $Cu_{0.99}Ag_{0.01}$ and temperature of 600 K. For bulk $Cu_{0.99}Ag_{0.01}$, Ag does not segregate and stays in solid solution. For the $Cu_{0.99}Ag_{0.01}$|Ni multilayer, it does segregate to the node positions even though the system is thermodynamically outside the miscibility gap. This suggests that node positions are favorable for Ag segregation for generic reasons.

As shown in Fig. 3.4(b), the Ag concentration is roughly constant when measured in thin slices parallel to the interface within the Cu layer. It increases in the region 1 nm around the interface, indicating segregation of Ag at the Cu|Ni interface. Within the interfacial plane, Ag preferentially segregates at node positions and along dislocation lines as shown in Fig. 3.3(g).

Segregation in a system with a free surface have also been probed. A free surface will be present during growth of a such multilayer system, e.g. by sputtering (Mirkarimi et al., 1992, Clemens et al., 1999). In the case of a (111) Cu surface, Ag segregates at the free surface as shown in Fig. 3.4(c), leading to a nonuniform Ag concentration profile across the layer. Enrichment of Ag at the heterointerface of as-grown multilayers could therefore occur during the growth process.

The effect of the MC/MD relaxation on the interface stacking and the misfit dislocation network in the ternary system are shown in Figs. 3.3(e) and (f), respectively. Cu-Ni intermixing occurs during MC/MD relaxation in the binary system and does not affect the dislocation network. Ag segregation, however, does affect the shape of the nodes. Their spiral character is lost, their length increases and sessile stair-rod dislocations form at the interface. The planar dislocation network becomes a three-dimensional network with expanded nodes and dislocation loops extending into the Cu rich layer.

3.3.3. Validation of the average EAM potential

To validate the average EAM (AEAM) potential constructed using the method described in section 2.1.2, The properties of interest are computed using both the AEAM potential and the regular EAM potential. While the AEAM potential gives only one results per concentration by definition, the EAM require averaging over several solid solution configurations for a given concentration for a representative result. Four different random solid solutions are used for each concentration.

Figure 3.5 shows the results obtained over the entire concentration range. The AEAM potential shows a good agreement for cohesive energies and lattice constants obtained at 0 K with a deviation smaller than 1% from the EAM potential values. The (111) surface energies obtained with the AEAM potential are in good agreement with the one obtained with the EAM potential, with a maximum deviation of 5% for a concentration of 45 at.% Ag. The (100) surface energies show a larger discrepancy of up to 10%. The intrinsic stacking fault energies predicted by the AEAM potential agree with the EAM potential value at low and high Ag concentration but are underestimated at a concentration of around 20 at.% Ag. The complex shape of the intrinsic stacking fault energies across the concentration range is nonetheless recovered with an inflexion point at around 40 at.% Ag. The AEAM reproduces

correctly the bulk modulus over the entire concentration range, while the shear moduli are only correctly predicted in the 0-20 at.% Ag and 80-100 at.% Ag ranges. In the 20-80 at.% Ag range the moduli predicted by the AEAM are overestimated by up to 15% with respect to the solid solution results. The results indicate that the AEAM potential is well suited for an usage here, where the concentration of Ag does not exceed 10 at.%.

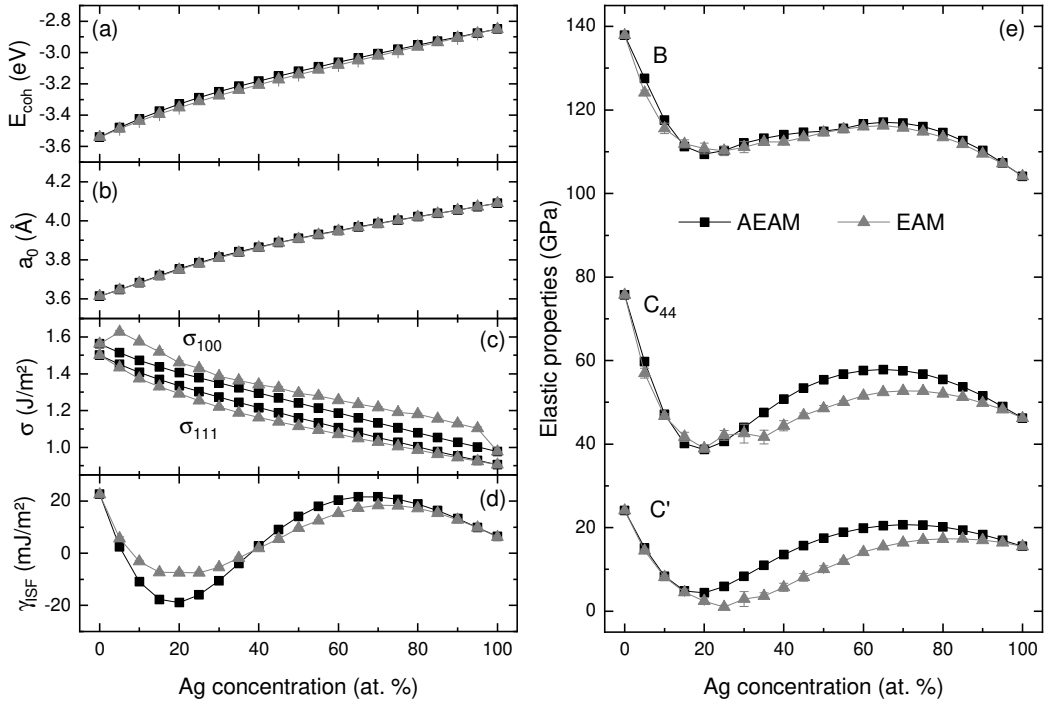

Figure 3.5: Comparison of the properties obtained at 0K for the $Cu_{1-x}Ag_x$ system using an EAM potential and AEAM. The properties computed are (a) cohesive energy, (b) lattice constant, (c) surface energies, (d) intrinsic stacking fault energies and (e) Bulk modulus B, shear moduli C_{44}, $C' = \frac{C_{11}-C_{12}}{2}$. The results obtained for the EAM solid solution are averaged over 4 random solid solutions iteration, the error bars show the standard deviation of the obtained results.

3.3.4. Energetics of Ag segregation

To rationalize the segregation of Ag to the node positions, one can compute the difference in energy of a bulk Ag atom within a solid solution of $Cu_{0.90}Ag_{0.10}$ to an Ag sitting at the interface of $Cu_{0.90}Ag_{0.10}$ and Ni. Sampling over different configurational realizations of the solid solution occurs implicitly by using a compositionally-averaged EAM formulation for $Cu_{0.90}Ag_{0.10}$, as described in section 2.1.2. This model introduces an alloy-average atom type $\langle Cu_{0.90}Ag_{0.10}\rangle$ from which a crystalline solid is built. The energetics of Ag segregation is then computed by placing individual Ag atoms in this alloy-averaged solid.

The energy difference maps obtained for moving an Ag atom from the bulk to the interface are shown in Fig. 3.6. These maps show the gain in energy when moving Ag to the first and the second interfacial layers separately. In these calculations, the first interfacial layer can have up to two Ag atoms already present at the interface. The energy landscape on the first layer has a sixfold symmetry. Ag atoms segregate preferentially at node positions or along the dislocation lines. On the second interfacial layer the energy landscapes has threefold symmetry and low energy positions at HCP stacked positions. The energy gained by moving one to three Ag atoms to the interface ranges from 0.3 to 0.4 eV. These calculations with individual Ag atoms also provide information about the hydrostatic atomic stress in the node area. The larger Ag atom reduces the tensile stress by approximately 7 GPa (from 8.8 GPa to 1.7 GPa) on the central position when a $\langle Cu_{0.95}Ag_{0.05}\rangle$ atom is substituted by Ag. Substituting a second Ag atom next to the aforementioned one reduced the hydrostatic stress by an additional $\approx$ 1GPa (from 6.7 GPa to 5.5 GPa) at the substitution positions next to the central position.

3.4 Discussion

The first notable observation is that no Ag is found in the Ni layer because its heat of formation in Cu is significantly lower than in Ni. This difference is in accord with the binary Cu-Ag and Ag-Ni phase diagrams (Massalski et al., 1990) that show miscibility of up to 3% Ag in Cu at 1000K and no miscibility of Ag in Ni. Any Ag in the multilayer system therefore stays out of the Ni and alloys with Cu and any excess Ag segregates within the Cu layer. The first aim to modify only one of the layers with the addition of Ag to the Cu|Ni multilayer system was hence successful. However, the MC/MD calculations show that this segregation leads to the formation of clusters of pure Ag in the Cu layer and partially at the interface.

The segregation of individual Ag atoms as well as the formation of the Ag clusters occurs at the nodes of the interfacial Cu|Ni misfit dislocation network. A simple heuristic argument explaining segregation into these nodes can be developed from the atomic size difference of Ag and Cu. Since Ag is larger than Cu, it feels a compressive stress within the solid solution phase. From the hydrostatic component of local atomic stress tensor (Fig. 3.3(b)) it is known, that the nodes of the misfit dislocation network are under tension on the Cu side. This tensile stress, as mentioned in section 3.3.4, is partially released by moving the larger Ag atoms there (Meunier et al., 2000, Borovikov et al., 2017), consistent with the observation that local stress alters the solubility of a solute (Larché and Cahn, 1985). In the case of Cu and Ag this has, for example, been observed in a $Cu_{1-x}Ag_x$ nanocrystaline structures (with

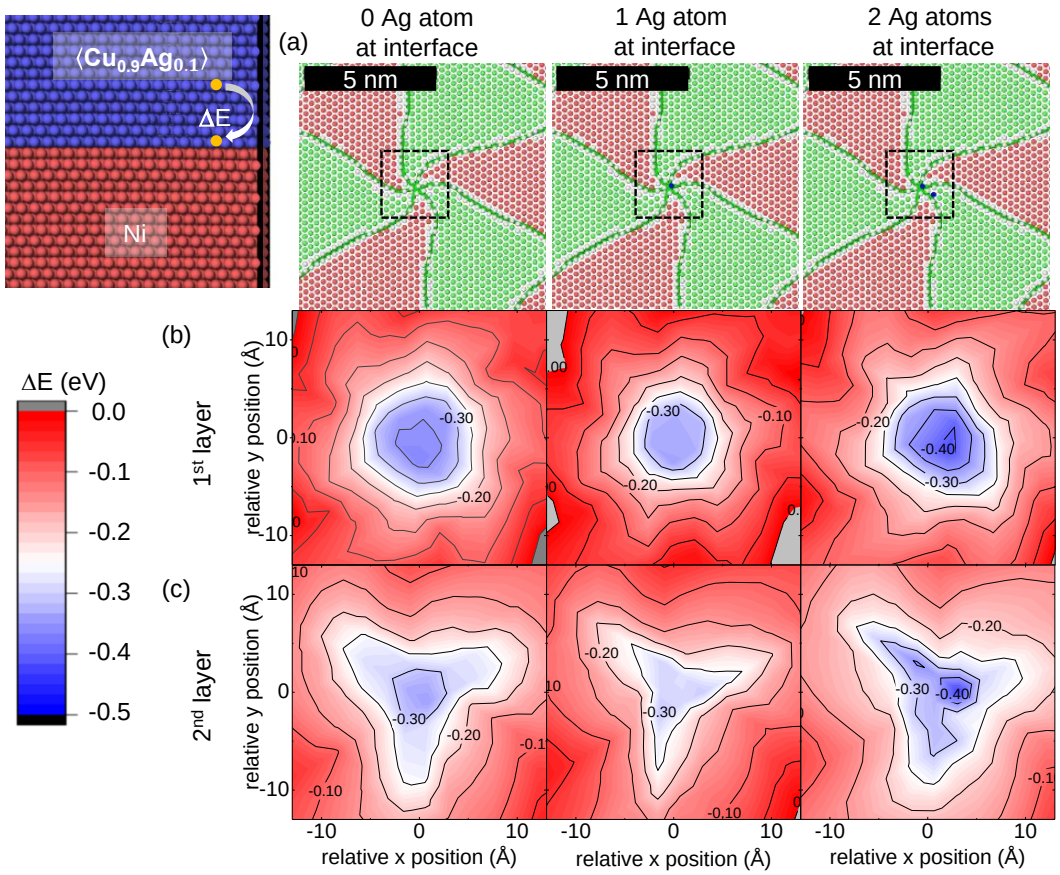

Figure 3.6: Energy map obtained for the energy difference of an Ag solute at bulk and interfacial positions. Panel (a) shows a common neighbor analysis of the corresponding interface (atoms in green are FCC, atoms in red HCP and atoms in white have other local environments). Energy maps (b) and (c) show the energy difference when moving a solute atom (b) directly to the interface and (c) to the second layer from the interface. Dashed rectangles in (a) show the area that is mapped in (b) and (c). The columns show the energy obtained within in the pristine average-atom solid, and with one or two Ag atoms already present at the interface. Blue atoms in panel (a) show the position of these Ag atoms. Relative positions in panels (b) and (c) are calculated with respect to the center of the node.

$x = 0 - 24\%$), where Ag segregates to the grain boundaries because it reduces the tensile stress arising from large free volumes (Riedl et al., 2013, Li and Szlufarska, 2017).

This heuristic argument is supported by the potential energy calculations with a compositionally (alloy-)averaged interatomic potential (Fig. 3.6). These calculations show a decrease in potential energy as the Ag atom segregates at the nodes of the interface. Furthermore, the energy difference becomes more favorable when an Ag atom is already present at these node positions. This suggests stabilization of Ag clusters for the investigated Ag concentrations of 5% to 10%.

The calculations have additionally shown that the stabilization of bulk Ag at the nodes leads to segregation even at compositions outside the miscibility gap. Practically this means that an alloyed layer can not be easily stabilized as an alloy but will tend to segregate out. The interface is always providing locations of high stress which can be reduced by moving a size-mismatched element there. This mechanism should also be active at other types of interfaces than the one investigated here. In other words, the presence of the heterophase interfaces will always tend to widen a miscibility gap, even for the almost ideal $\{111\}$ interfaces.

Experimental growth of such multilayer stacks temporarily exposes free surfaces of Cu and Ni to the growth chamber. Calculations have shown that Ag segregates to a free Cu surface. This could mean that during growth Ag enriches preferentially at the Cu—Ni interfaces, leading to an asymmetric Ag concentration. Such concentration gradient could be easily detected in microscopy on film cross-sections.

3.5 Summary

In this chapter, Ag has been alloyed into the Cu layer of a Cu|Ni (111) multilayer system. This alloying affects the interface dislocation network by increasing the misfit between the layers. The interface dislocation network is a triangular pattern of alternating FCC and HCP (stacking fault) regions, which becomes denser with increasing Ag content because the lattice mismatch between the $Cu_{1-x}Ag_x$ and Ni phases increases. Monte Carlo simulations reveal that Ag atoms segregate within the Cu layer at the nodes of the triangular misfit dislocation network.

4. Polycrystalline layers: Structure

4.1 Introduction

The previous chapter showed that Ag in the $Cu_{1-x}Ag_x|Ni$ multilayers systems has the tendency to segregate. The segregation took place in area of the systems with low coordination or high tensile stress. The systems studied in chapter 3 were idealized structures with each layer comprised of a single crystal. Experimentally such multilayer systems would most likely have polycrystalline layers. For example in the fabrication process using physical vapor deposition, structure tend to have columnar grains (Was and Foecke, 1996) with a grain size scaling linearly with the layer thickness (Srolovitz et al., 1995). In this chapter the impact of the introduction of grain boundaries in the $Cu_{0.90}Ag_{0.10}|Ni$ multilayer system is investigated. This investigation is done with the help of a bilayer system having 40 nm thick layers. This allow to work with grain sizes readily observable experimentally (Li and Zhang, 2010). Such system size is also used in atom probe experiments in order to obtain information at the atomic scale on precipitations, compositions and interface shapes (Gault et al., 2012). This chapter focuses on the results obtained for a relaxed $Cu_{0.90}Ag_{0.10}|Ni$ polycrystalline structure. This increase of system size, from about 1000 nm^3 in the previous chapter to 180,000 nm^3, requires a modification of the approach to the MC/MD relaxation process, which does not parallelize well. For this matter the variance constraint semi-grand canonical (VC-SGC) Monte Carlo / Molecular dynamics method (MC/MD) is used, which allows for highly parallelized calculations.

4.2 Methods

The polycrystal was setup using a 2D Voronoi tessellation procedure (Voronoi, 1908, Hirel, 2015). This procedure forms polycrystalline layers with columnar grains aligned along a specific direction, here [111], as found experimentally in FCC multilayers build by physical vapor deposition (Li and Zhang, 2010). In order to build the polycrystalline layer, four seeds are used on a plane specifically arranged to form regular hexagonal shape after construction.

From these four seeds the Voronoi tessellation forms convex polyhedrons with planes lying halfway between neighboring seeds. The final system shown in Fig. 4.1(a-b) is composed of approximately 15×10^6 atoms spread over two 40 nm thick layers. Each layer has 4 regular hexagonal grains of approximately 30 nm diameter.

As described in section 2.3.3, the variance constraint semi-grand canonical Monte Carlo/Molecular dynamics method (MC/MD) have been used to bring a polycrystalline multilayer system to its thermodynamic equilibrium. The system was initially setup with a $Cu_{0.90}Ag_{0.10}$ solid solution layer and a pure Ni layer. For this a Cu FCC polycrystal was generated from which is then selected a random fraction of atoms. This fraction of atoms was then mutated to Ag, arriving at a random solid solution with stoichiometry $Cu_{0.90}Ag_{0.10}$ and a FCC polycrystalline structure. The calculation was performed at 300 K using $\Delta\mu_0^{\mathrm{NiCu}} = -0.89$ eV and $\Delta\mu_0^{\mathrm{NiAg}} = -1.46$ eV. The target global concentrations were fixed to $c_{\mathrm{Cu}} \approx 43$ at.% and $c_{\mathrm{Ag}} \approx 5$ at.%. Similarly to the serial MC/MD method used in chapter 3, the calculation consisted in repeating sequences of N_{atoms} MC trial moves followed by 20 MD steps at isobaric-isothermal (NPT) conditions with an integration time step of 2.5 fs. Here N_{atoms} is the total number of atoms in the simulation, i.e. approximately 15×10^6. A total of approximately 75,000 MC/MD steps was performed. The total number of MC/MD steps was chosen large enough to reach a steady state of the local concentrations of the different atom types in the system.

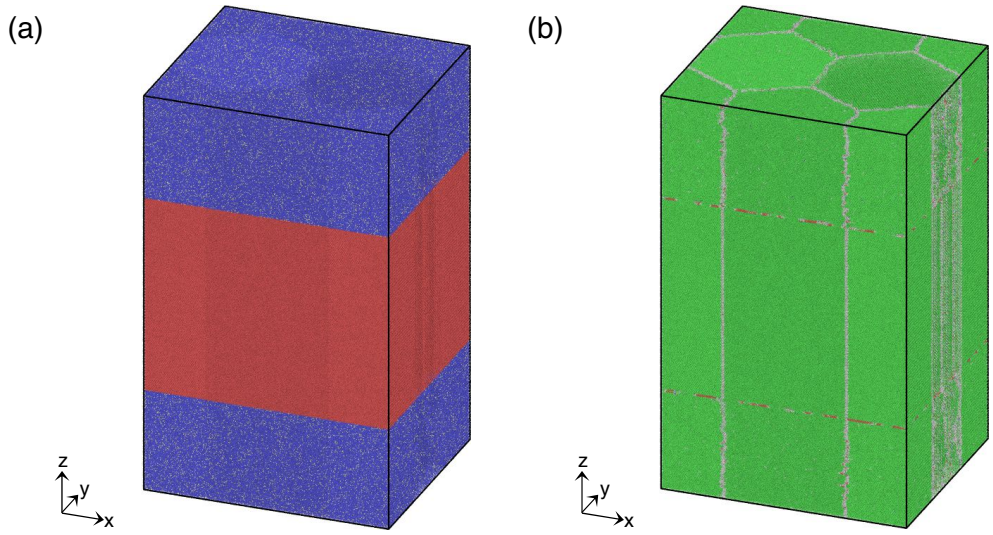

Figure 4.1: $Cu_{0.90}Ag_{0.10}$|Ni initial polycrystalline bilayer system with Ag in solid solution in the Cu layer. Panel (a) shows the atoms colored according to their type with Ni in red, Cu in blue and Ag in yellow. The atoms in panel (b) are colored after their local atomic environment as determined by common neighbor analysis (Honeycutt and Andersen, 1987, Stukowski, 2012) highlighting the grain boundaries. Atoms in green are FCC, atoms in red are HCP and atoms in white have other local environments.

The resulting relaxed structural model was used to identify segregation patterns occurring in polycrystalline FCC/FCC alloyed multilayer system presenting miscibility gaps.

4.3 Results

Figure 4.2(a-c) shows the system state obtained after 75000 MC/MD steps. Figure 4.3(a) shows the corresponding profile concentration along the main [111] z-axis. It shows a Cu-rich layer having an average composition of $Cu_{0.85}Ag_{0.10}Ni_{0.05}$ and a Ni-rich layer having global a composition of $Cu_{0.05}Ni_{0.95}$. The inset of Fig. 4.3(a) shows that the initially sharp interface is smeared over a distance of approximately 1 nm.

Figures 4.2(b-c) and 4.3(b-c) show respectively qualitative and quantitative results on the composition of the grains and grain boundaries. In the Cu-rich layer the grains have an average composition of $Cu_{0.87}Ag_{0.08}Ni_{0.05}$ with a high concentration of Ag at the grain boundaries up to 27 at.% (Fig. 4.3(b)). The average composition of the grains in the Ni-rich layer is $Cu_{0.02}Ni_{0.98}$ with a clear trend to Cu segregating at the grain boundaries with concentration going up to 22 at.% (Fig. 4.3(c)). Figure 4.2(d) shows that the majority of the Ag atoms are in the Cu-rich layer while a few Ag atoms are visible along the grain boundaries in the Ni-rich layer.

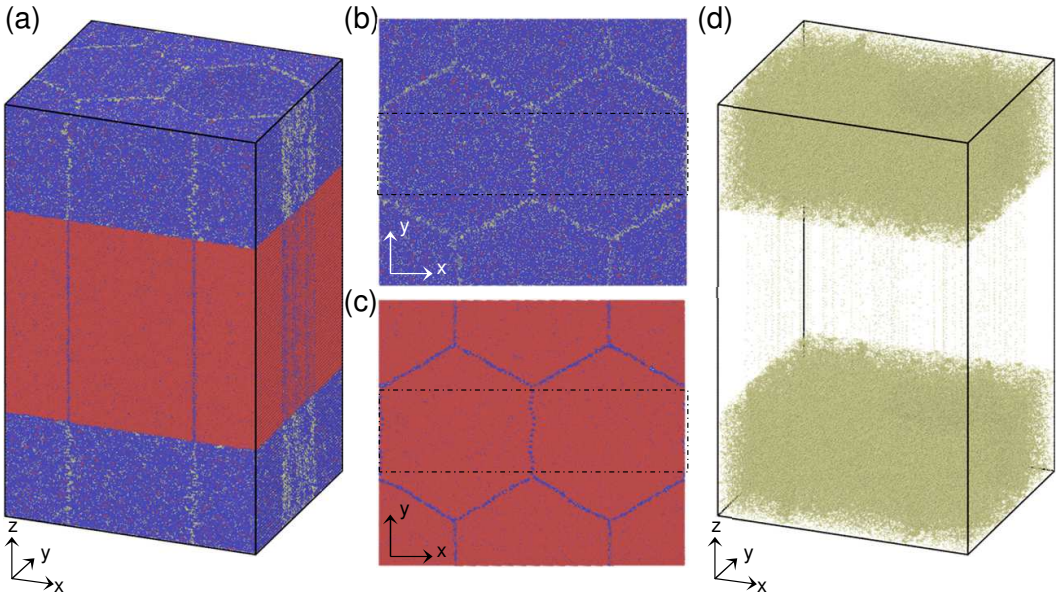

Figure 4.2: (a) $Cu_{0.9}Ag_{0.1}|$Ni polycrystalline bilayer system after VC-SGC MC/MD relaxation, (b) cross section of the Cu-rich layer, (c) cross section of the Ni-rich layer, (d) Ag atoms in the polycrystalline bilayer system after VC-SGC MC/MD relaxation. Atoms colored according to their type with Ni in red, Cu in blue and Ag in yellow. The dashed rectangles in (b-c) represent the slice used to extract the profile concentration in Fig. 4.3.

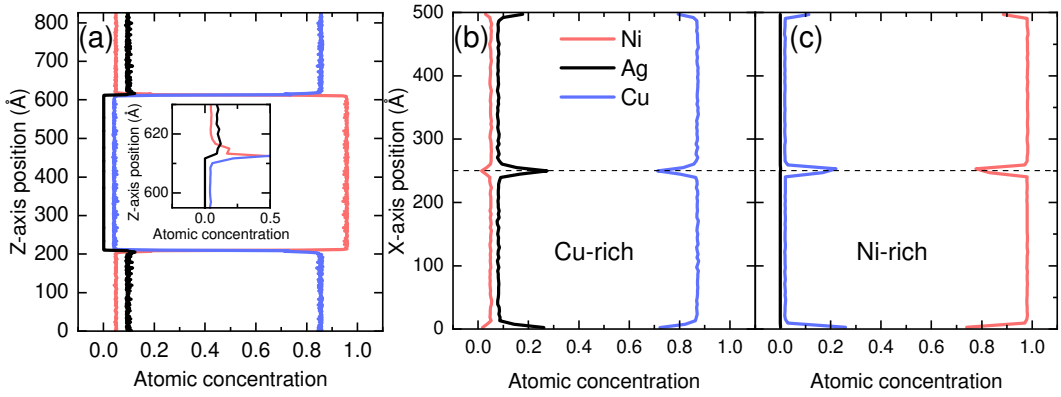

Figure 4.3: (a) Atomic concentration profile along the [111] direction after VC-SGC MC/MD relaxation. The inset shows a zoom on one of the interface concentration profile. (b) Concentration profile in the Cu-rich layer along the x-axis in a 15nm centered slice shown in fig. 4.2(b). (c) Concentration profile in the Ni-rich layer along the x-axis in a 15nm centered slice shown in fig. 4.2(c). The dashed lines in (b) and (c) show the grain boundary position.

Figures 4.4(a-c) show quantitative information about the Ag segregation in the form of concentration iso-surfaces. This confirm that the highest Ag concentration, volume with more than 25 at.% Ag, is at the grain boundaries in the Cu-rich layer. While the concentration at the interfaces is only on the order of 10-15 at.% as the small iso-surfaces patched disapear on 4.4(c).

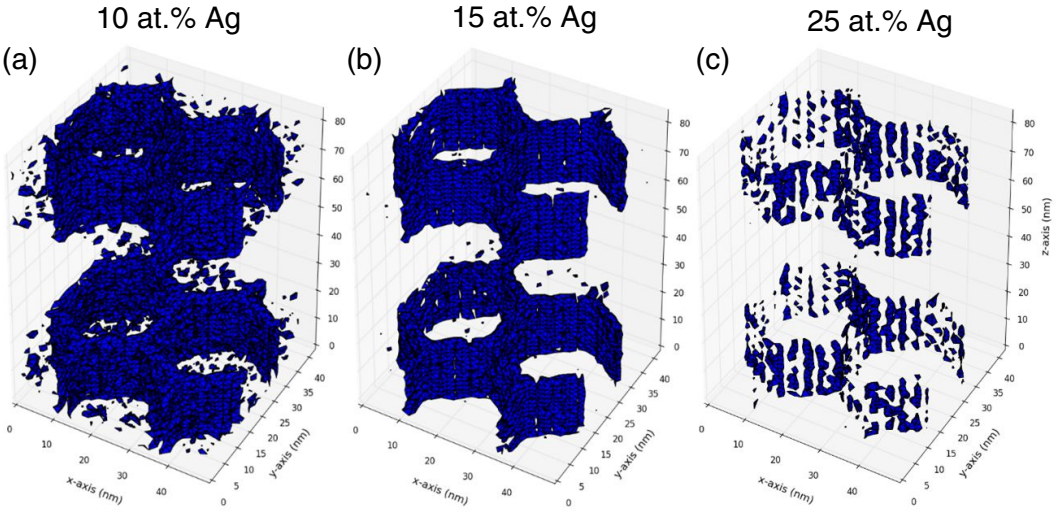

Figure 4.4: Concentration iso-surfaces for (a) 10at.% Ag, (b) 15at.% Ag and (c) 25%. Ag using $1.5 \times 1.5 \times 1.5\text{nm}^3$ voxels. Neighboring voxel sharing the same concentration are connected using a marching cube algorithm. The surface mesh connecting these voxels is shown in blue.

4.4 Discussion

The grains composition extracted from the VC-SGC MC/MD relaxation are still within the miscibility gaps of the Cu-Ni and Cu-Ag systems shown in Fig. 1.2 and 1.4(a). This confirms that the constraint applied in the VC-SGC MC/MD method allows to model systems at concentration being inside a miscibility gap. Similarly to the monocrystal setup discussed in chapter 3 the Ag shows a strong tendency to segregate, and the Cu and Ni show a slight intermixing across the interface.

The calculations performed here with a polycrystalline structure show that the presence of grain boundaries amplify the segregation of Ag following the scheme demonstrated in section 3.4. Ag segregates out of the Cu-rich layer towards areas where the stresses due to a large lattice mismatch can be released. Riedl et al. (2013) noticed this behavior in atom probe tomography experiment of nanocrystalline $Cu_{1-x}Ag_x$ alloys for $x = 0.2 - 0.4$at.%, and Li and Szlufarska (2017) observed a similar segregation pattern in a polycrystalline $Cu_{1-x}Ag_x$ alloy model with $x = 0 - 24$at.% using a different potential. The large amount of Ag segregating in the grain boundaries prevent it from having a higher Ag concentration at the interfaces than in the volume.

Even though Ag and Ni are not miscible at 300K (Fig. 1.4(b)) some Ag is observed at the grain boundaries in the Ni-rich layer after MC/MD equilibration. The presence of Cu in this same grain boundaries and the larger volume available could explain the presence of Ag at this grain boundaries. Atom probe tomography experiments on $Cu_{1-x}Ag_x|Ni$ polycrystalline multilayers carried out by collaborators (Schwaiger group at KIT) also showed Ag segregation together with Cu at grain boundaries in Ni-rich layers (Schwaiger, 2015).

4.5 Summary

Compared to the single crystal structure described in the previous chapter, the polycrystalline structure adds another location for segregation with the grain boundaries. The driving force to segregation of both Ag and Cu remain similar to the one discussed in chapter 3, i.e. large free volume releasing the stress due to the lattice mismatch.

A $Cu_{0.90}Ag_{0.10}|Ni$ polycrystalline structure has been modeled at a size directly comparable with atom probe tomography experiments (Schwaiger, 2015). This model could complement atom probe tomography experiments as it brings information at the atomic scale when the

atom probe tomography has a detection efficiency of about 50% (Gault et al., 2012). This shows a possible synergy between experiments and MD models.

5. Monocrystalline layers: Deformation

5.1 Introduction

In this chapter the MC/MD relaxed systems obtained in chapter 3 is used to investigate the effect of Ag on the mechanical properties of the $Cu_{1-x}Ag_x$|Ni monocrystalline multilayer system. As described earlier Ag modifies the lattice mismatch between the two layers and segregates in the Cu-rich layer. Therefore it is interesting to examine the impact of Ag on the misfit dislocation mobility by running simple shear calculation along the interface planes. By increasing the lattice mismatch Ag increases the density of node dislocation at the interface. For this reason this chapter explores the effect of such increase on the multilayer strength by running biaxial tensile deformation in the interface planes. These calculations remove any initial motion of the misfit dislocation because the Schmid factor on the interface planes is zero. Lastly, one more loading condition is considered where the systems are sheared across the interface planes.

5.2 Methods

Direct deformation was performed at a temperature of 1 K and 300 K. 1 K runs were carried out to reduce thermal noise that complicates atomic-structure analysis. The same atomic structure obtained from the MC/MD relaxation at 300 K was used as starting configuration in both cases. A strain rate of $10^8\,s^{-1}$ was used in all cases; yield stress dependence on strain rate is negligible at these rates in FCC metals (Horstemeyer et al., 2001, Zepeda-Ruiz et al., 2017). Before straining, the systems were relaxed at the final temperature for 500 ps using the Nosé-Hoover/Andersen ensemble without any strain. Simple shear strain was applied along $[112](\bar{1}\bar{1}1)$ directions for shear parallel to the multilayer interfaces and along $[\bar{1}\bar{1}1](\bar{1}10)$ directions for perpendicular shear by homogeneously deforming the box. The

notation $[abc](hkl)$ for simple shear reports both the direction of shear $[abc]$ and the plane of shear (hkl).

Under perpendicular shear, the dislocations are expected to nucleate at the interfacial nodes (Shao et al., 2015). Due to the interface orientation $(\bar{1}\bar{1}1)$ the dislocation nucleate and glide on $\{111\}$ planes that are not parallel to the main cell axes. In the case of a small periodic simulation cell, dislocation reenter the cell through the periodic boundaries which results in the critical multiplication of the nucleated dislocations at a non-physical rate. In order to weaken this replication issue supercells were used. The supercells consisted in $2 \times 2 \times 1$ replication of the simulation cell given in Tab. 3.2 for shear perpendicular to the heterointeface and $1 \times 1 \times 1$ simulation cells for the parallel shear calculations, where shear is localized at the interface and no dislocations are emitted in to the bulk of Cu or Ni layers.

Additionally biaxial tensile tests were carried out on $2 \times 4 \times 2$ supercells of the simulation cells reported in Tab. 3.2 resulting in supercells with lateral size of approximately 20 nm. The biaxial tensile test was carried out on a box with full periodic boundary conditions along the [112],$[\bar{1}10]$ and $[\bar{1}\bar{1}1]$ directions. The deformation was imposed by changing the simulation box size along the [112] and $[\bar{1}10]$ directions according to the defined strain rate. The pressure perpendicular to the deformation (i.e. the $[\bar{1}\bar{1}1]$ direction) was kept at zero using a Berendsen barostat (Berendsen et al., 1984) with a relaxation time constant of 100 ps.

5.3 Results

5.3.1. Simple shear deformation

The mechanical response of the bilayer system is probed via carrying out simple shear deformation parallel to the heterointerface. Calculations are carried out on the fully MC/MD-relaxed systems, but on larger supercells as described in the methods section. For parallel simple shear , the stress strain curves in Fig. 5.1(a) show a clear increase of the yield stress from 0.3 GPa to about 1.3 GPa at strains of 2% and 4%, respectively, when alloying 5-10% Ag to the Cu layer. The values obtained for the fully MC/MD-relaxed system are higher than for the solid solution case where the heterointerface is atomically flat, and for which the calculations gave a maximum stress on the order of approximately 50 MPa. These critical stresses are in good agreement with the experimental interface shear strength value for Cu|Ni multilayers (Liu et al., 2017).

Table 5.1: Flow stress at 300 K for parallel simple shear, perpendicular simple shear and biaxial shear of $Cu_{1-x}Ag_x|Ni$ with $x = 0\%, 5\%, 10\%$. Simple shear values are averages of the stress from 20 to 40% strain, biaxial values are averaged from 4% to 14% strain. Error ($\pm$) is the standard deviation of stress values in that range. Results given in parenthesis are computed at 1 K. Results are given in GPa.

System	Parallel	Perpendicular	Biaxial
Cu|Ni	0.03±0.06	1.03±0.26	2.64±0.19
	(0.08±0.08)	(1.36±0.34)	(3.25±0.22)
$Cu_{0.95}Ag_{0.05}|Ni$	0.33±0.15	1.13±0.43	3.05±0.42
	(0.52±0.18)	(1.72±0.46)	(3.87±0.40)
$Cu_{0.90}Ag_{0.10}|Ni$	0.44±0.22	1.54±0.42	3.41±0.42
	(0.72±0.27)	(1.97±0.38)	(4.44±0.73)

The stress-strain curve appears almost periodic at low strains for the binary system. It becomes irregular and intermittent for the ternary system as Ag segregates at the nodes. During shear, the stress appears to evolve towards a state with smaller fluctuation amplitudes at large strain for all cases. The final flow stress is larger for the systems alloyed with Ag than the pure Cu|Ni multilayer (see Tab. 5.1). Atomic strain analysis (Falk and Langer, 1998, Shimizu et al., 2007) reveals that deformation is always localized at the interface for both pure Cu|Ni and the alloyed system.

Figure 5.1(e) shows the evolution of the dislocation density

$$\rho_{\text{dislocations}} = \frac{\text{Total dislocation line length}}{\text{Cell volume}} \tag{5.1}$$

as a function of strain. The total dislocation line length is here obtained with a dislocation extraction algorithm (Stukowski et al., 2012). The dislocation densities are constant for all strain values and for pure Cu|Ni as well as the alloyed systems. This is in agreement with the observation of shear localization at the interface. The dislocation density in the alloyed $Cu_{0.90}Ag_{0.10}|Ni$ system is twice as large as the density in the pure Cu|Ni system.

Figure 5.1(b,d) show the stress-strain curves obtained for simple shear perpendicular to the interface for different Ag concentrations after MC/MD relaxation. It is worth noting that at 300 K the stress is lower than at 1 K because thermal activation aids movement and nucleation of dislocations. At strains below 10%, the curves show the same periodic behavior seen for parallel shear. As the strain increases to about 20%, dislocations are emitted into the Cu layer and the stress-strain curve starts to show intermittent behavior. In contrast to parallel shear, where no shear strengthening was observed, in the perpendicular shear cases a slight strengthening is observed once dislocations are present in the bulk. Again, the average flow stress is slightly larger for the systems with Ag than the pure Cu|Ni multilayer (see

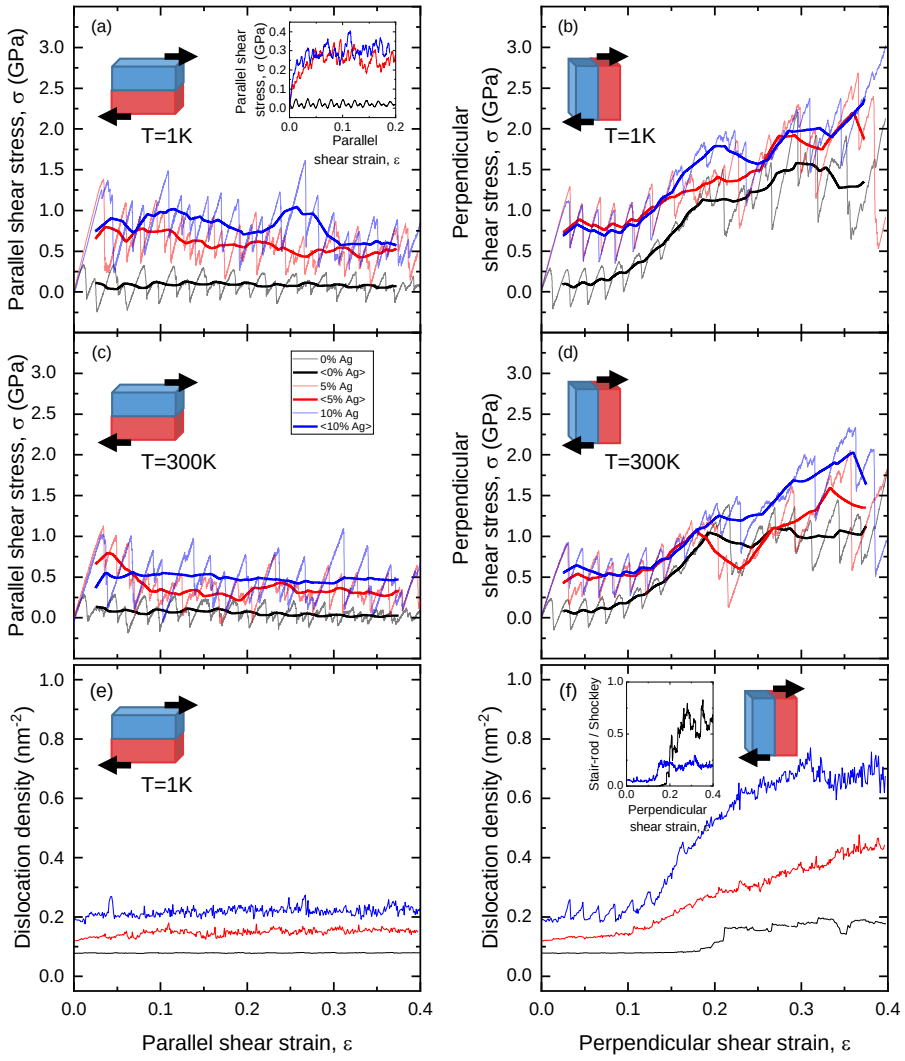

Figure 5.1: Stress-strain curves during simple shear at 1 K and 300 K (a,c) parallel, (b,d) perpendicular to the (111) interface for the Cu|Ni binary, the $Cu_{0.95}Ag_{0.05}$|Ni ternary and $Cu_{0.90}Ag_{0.10}$|Ni ternary system after MC/MD relaxation. Thick lines are a moving averages over a strain interval ± 0.025 around the respective data point, thin lines show the full data. Panels (e) and (f) show the dislocation density (at 1 K) for the three stoichiometries and parallel and perpendicular shear, respectively. The inset in panel (a) shows the stress strain curve for the atomically flat interface systems. The inset in panel (f) shows the ratio of the stair-rod dislocation density to the density of Shockley partials for the Cu|Ni binary and the $Cu_{0.90}Ag_{0.10}$|Ni ternary systems.

Tab. 5.1). Figure 5.1(f) shows the corresponding evolution of the dislocation density as a function of strain. The dislocation densities are increasing at smaller strain values (≈ 0.1) for the alloyed systems, while the density only increase at a strain value of approximately 0.2 for the pure Cu|Ni system. The dislocation density is 3 to 4 times higher in the ternary systems than in the binary system.

The ratio of the density of stair-rod dislocations to the density of Shockley partials is shown in the inset of Fig. 5.1(f) as a function of applied strain, and it is about a factor of three larger for the binary system than for the one with 10% Ag. The stair-rod dislocations are defined as dislocations having a $\frac{1}{6} < 110 >$ Burgers vector.

Figure 5.2 shows the evolution of the atomic fraction with $\gamma_i > 30\%$ in both the Cu-rich and Ni-rich layer as a function of strain. This quantifies the participation of the two layers in the deformation process. The evolution of this participation fraction in Fig. 5.2 shows no strain-accumulation within the layers below the yield strain (≈ 0.2). After yielding the participation steadily increases in the Cu-rich layer for all systems. The participation of the Ni-rich layer is much lower (about 4 times at $\varepsilon = 0.4$). Each step in the curves for the Ni-rich layer corresponds to a dislocation burst.

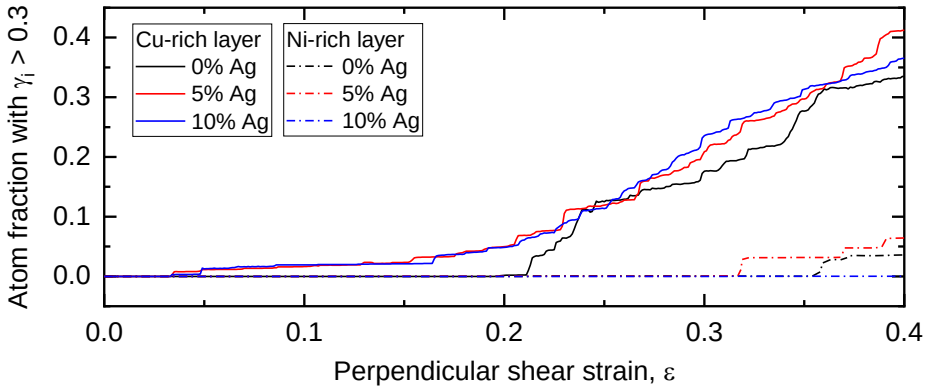

Figure 5.2: Atom fraction in the Cu-rich and Ni-rich layers (excluding atoms ± 1 Åaround the interfaces) with an atomic strain $\gamma_i > 0.3$ for $Cu_{1-x}Ag_x|Ni$ with $x = 0\%, 5\%, 10\%$ at 1 K under perpendicular shear.

5.3.2. Biaxial tensile deformation

Biaxial tensile deformation parallel to the interface roughly corresponds to the situation encountered in a compression test or directly underneath the tip of an indenter. Specifically, the system is elongated along the $[112]$ and $[\bar{1}10]$ directions while maintaining zero normal stress (i.e. along $[\bar{1}\bar{1}1]$). Stress strain curves are shown in Figs. 5.3(a) and (b) for 300 K and 1 K, respectively. Stress rises monotonously for the three systems up to strains of around 2.5% for all systems before dropping to around 2.5 GPa to 4 GPa after yield. Note that in contrast to simple shear, the ternary alloys show a slightly lower yield stress than the pure multilayer. Fig. 5.3(c) shows the dislocation density as a function of strain. The dislocation density is 2 to 3 times higher in the ternary systems than in the binary system.

During plastic deformation all systems reach a quasi steady-state where the stress remains approximately constant while the dislocation density still rises slowly. The flow stresses

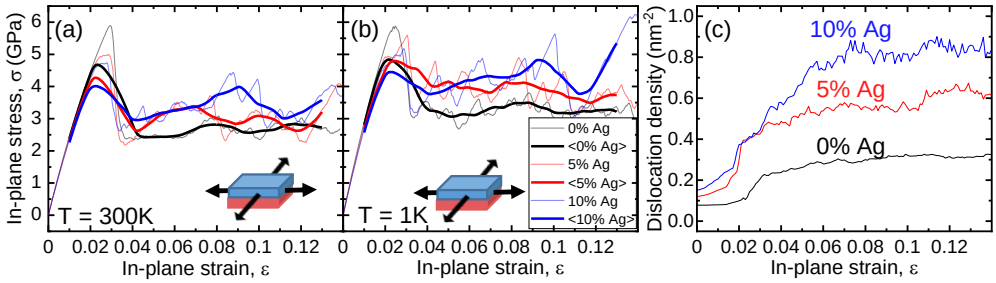

Figure 5.3: Stress-strain curves at (a) 300 K and (b) 1 K, and (c) the corresponding dislocations density at 1 K for $Cu_{1-x}Ag_x|Ni$ with $x = 0\%, 5\%, 10\%$ under an applied biaxial tensile strain along the $[112]$ and $[\bar{1}10]$ directions. Thick lines are moving averages over a strain interval ± 0.01 around the respective data point, thin lines show the full data.

reported in Tab. 5.1 are obtained by averaging the stress over an interval from 4% to 14% strain. An increase of the flow stress of approximately 20% and 25% is found for the 5% and 10% alloyed systems, respectively. Although the yield stress decreases with Ag content, the flow stress increases slightly.

A microscopic analysis of dislocation nucleation in the pure Cu|Ni multilayer system (at 1 K) is shown in Fig. 5.4 from 0% to 2.6% of deformation. At small strain, the dislocation nodes change from a perfectly planar arrangement to a structure that spreads out of plane. At higher strain (1.8%) three out of the six branches of the nodes nucleate dislocation loops, splitting a Shockley partial into a Shockley partial and a stair-rod dislocation. As the strain increases to 2.6%, the loop size increases up to the emission of one dislocation loop into the Cu layer.

5.4 Discussion

Parallel simple shear deformation. The multilayer system responds by gliding along the heterointerface in parallel shear because the Schmid factor on the interface plane is maximum. The stress oscillations observed for all the systems during simple shear deformation parallel to the interface along the [112] axis (Fig. 5.1(a,c)) can be traced to the translational invariance of the interfacial misfit dislocation network. Translation of the network by integer multiples of one unit cell vector leads to states that are indistinguishable from each other and must therefore have the same energy. The average stress over one cycle then vanishes because integrating stress over strain gives the energy difference between the two states, which must be zero because of translational invariance. Note that such periodicity is not observed with almost incoherent interfaces such as the Kurdjumov–Sachs interface in FCC/BCC multilayers where misfit dislocation can not form (Wang et al., 2008).

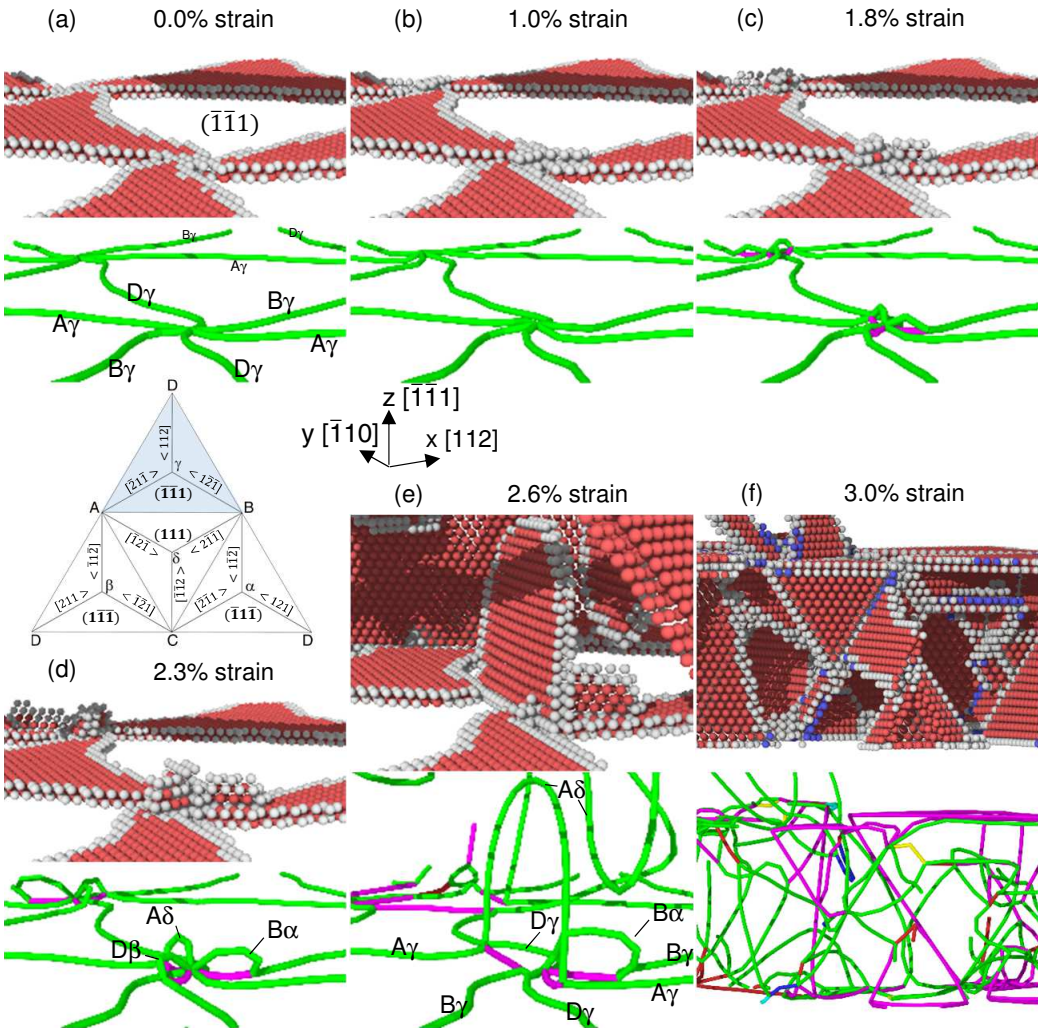

Figure 5.4: Evolution of node dislocations with applied biaxial strain to the Cu|Ni multilayer system from (a) 0% to (f) 3.0% of strain. Top row: Atoms are colored after their atomic structure environment determined by common neighbor analysis (Honeycutt and Andersen, 1987, Stukowski, 2012). FCC atoms have been removed for clarity, atoms in red are HCP and atoms in white have other local environments. Bottom row: Dislocation lines as identified by the dislocation extraction algorithm (Stukowski et al., 2012). Shockley partial dislocation are represented in green, stair-rod dislocation are represented in purple. The blue shaded region in the open Thompson tetrahedron represent the interface plane. In frame (a) and (d) the burger vectors are assigned to the Shockley partial of interest.

This conclusion is confirmed by the invariance of the dislocation densities with applied strain (Fig. 5.1(e)). No dislocations nucleate in the bulk of the layers since all the plastic deformation is accommodated at the interfaces with their pre-existing network of misfit dislocation. Note that for the ternary systems, translational invariance is broken by the presences of Ag and its segregation into clusters. This pins the dislocation network in the

multilayer interfaces and leads to an increase in flow stress even after shearing by one full lattice unit cell, while maintaining localization of shear at the heterointerface.

Pinning has also been observed to a smaller extent in two other cases. First, when comparing atomically ideal to MC/MD-relaxed systems of Cu|Ni (without Ag) under simple shear, the maximum stress differs by an order of magnitude (Fig. 5.1(a)). This difference is due to the imperfection brought into the interface by swapping some Cu atoms with Ni atoms. A direct indication that pinning comes from interface heterogeneity is given by the calculations performed with the alloy-averaged EAM approximation (described in section 2.1.2). When the heterogeneous $Cu_{1-x}Ag_x$ is replaced by a homogeneous average $\langle Cu_{1-x}Ag_x \rangle$ solid (that describes the thermodynamic properties of this solid solution correctly), the maximum stress drops by one order of magnitude close to the values obtained for the pure, ideal Cu|Ni multilayer. These results are not shown here, but they look essentially like the calculations for the pure Cu—Ni system shown in Fig. 5.1.

Similar mechanisms have been observed in CuNb|Cu multilayer system where coherent interfaces show alternating compressive and tensile stresses that can strongly hinder dislocation mobility (Gu et al., 2015). Similarly, in nanocrystalline CuAg alloys, segregated Ag at the grain boundary affects the resistance of the grain boundary to sliding and dislocation slip (Li and Szlufarska, 2017). The shear strength obtained for the FCC/FCC interfaces in such alloys can reach values similiar to those of more complex interfaces such as FCC/BCC (Wang et al., 2008, Zhang et al., 2016) that show a higher shear resistance than FCC/FCC interfaces.

Perpendicular simple shear deformation. The oscillation in the stress strain curves observed in parallel shear can also be seen when the systems are sheared perpendicularly to the multilayer interface (Fig. 5.1(b,d)). All systems accommodate the deformation at small strains by first sliding along the heterointerface although the Schmid factor for sliding along that plane is small. This is because the resistance to shear of the heterointerface is much smaller than the stress required to nucleate dislocations on the other three $\{111\}$ planes.

The dislocation density remains approximately constant in that regime (Fig 5.1(f)). The origin of the oscillatory stress-strain curves at small applied strain is identical in parallel and perpendicular shear. Note that the difference of shape observed in the feature between Fig. 5.1(a) and (b) comes from the different crystal orientation accommodating the interface strain. In the first case, the interfaces are sheared along the $[112]$ direction while in the second case the interfaces are sheared along the $[110]$ direction.

At an applied strain of around 10% and larger, the stress-strain response becomes intermittent, which is typically a sign of the presence of structural disorder. This onset of intermittency coincides with increased dislocation activity within the Cu layer but also crossing the layers (Fig. 5.1(f)). The primary source of the dislocations are the nodes of the interfacial misfit

dislocation network, whose density depends on Ag content. Structures with more Ag therefore show a more pronounced increase in overall dislocation density when sheared (Fig. 5.1(f)). Dislocations then interact with obstacles, such as bilayer interfaces, randomly-located Ag aggregates and other dislocations that are present in the bulk of the layers.

Pure systems can obviously withstand enormous elastic stress in the single layers without dislocation nucleation. The alloyed system lowers the barrier to dislocation nucleation because of interface defects and segregation that leads to stress concentration. Similar stress concentration zones are for example found in CuNb|Cu system at amorphous/crystalline interface (Gu et al., 2015). Ag segregation within the Cu layers leads to defects resulting in a higher initial dislocation density for the ternary systems (Fig. 5.1(f)). These initial defects help nucleation of clusters of stacking faults at much smaller applied strain than the pure bilayer. At strains from around 5% to 15%, deformation is confined to the heterointerface for the pure system as confirmed by the absence of pronounced dislocation production (Fig. 5.1(f) and 5.2), while the systems with 5% and 10% Ag have created stacking faults within the $Cu_{1-x}Ag_x$ layer (Fig. 5.1(f) and 5.2).

The evolution of local atomic strain γ_i, defined in section 5.3.1 and shown in Fig. 5.2, shows that during the entire deformation process, dislocation activity concentrates in the Cu-rich layer with only few Shockley partial dislocations crossing to the Ni-rich layer. These dislocations do not leave behind any stable stacking fault in that layer as one full dislocation passes but create steps at the interface. The fraction of atoms with atomic strain $\gamma_i > 0.3$ in the Ni-rich part of the system is larger for the systems with 0% and 5% Ag than the system with 10% Ag. This suggests that the interface barrier strength is larger in the latter cases.

Biaxial tensile deformation. The initial response of the system during biaxial tensile deformation leads to a yield stress much larger than for the simple shear cases. This is because during simple shear, the system can always respond by sliding along the bilayer. This mode of accommodating the deformation is suppressed in the biaxial configuration. In biaxial shear, the resolved shear stress on the interface vanishes (its Schmid factor becomes zero) because of the loading geometry. The system must nucleate dislocations to accommodate deformation plastically.

Dislocation nucleation is again aided by the presence of disorder in the form of Ag segregates. This is evident from the decrease in yield stress with increasing Ag content shown in Fig. 5.3(a,b). It can even more clearly be seen in the corresponding dislocation densities, shown in Fig. 5.3(c), which increase with increasing Ag content. From this it is evident that the alloyed system has higher dislocation density at similar strain, even when considering for the fact that the initial dislocation density (at zero strain) in the alloyed system is higher with than without Ag. Most of this increase in dislocation density happens during yielding.

The high dislocation density then leads to an inversion of the dependency on Ag content of the stress required to continuously deform the bilayer during flow. The more Ag present, the higher the flow stress, as reported in Tab. 5.1. Many of the Shockley partials that are created glide along one of the three (111), $(1\bar{1}\bar{1})$ and $(\bar{1}1\bar{1})$ planes and react to form sessile stair-rod dislocations and stacking fault tetrahedra within the layers (Jøssang and Hirth, 1966), that then act as obstacles to later dislocations and therefore strengthen the material (see Fig. 5.4(f)). The mechanism leading to the formation of stacking fault tetrahedra from the dislocations emitted at the interface nodes has been recently observed (Shao et al., 2015) in molecular dynamics simulations of binary Cu|Ni multilayers, albeit with a different EAM potential (Voter and Chen, 1986, Mishin et al., 2001, Bonny et al., 2009), and in simulations of deformation of Cu|Ag bilayer system (Yuan et al., 2013).

It is worth pointing out that the situation for simple perpendicular shear is different. As shown in Fig. 5.5(a), dislocations nucleate only on two out of the three $\{111\}$ planes. Sessile stacking fault tetrahedra therefore do not form at a rate comparable to the biaxial situation. This difference has been observed similarly for uniaxial and biaxial deformation parallel to the interface in Cu|Ni multilayers (Chen et al., 2018). The increase in flow stress with increasing Ag content (Tab. 5.1) is therefore less pronounced in simple shear than in biaxial tension.

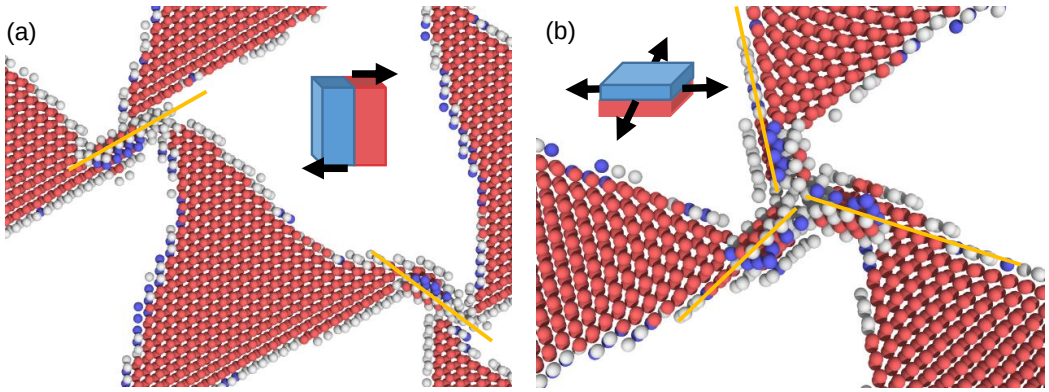

Figure 5.5: First step of dislocation emission from the nodes for the cases of (a) shear perpendicular to the interface and (b) biaxial tensile deformation parallel to the interface. Yellow lines indicate the active $\{111\}$ planes that can emit dislocations. Atoms are colored after their local crystal structure and FCC atoms have been removed for clarity: Atoms in red are HCP, atoms in blue are BCC and atoms in white have other local environments.

5.5 Summary

The direct molecular dynamics simulations have shown that increasing the Ag content (up to 10%) increases the strength of the multilayer stack. Inspection of the results yielded

three strengthening mechanisms: First, Ag clusters pin the interface dislocation network, increasing the interface resistance to shear. Second, the increase in density of the interfacial misfit dislocation network as Ag atoms are added appears to increase the resistance to dislocations crossing the interface. Third, the increase in misfit dislocation density leads to more potential sites for the nucleation of dislocations that cross the Cu layer. Dislocations nucleate at the interface nodes and react to form sessile stair-rod dislocations. These in turn act as obstacles that hinder dislocation motion and strengthen the material.

These three strengthening mechanisms are active for different deformation modes, namely simple shear parallel to the interface, simple shear perpendicular to it and biaxial tensile deformation, respectively. Tuning the lattice constant of Cu by alloying it with Ag is therefore a potential route for tuning strength of the Cu|Ni multilayer system for a variety of loading conditions.

Additionally the segregation pattern at the grain boundaries in both Cu-rich and Ni-rich in chapter 4 layer is expected to further modify the mechanical properties of the multilayer system and could be the source of an additional strengthening mechanism. Such aggregates could modify the grain boundaries slip resistance to dislocation and to a smaller extend alter the grain boundaries sliding mechanism. Similarly, an increase in flow stress has been observed by Li and Szlufarska (2017) in nanocystalline Cu-Ag alloys with a grain size smaller than 40 nm where Ag has segregated to the grain boundaries.

Part III.

Cu|Au multilayer system

6. EAM potential for Cu-Au

6.1 Introduction

The binary Cu-Au system has been studied in recent years because multilayered (phase separated) films of Cu-Au can be prepared experimentally (Borders, 1973, Paulson and Hilliard, 1977, Li et al., 2010), yet Cu-Au is miscible and forms stable intermetallic phases. The phase separated state is therefore an example of a material far from equilibrium that can be used to study alloying by mechanical action (Delogu and Cocco, 2005, Kaupp, 2009) and the influence of microstructure on mechanical properties (Misra and Krug, 2001, Wang et al., 2008, Wang and Misra, 2011). Cu and Au both crystallize in the face-centered cubic (FCC) structure. Their intermetallic phases are of mainly $L1_0$ and $L1_2$ structure (Borders, 1973).

Studying deformation processes in this binary system requires an interatomic potential that captures both mechanical and thermodynamic properties. The benchmark property for the mechanical performance of an embedded atom potential for FCC metals is the stacking fault energy (SFE) (Zimmerman et al., 2000), since deformation in FCC metals is mainly carried by dislocations that often dissociate into two Shockley partials separated by a stacking fault. The splitting distance between these partials is determined by SFE and elastic constants (Hull and Bacon, 2011).

Most of the binary Cu-Au EAM potentials found in the literature (Barrera et al., 2000, Foiles et al., 1986, Zhou et al., 2004, Ackland and Vitek, 1990) are fitted to describe thermodynamic properties and provide an approximate description of the Cu-Au binary phase diagram (Fig. 1.3), but they do not describe the energies of planar defects in pure phases well, such as stable and unstable stacking fault energies or surface energies. The present work reports an interatomic potential for the binary Cu-Au system that describes stacking faults well while conserving a reasonable description of the Cu-Au phase diagram. For this goal, the established Cu potential by Mishin et al. (2001) and the Au potential by Grochola et al. (2005) are used for the unary phases, only the Cu-Au cross interaction is fitted. This is a pragmatic approach to arrive at a potential energy expression that can be used to study mechanical deformation in the Cu-Au system. The properties of this potential are

compared to four potentials published in the literature: Ackland and Vitek (1990), Barrera et al. (2000), Zhou et al. (2004) and the universal EAM of Foiles et al. (1986).

6.2 Methods

6.2.1. Embedded-atom method

In this chapter the embedded atom method describe in section 2.1 was employed. The two established potentials used here report the three functions $F(\rho)$, $f(r)$ and $\phi(r)$ in a tabulated form (Becker et al., 2013). Values and derivatives are then computed from a third-order spline approximation to this table. Mishin's potential has been fit to experimental and *ab-initio* properties of Cu (lattice constant, heats of formation, etc.) while Grochola has adopted the force-matching approach of Ercolessi & Adams (Ercolessi and Adams, 1994) to fit the potential to *ab-initio* (density-functional theory (Martin, 2004) with the PW91 functional (Perdew et al., 1992)) data. While these fitting procedures differ in philosophy, both potentials give accurate representations of the underlying material. Table 6.1, Tab. 6.2 and Tab. 6.3 show a comparison of computed lattice parameters, elastic constants and planar defects in comparison with experimental and *ab-initio* data for the unary phases as described by these potentials.

Table 6.1: Lattice constant a_0 of the Cu and Au unary FCC phases from experiments (extrapolated to 0 K unless otherwise noted), DFT and the respective EAM potential (both at 0 K).

Element	Method	a_0 (Å)
Cu	Experimental Kittel (2005)	3.615[a]
	DFT-PW91 (Literature) (Kamran et al., 2009)	3.637
	DFT-PBE (This work)	3.637
	Mishin et al.	3.615
	Ackland et al.	3.615
	Barrera et al.	3.615
	Foiles et al.	3.615
	Zhou et al.	3.615
Au	Experimental (Kittel, 2005)	4.07
	DFT-LDA[b] (Literature) (Wang et al., 2013)	4.067
	DFT-PBE (Literature) (Wang et al., 2013)	4.175
	DFT-PBE (This work)	4.157
	Grochola et al.	4.070
	Ackland et al.	4.078
	Barrera et al.	4.079
	Foiles et al.	4.080
	Zhou et al.	4.080

[a] At 300 K ; [b] Local density approximation (LDA).

Table 6.2: Cubic elastic constants C_{11}, C_{12} and C_{44} and bulk modulus B of the unary FCC phases from experiments (at 0 K) and the respective EAM potential (at 0 K). Elastic constants were obtained from a finite-differences approximation of the derivative of the stress tensor using a strain increment of 10^{-6}. All results are given in GPa

Element	Method	C_{11}	C_{12}	C_{44}	B
Cu	Experimental[a]	176	125	82	142
	DFT-PW91[b] (Literature)	177	130	82	145
	DFT-PBE (This work)	179	126	78	143
	Mishin et al.	170	122	76	138
	Ackland et al.	169	122	76	137
	Barrera et al.	163	117	75	132
	Foiles et al.	167	124	76	139
	Zhou et al.	178	128	78	145
Au	Experimental[a]	202	170	45	180
	DFT-LDA[c] (Literature)	198	185	56	189
	DFT-PBE[c] (Literature)	147	136	40	140
	DFT-PBE (This work)	155	130	26	138
	Grochola et al.	202	169	46	180
	Ackland et al.	187	157	42	167
	Barrera et al.	186	148	49	161
	Foiles et al.	183	159	45	167
	Zhou et al.	188	158	43	168

[a] Simmons et al. (1971) ; [b] Kamran et al. (2009) ; [c] Wang et al. (2013) .

Table 6.3: Energies of planar defects in the unary FCC phases. The table reports the stacking fault energy γ_{SF}, the unstable stacking fault energy γ_{USF} and the energies of free {100}, {110} and {111} surfaces (γ_{100}, γ_{110} and γ_{111}, respectively). Values in parenthesis are computed without atomic relaxation. Values in curly brackets are corrected DFT values using the technique described in (Mattsson et al., 2006). Experimental and previous *ab-initio* calculation results are shown when available. All the results are in mJ m^{-2}. Large deviations between theoretical and experimental data are shown in bold and discussed in the main text.

Element	Method	γ_{SF}	γ_{USF}	γ_{100}	γ_{110}	γ_{111}
Cu	Experimental	45-75[a]	-	1790[b]	1790[b]	1790[b]
	DFT (Literature)	39[c]	158[c]	1460 (1470) {2270}[d]		1320 (1320) {2130}[d]
		43[e]	175[e]			
		49[f]	210[f]			
	DFT-PBE (This work)	51 (51)	161 (179)	1408 (1423) {2021}	1495 (1539) {2108}	1223 (1226) {1836}
	Mishin et al.	44.4 (44.8)	162 (180)	1347 (1352)	1478 (1492)	1241 (1248)
	Ackland et al.	46.4 (52.1)	**289** (**297**)	1135 (1144)	1230 (1253)	**960** (**969**)
	Barrera et al.	**17.8** (**17.8**)	154 (159)	1331 (1354)	1446 (1473)	1225 (1254)
	Foiles et al.	**17.4** (**17.8**)	141 (157)	1288 (1291)	1413 (1427)	1181 (1185)
	Zhou et al.	22.6 (39.8)	110 (179)	1563 (1566)	1744 (1756)	1502 (1505)
Au	Experimental	32-40[a]	-	1506[b]	1506[b]	1506[b]
	DFT (Literature)	27[e]	94[e]	1450[d]		1250[d]
	DFT-PBE (This work)	36 (39)	87 (103)	835 (840) {1261}	883 (894) {1309}	646 (648) {1072}
	Grochola et al.	42.6 (42.7)	92 (98)	1296 (1439)	1530 (1735)	1196 (1281)
	Ackland et al.	31.7 (44.3)	**219** (**296**)	**769** (**794**)	**814** (**871**)	**622** (**644**)
	Barrera et al.	**-1.5** (**-1.3**)	117 (136)	**683** (**766**)	**738** (**851**)	**577** (**645**)
	Foiles et al.	**4.8** (**4.8**)	95 (103)	914 (976)	977 (1094)	785 (827)
	Zhou et al.	**3.3** (**5.1**)	86 (106)	1015 (1083)	1109 (1236)	907 (952)

[a] Yan and Zhang (2013) ; [b] Tyson and Miller (1977), extrapolated to 0 K for average orientation.
[c] PW91, Ogata et al. (2002) ; [d] PW91, Swart et al. (2007) ; [e] PBE, Wu et al. (2010) ; [f] LDA, Zimmerman et al. (2000).

6.2.2. Ab-initio calculations

The reference values were computed using density functional theory (DFT). These calculations were carried out using the Vienna ab-initio Simulation Package (VASP version 5.3.2) (Kresse and Hafner, 1993, Kresse and Furthmüller, 1996b,a). The projector-augmented wave (PAW) (Blöchl, 1994) method was used to represent frozen core electrons and the Perdew–Burke–Ernzerhof (PBE) (Perdew et al., 1996) exchange correlation functional. For both elements the standard potentials distributed with VASP with PAW electronic configuration [Ar] $3d^{10}$ $4p^1$ for Cu and [Xe] $4f^{14}$ $5d^{10}$ $6s^1$ for Au were used. All calculations were spin-paired. The wavefunctions were expanded into plane waves up to an upper energy cutoff of 500eV. The Brillouin-zone was sampled with a 15x15x15 k-points mesh distributed according to the sampling scheme of Monkhorst and Pack (1976) for bulk properties (lattice constants, elastic constants, etc.). For systems containing planar defects (stacking faults or surfaces) an 11x1x11 Monkhorst and Pack mesh was used. Energy level were populated using the method of Methfessel and Paxton (1989) with a smearing width of 0.2 eV.

6.2.3. Stacking fault energies

The intrinsic stacking fault is a lattice defect that breaks the stacking sequence ...ABCABCABC... of $\{111\}$ planes in the FCC structure to ...ABCABABC.... Atoms in the stacking fault are locally in a hexagonal close packed (HCP) environment. The energy for forming this defect is positive and called the stacking fault energy (SFE).

Stacking faults can be characterized by the γ-surface (Vítek, 1968), the potential energy surface that is obtained by rigidly displacing a crystalline block of atoms parallel to a $\{111\}$ plane. In the case of an FCC structure the local minima of the γ-surface in the $\langle 112 \rangle$ direction are stable stacking faults and the respective energy is the SFE. Saddle points are called unstable stacking faults. For the $L1_2$ structure the γ-surface is more complex. The local minima correspond successively to the complex stacking fault (CSF) energy (at $\frac{a_0}{6}[11\bar{2}]$), the antiphase boundary (APB) energy (at $\frac{a_0}{2}[11\bar{2}]$) and the superlattice intrinsic stacking fault (SISF) energy (at $\frac{2a_0}{3}[11\bar{2}]$) (Reed, 2008). For the $L1_0$ structure one can find the SISF energy at $\frac{a_0}{6}[11\bar{2}]$ and the CSF at $\frac{a_0}{12}[\bar{1}\bar{1}2] + \frac{a_0}{4}[1\bar{1}0]$ (Paidar and Vitek, 2002). In an atomistic calculation, the stacking fault energy γ_{SF} can be computed from

$$\gamma_{\mathrm{SF}} = \frac{E_{\mathrm{SF}} - E_0}{A} \tag{6.1}$$

where E_{SF} is the energy of the crystal with defect (HCP stacking fault in this case), E_0 is the energy of the perfect lattice (FCC in this case), and A is the area of the stacking fault.

All stacking fault energies reported here were computed at 0 K. The systems were composed of 12 atomic layers with two free surfaces separated by a 15 Å vacuum. The x, y and z axis of the simulation box were oriented along the [112], [$\bar{1}$10] and [$\bar{1}\bar{1}$1] directions, respectively. The upper six atomic layers were then rigidly displaced in the [112] direction while computing the energy.

In order to quantify the effect of lattice relaxation, additional calculations were carried out where relaxation of atoms along the [$\bar{1}\bar{1}$1] direction was allowed. These calculations were run for only the EAM potentials and used larger crystalline blocks of approximately 48,000 atoms originally in perfect FCC stacking. A conjugate gradient minimizer was used and optimized until the length of the global force vector of the system dropped below 10^{-6} eV Å^{-1}.

6.2.4. Surface energies

The surface energy is the energy of another planar defect, the interface of the crystal with vacuum. Its energy represents the work required to create a free surface from a perfect FCC bulk on a given (hkl) plane. Similarly to the stacking fault definition, surface energies can be computed from

$$\gamma_{hkl} = \frac{E_{hkl} - E_0}{2A} \tag{6.2}$$

where E_{hkl} is the energy of the crystal with two free surfaces, E_0 is the energy of the perfect lattice (FCC in this case), and A is the area of the two planar faults created.

All surface energies reported here are computer at 0 K. The surface energies were computed for three low-index crystallographic planes $\{100\}$, $\{110\}$ and $\{111\}$. In *ab-initio* calculations the systems used were similar to the one used for the SFE calculations. The systems were set up such that at least 30 Å separated the two free surfaces. A stack of 8 crystalline layers was used for the (100) orientation, 12 layers for the (110) orientation and 9 layers for the (111) orientation. Free surfaces were relaxed using a conjugate gradient minimizer until the length of the global force vector of the system dropped below 10^{-3} eV Å^{-1}.

The energies of (free) surfaces computed from DFT calculations using both LDA or GGA approximations typically underestimate the corresponding experimental values. The correction by Mattsson et al. (2006) was applied to the DFT surface energy results. This correction uses the intrinsic error of the corresponding functional (PBE in this case) as computed for the Jellium surface (for which high-quality random phase approximation data is available (Yan et al., 2000, Pitarke and Eguiluz, 2001)) to correct the surface energy of DFT calculations.

6.2.5. Nested sampling

The nested sampling calculations used unit cells containing 64 atoms. $K = 2400$ phase space configurations were used. The nested sampling algorithm was stopped when the expectation value of the temperature dropped below 100 K. One configuration per iteration was removed and the new uncorrelated configuration was generated with a Monte-Carlo (MC) walk of 640 MC moves. The MC walk was a repeating sequence of eight N-particle moves, 16 cell volume moves, eight MC cell shear moves, eight cell stretch moves and eight atom swaps. Then $\chi(\varepsilon)$ was used to compute the heat capacity $C_p(T)$ as a function of temperature T. Peaks within $C_p(T)$ indicate phase transitions. These peaks were fitted with Gaussians. This yields the transition temperatures and a measure for their error.

6.3 Fitting the cross potential

The two unary EAM potentials of Mishin and Grochola were used as the starting point for the new binary Cu-Au EAM potential. A simplified procedure for determining the cross term was adopted, inspired by the (Lorentz-Berthelot) type mixing rules that are commonly used for cross terms in Lennard-Jones type potentials, but also the embedded atom method (e.g. Foiles et al. (1986)) or empirical bond-order potentials (e.g. Tersoff (1988)). Rather than employing a simple mix that treats the contribution of both species equally (either through arithmetic or geometric averages), mixing parameters were fitted. This leads to small set of fitting parameters while still giving some flexibility for the target properties to be reproduced.

Specifically, this expression was used

$$\phi_{\mathrm{CuAu}}(r) = \alpha_{\mathrm{Cu}} \cdot \phi_{\mathrm{CuCu}}(r) + \alpha_{\mathrm{Au}} \cdot \phi_{\mathrm{AuAu}}(r) \tag{6.3}$$

for the repulsive pair potential in Eq. (2.2). Here, $\phi_{\mathrm{CuAu}}(r)$ is the pairwise interspecies potential and $\phi_{\mathrm{CuCu}}(r)$ and $\phi_{\mathrm{AuAu}}(r)$ are the pairwise potentials for the pure species (i.e. Mishin's and Grochola's estimates for those). The coefficients α_{Cu} and α_{Au} are the mixing parameters and fit using the procedure described below. Note that Eq. (6.3) conserves the symmetry of $\phi_{\sigma_i\sigma_j}(r)$ with respect to exchange of the indices σ_i and σ_j.

The local electron densities were obtained from the functions

$$f_{\mathrm{Au|Cu}}(r) = \beta_{\mathrm{Cu}} \cdot f_{\mathrm{Cu|Cu}}(r) + \gamma_{\mathrm{Cu}} \cdot f_{\mathrm{Au|Au}}(r) \tag{6.4}$$

$$f_{\mathrm{Cu|Au}}(r) = \beta_{\mathrm{Au}} \cdot f_{\mathrm{Au|Au}}(r) + \gamma_{\mathrm{Au}} \cdot f_{\mathrm{Cu|Cu}}(r) \tag{6.5}$$

where $f_{\mathrm{Au|Cu}}(r)$ and $f_{\mathrm{Cu|Au}}(r)$ are the missing cross terms.

The coefficients in Eqs. (6.3), (6.4) and (6.5) were fitted to experimental data for each of the intermetallics. The (experimental) target properties for the Cu_3Au, CuAu and $CuAu_3$ phases are marked with a dagger in Tab. 6.4 and Tab. 6.5.

The cross potential was fitted by minimizing a cost function Q with respect to the model parameters using the downhill simplex method of Nelder and Mead (Nelder and Mead, 1965). The cost function was a sum of the weighted residuals for each targeted physical constant,

$$Q = \sum_i (\delta_i \cdot w_i)^2, \quad \delta_i = v_{i,\mathrm{EAM}} - v_{i,0}, \tag{6.6}$$

where i is the i-th physical constant value to fit, $v_{i,\mathrm{EAM}}$ and $v_{i,0}$ are the computed and targeted physical constants, respectively, and w_i is a weighting coefficient. The initial values entering Eqs. (6.3), (6.4) and (6.5) are taken as $\alpha_{\mathrm{Cu}} = \alpha_{\mathrm{Au}} = \beta_{\mathrm{Cu}} = \beta_{\mathrm{Au}} = \gamma_{\mathrm{Au}} = \gamma_{\mathrm{Cu}} = 0.5$ with the weight coefficients defined in Tab. 6.6. The lattice constant of the $L1_2$ phase did not require a high weight as the value from the initial guess already agreed well with experimental data. For the $L1_0$ a high weight was required to obtain the correct c/a ratio. A particular focus was put on the enthalpy of mixing in order to conserve thermodynamic properties. The c/a ratio was constrained to be smaller than 1. An initial fit gave values for the prefactors γ_{Cu} and γ_{Au} smaller than 0.01. The fit was then reran at fixed $\gamma_{\mathrm{Cu}} = 0$ and $\gamma_{\mathrm{Au}} = 0$. This produced the final prefactors reported in Tab. 6.7.

Table 6.4: Lattice constant a_0 for the cubic $L1_2$ phases, lattice constants a_0 and c_0 for the tetragonal $L1_0$ phase and enthalpy of mixing ΔH_{mix} of the Cu-Au binary phases from experiments at 0 K, DFT and the respective EAM potential (at 0 K). Large deviations between theoretical and experimental data are shown in bold and discussed in the main text. The values marked with a dagger are fitting targets for the potential. The error relative to the experimental enthalpy of mixing at 0 K is given in percent in the last column.

Phase	Method	a_0 (Å)	c_0 (Å)	c/a	ΔH_{mix} (eV/atom)	Error (%)
Cu_3Au ($L1_2$)	Experimental	3.74†[a]			-0.074†[b]	–
	DFT (Literature)	3.725[c]			–	–
	DFT-PBE (This work)	3.784			-0.048	35
	EAM (This work)	3.735			-0.072	3
	Ackland et al.	3.748			-0.071	4
	Barrera et al.	3.726			-0.081	9
	Foiles et al.	3.753			-0.051	31
	Zhou et al.	3.750			-0.093	26
CuAu ($L1_0$)	Exp	3.966†[d]	3.673†[d]	0.93†	-0.091†[b]	–
	DFT-PBE (This work)	4.061	3.679	0.91	-0.058	36
	EAM (This work)	3.852	3.803	0.99	-0.092	1
	Ackland et al.	3.899	3.902	**1.00**	-0.071	22
	Barrera et al.	3.944	3.653	0.93	-0.094	3
	Foiles et al.	3.070 **(B2)**	–	–	-0.082	10
	Zhou et al.	3.941	3.715	0.94	-0.133	46
$CuAu_3$ ($L1_2$)	Experimental	3.98†[a]			-0.059†[b]	–
	DFT-PBE (This work)	4.047			-0.028	53
	EAM (This work)	3.941			-0.060	2
	Ackland et al.	3.997			-0.057	3
	Barrera et al.	3.960			-0.052	12
	Foiles et al.	3.982			-0.035	41
	Zhou et al.	3.976			-0.095	61

[a] Kittel (2005) ; [b] Ozoliņš et al. (1998) ; [c] Wang et al. (2013), calculated with the revised PBE functional of Perdew et al. (2008) ; [d] Barrera et al. (2000), at 300 K.

6.4 Tests of the binary potential

6.4.1. Lattice parameters and elastic constants

The physical properties (enthalpy of mixing, lattice constants, elastic constants) obtained for the ordered phases in the potential described here are shown in Tab. 6.4 and 6.5. The enthalpies of mixing are in good agreement with the experimental values with differences of less than 2 meV for the $L1_2$ phases. The lattice constants for the $L1_2$ phases are within a 1% range from the experimental values. The potential predicts a slightly deformed version of the tetrahedral $L1_0$ phase with a 2% smaller a_0 lattice vector and a 2% larger c_0 lattice vector, while keeping a c_0/a_0 ratio smaller than one (consistent with the $L1_0$ structure) and almost no error in density (differs by 0.2%). While structure and formation energy is excellently described by the EAM potential, the elastic constants (Tab. 6.5) for the intermetallic $L1_2$ phases phases are overestimated by $\sim 17\%$ ($CuAu_3$) and $\sim 22\%$ (Cu_3Au).

Existing EAM potentials manage to describe properly the elastic constants for the Cu and Au pure phases. The potentials from Ackland and Vitek (1990), Barrera et al. (2000), and Foiles et al. (1986) successfully describe the elastic properties of the Cu_3Au $L1_2$ phase, while the potential from Zhou et al. (2004) slightly underestimates the elastic constants for this phase. The potential from Ackland and Vitek (1990) overestimates the elastic constants for the $CuAu_3$ $L1_2$ phase when the three other correctly describe the elastic constant for this phase.

6.4.2. Stacking fault energies

Figure 6.1 shows the energy of the fault as a function of the relative displacement of the two ideal crystals bounding the stacking fault. For the Cu, Au and CuAu single crystals, the intrinsic SFE (γ_{SF}) is defined as the first minimum of the curve. For the Cu_3Au and $CuAu_3$ curve the first minimum corresponds to the complex SFE (γ_{CSF}). The unstable SFE to nucleate the leading partial can be identified as the first maximum of the curve (Xie et al., 2014).

Table 6.3 reports experimental planar defect energies (Yan and Zhang, 2013, Ogata et al., 2002) and values obtained for the unary Cu and Au EAM potentials of Mishin et al. (2001) and Grochola et al. (2005) as well as the binary Cu-Au EAM potentials of Ackland and Vitek (1990), Barrera et al. (2000), Zhou et al. (2004) and the universal EAM of Foiles et al. (1986) for the unary phases. Both Mishin et al. (2001) and Grochola et al. (2005), and hence also the binary potential presented here, agree well with experimental and DFT data for stacking fault and unstable stacking fault energies. Except for Ackland and Vitek (1990), the

Table 6.5: Independent elastic constants and bulk modulus B of the $L1_2$ and $L1_0$ phases from experiments (at 0 K) and the respective EAM potential (at 0 K). Elastic constants were obtained from a finite-differences approximation of the derivative of the stress tensor using a strain increment of 10^{-6}. All results are given in GPa. The values marked with a dagger are fitting targets for the potential. The averaged error relative to the experimental value over all the elastic constant is given in percent in the last column.

Phase	Method	C_{11}	C_{12}	C_{44}	B	
Cu_3Au ($L1_2$)	Experimental[a]	189†	132†	74†	150	–
	DFT[b] (Literature)	198	154	91	169	13
	DFT-PBE (This work)	178	120	65	139	9
	EAM (This work)	236	172	78	194	22
	Ackland et al.	177	126	65	143	7
	Barrera et al.	174	124	66	140	8
	Foiles et al.	175	140	60	151	8
	Zhou et al.	124	107	47	112	29
$CuAu_3$ ($L1_2$)	Experimental[a]	189†	155†	47†	166	–
	DFT-PBE (This work)	157	123	36	134	20
	EAM (This work)	220	193	50	202	17
	Ackland et al.	269	192	96	218	50
	Barrera et al.	194	149	57	164	7
	Foiles et al.	181	155	47	164	1
	Zhou et al.	192	150	55	164	6

Phase	Method	C_{11}	C_{22}	C_{12}	C_{13}	C_{44}	C_{55}
CuAu ($L1_0$)	DFT-PBE (This work)	264	269	157	272	189	37
	EAM (This work)	228	250	176	186	71	70
	Ackland et al.	214	280	184	158	84	100
	Barrera et al.	198	148	144	127	59	59
	Foiles et al. (B2)	171	–	154	–	58	–
	Zhou et al.	183	130	126	128	60	50

[a] Simmons et al. (1971) ; [b] Wang et al. (2013).

Table 6.6: Weight coefficients used in Eq. (6.6) to fit to the experimental target data tabulated in Tabs. 6.4 and 6.5. Fitting targets marked with a dagger in Tabs. 6.4 and 6.5.

Phase	Cu_3Au	CuAu	$CuAu_3$
Structure	$L1_2$	$L1_0$	$L1_2$
a_0	1	20	1
c_0		40	
c/a		80	
ΔH_{mix}	30	30	30
C_{11}	10		10
C_{12}	10		10
C_{44}	10		10

Table 6.7: Optimized set of mixing parameters for the binary EAM potential.

	Au	Cu
α	0.397	0.857
β	0.699	1.124
γ	0	0

binary Cu-Au potentials underestimate the SFE of Au by an order of magnitude and the SFE of Cu by at least a factor of two. Conversely, while all potentials give unstable SFEs that agree well with DFT, Ackland and Vitek (1990) gives unstable stacking fault energies about a factor of two larger than the reference DFT calculations.

The complex stacking fault (CSF) and superlattice intrinsic stacking fault (SISF) energies obtained for the binary phases were compared with DFT calculation. Results are summarized in Tab. 6.8. All stacking fault values obtained for ordered phases with the fitted potential are positive. The values for the $L1_2$ phases are underestimated by a factor of two to three. The values for the $L1_0$ phases are underestimated by a factor of six to seven. Both Ackland and Vitek (1990) and Zhou et al. (2004) yield reasonable values for the stacking faults of these three compounds (to within a factor of three of the DFT calculations). Barrera et al. (2000) and Foiles et al. (1986) give negative SISF energies for the $CuAu_3$ $L1_2$ structure. This indicates that $CuAu_3$ is not $L1_2$ is these potentials. Barrera et al. (2000) does additionally have a SISF energy for CuAu that is close to zero, also indicating a problem with the stability of the $L1_0$ CuAu phase in this potential.

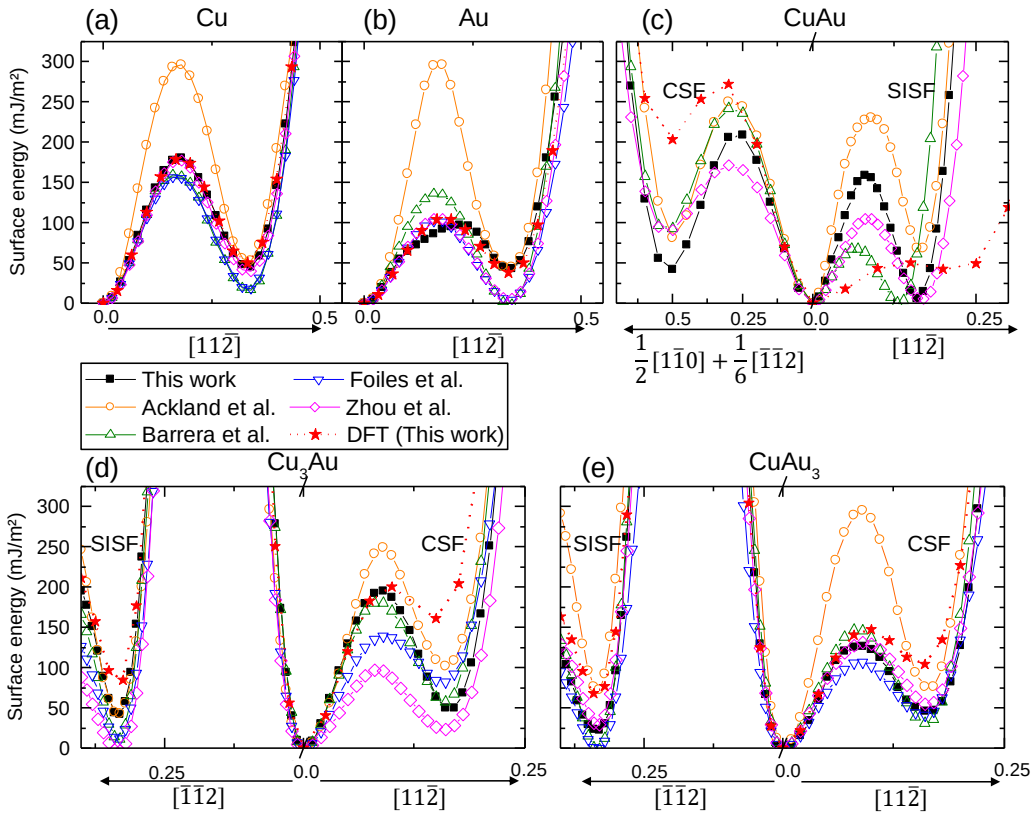

Figure 6.1: Generalized stacking fault energies of the single crystal Cu, Cu_3Au, CuAu, $CuAu_3$ and Au (without $\langle 111 \rangle$ axis relaxation for all calculations) for the potentials considered in this work and DFT calculations. The directions of the rigid displacements within the corresponding (111) plane are indicated in the axis labels.

Table 6.8: Energies of planar defects in the binary phases. The table reports the complex stacking fault energy γ_{CSF}, the superlattice intrinsic stacking fault energy γ_{SISF} and the energies of free $\{100\}$, $\{110\}$ and $\{111\}$ surfaces (γ_{100}, γ_{110} and γ_{111}, respectively). Previous *ab-initio* calculation results are shown when available. Values in parenthesis are computed without atomic relaxation. All the results are in mJ m^{-2}. Large deviations between *ab-initio* and EAM data are shown in bold and discussed in the main text.

Phase	Method	γ_{CSF}	γ_{SISF}	γ_{100}	γ_{110}	γ_{111}
Cu_3Au	DFT	260[a] ; 369[b] ; 227[c]	120[a] ; 199[b]			
($L1_2$)	DFT-PBE (This work)	133 (161)	76.7 (79.4)	1274 (1294)	1301 (1385)	1074 (1086)
	EAM (This work)	17.6 (48.5)	20.4 (41.0)	1408 (1456)	1576 (1655)	1317 (1354)
	Ackland et al.	48.8 (102.5)	40.6 (42.4)	1020 (1044)	1100 (1145)	864 (882)
	Barrera et al.	47.3 (58.3)	10.9 (10.9)	1145 (1164)	1235 (1266)	1031 (1044)
	Foiles et al.	58.2 (82.3)	11.2 (11.5)	1122 (1155)	1223 (1288)	997 (1028)
	Zhou et al.	19.9 (24.0)	**-3.4** (**-3.3**)	1475 (1484)	1626 (1669)	1372 (1385)
CuAu	DFT (This work)	167 (201)	35.9 (40.5)	1071 (1091)	1121 (1222)	906 (937)
($L1_0$)	EAM (This work)	22.3 (40.5)	5.8 (6.3)	1445 (1512)	1592 (1680)	1311 (1383)
	Ackland et al.	46.0 (80.8)	65.2 (65.5)	982 (1021)	976 (1060)	584 (775)
	Barrera et al.	75.3 (89.2)	**0.6** (**0.6**)	1014 (1041)	1038 (1098)	1398 (1600)
	Zhou et al.	81.6 (88.8)	22.8 (22.9)	1384 (1408)	1483 (1552)	1235 (1263)
$CuAu_3$	DFT	220[b]	119[b]			
($L1_2$)	DFT (This work)	88.7 (104)	57.8 (65.6)	960 (986)	973 (1070)	774 (798)
	EAM (This work)	39.6 (46.1)	21.4 (21.9)	1360 (1454)	1564 (1727)	1263 (1328)
	Ackland et al.	51.2 (73.8)	61.6 (71.9)	849 (885)	907 (970)	702 (731)
	Barrera et al.	26.4 (30.9)	**-1.7** (**-1.7**)	807 (854)	866 (941)	696 (729)
	Foiles et al.	31.6 (41.0)	**-0.8** (**-0.7**)	951 (1019)	1016 (1144)	816 (871)
	Zhou et al.	50.5 (54.7)	27.6 (28.8)	1186 (1235)	1295 (1393)	1067 (1103)

[a] Paxton (1992), full-potential LMTO calculations using the local-density approximation without relaxation.
[b] Rosengaard and Skriver (1994), tight-binding LMTO calculations without relaxation.
[c] Paxton and Sun (1998), full-potential LMTO calculations using the local-density approximation without relaxation.

6.4.3. Surface energies

The $\{100\}$, $\{110\}$ and $\{111\}$ surface energies are well described by all EAM potentials (Tab. 6.8) except for Barrera et al. (2000) that underestimates the values for Cu and Au by a factor of two or more and Ackland and Vitek (1990) that gives values for Au equal to half of the experimental or DFT values.

6.4.4. Binary phase diagram

The phase diagram of Cu-Au is explored using the nested sampling method. The heat capacity (at constant pressure) was computed as a function of temperature, $C_P(T)$ for alloy compositions with 0, 25, 50, 75 and 100 at.% Cu. For the potential presented here 9, 34, 66 and 91 at.% Cu are additionally considered. A typical $C_P(T)$ curve derived from one of theses calculations is shown in the inset of Fig. 6.2. Each peak indicates a first order phase transition. The location of these individual peaks is reported along the experimental phase diagram shown in Fig. 6.2. A Gaussian was fitted to the peaks in the $C_P(T)$ curves to determine mean and error of the transition temperature. The error bars shown in Fig. 6.2 are the standard deviation of this Gaussian.

The phase diagrams were computed for the EAM potentials listed in Tab. 6.3 as well as the fitted potential. Compared to experimental values (Massalski et al., 1990), the nested sampling calculations show that Grochola et al. slightly underestimates the melting point of Au (by around 100 K) and Mishin et al. overestimates the melting point of Cu (by around 100 K). There are only two potentials with a clear depression of the melting point at intermediate composition, Foiles et al. (1986) and Ackland and Vitek (1990). Both, however underestimate the melting points of the binary phases by more than 150 K. (All other potentials are within 100 K of the experimental melting point.) The potential by Ackland and Vitek (1990) shows two phase transitions for the pure Au phase which should have just a transition from FCC to the melt. The first transition (at high temperature) corresponds to the transition from the liquid state to an ordered BCC-rich phase, the second point corresponds to a solid phase transition to a pure FCC structure.

The potential described here shows a clear transition from solid solution to ordered intermetallic phases. These transitions from solid solution to ordered $L1_2$ and $L1_0$ phases are described by almost all EAM potentials at temperatures about half the experimental values, except for the correct prediction of the transition temperature at 50 at.% Cu by Foiles et al. (1986). Only the potential by Ackland and Vitek (1990) severely overestimates the temperatures of the solid phase transitions of the $CuAu_3$ and CuAu phases.

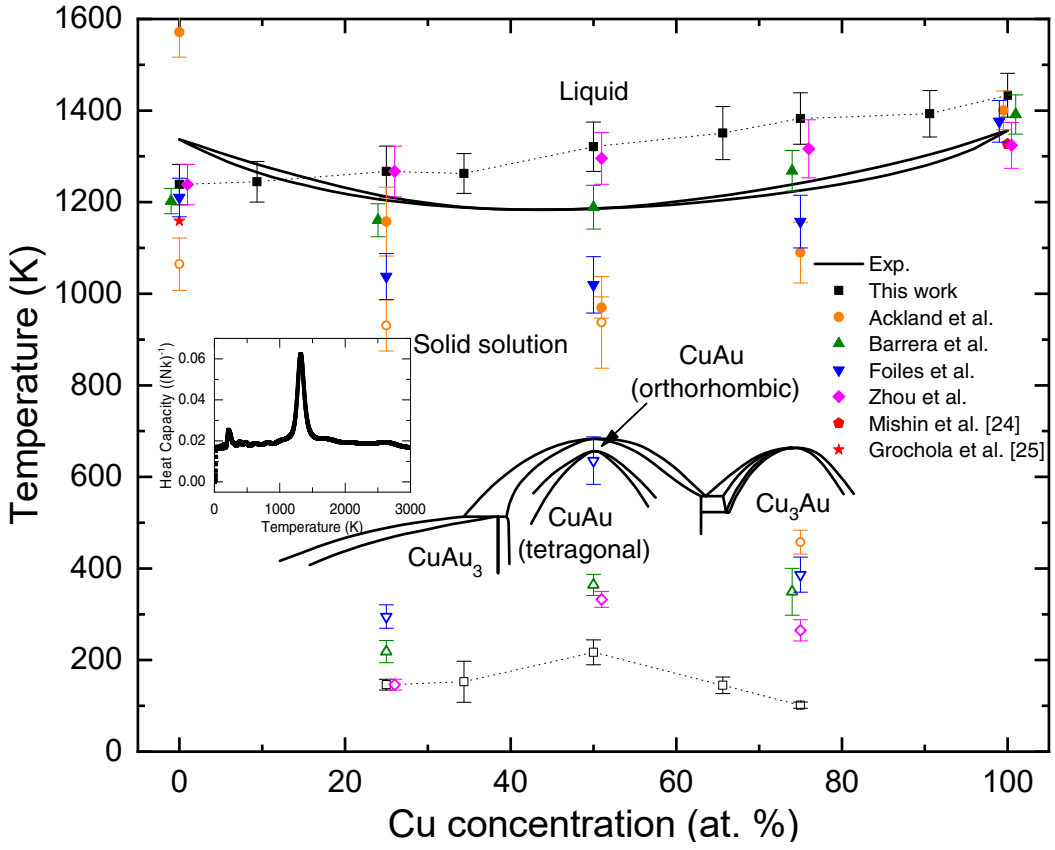

Figure 6.2: Phase diagram of the Cu-Au system. Solid lines are experimental data from Ref. (Massalski et al., 1990). Red data points show melting points reported in (Mishin et al., 2001, Grochola et al., 2005). All other results were computed using nested sampling. Full symbols represent liquid to solid transition, open symbols represent solid phase transitions. The dotted line connects data points and is a guide the eye. The inset exemplarily shows the nested sampling result of the heat capacity $C_p(T)$ for CuAu and the EAM potential of this work. Phase boundaries in the diagram are the positions of peaks of this curve. Overlapping points have been offset slightly in the concentration axis for clarity.

The structure of the low-temperature phases obtained from the nested sampling calculations are inspected, for those structures that show negative stacking fault energies. Note that a total of $K = 2400$ ground state configurations for each composition. Automatic classification of binary lattice structures is difficult and here are only reported structures manually inspected and analyzed with a combination of the adaptive common neighbor analysis (Honeycutt and Andersen, 1987, Stukowski, 2012) and polyhedral template matching (Larsen et al., 2016).

The potential of Barrera et al. (2000) forms an HCP phase for pure Au at low temperatures, consistent with the negative SFE for FCC Au (see table 6.3) which indicates that the FCC phase is not the ground state. Similarly, CuAu $L1_0$ has a close to zero SISF energy in Barrera et al. (2000) and might therefore be metastable. The low-temperature intermetallic for this

composition found by the nested sampling calculations gives an HCP-like structure and not $L1_0$. The negative SISF energies of the $CuAu_3$ ($L1_2$) phase in Barrera et al. (2000) and Foiles et al. (1986) are in agreement with the nested sampling ground state, where mixed HCP/FCC-like structures are obtained in both cases at low-temperature. For the potential of Foiles et al. (1986), the CuAu phase collapses into a B2 (BCC-like) structure when starting from an $L1_0$ structure during a cell shape and volume optimization. This ground state is confirmed by inspecting the nested sampling calculations. The Cu_3Au ($L1_2$) phase in Zhou et al. (2004) has a negative superlattice SISF energy. Consistent with this, the nested sampling calculations predict an HCP-like structure as the ground state at low-temperature.

6.5 Summary

Capturing all the features of a complex system such as a binary alloy with a simple potential energy expression is a difficult task. There are numerous existing EAM parameterizations for the Cu-Au system in the literature, four of which (Ackland and Vitek, 1990, Barrera et al., 2000, Zhou et al., 2004, Barrera et al., 2000) have explicitly been tested here. Each of the potentials manages to describe a part of the properties spectrum. Ackland and Vitek (1990) gives good SFEs but does not describe the phase diagram well. The other three potentials (Barrera et al., 2000, Zhou et al., 2004, Barrera et al., 2000) give a good reproduction of the phase diagram but underestimate SFEs. The most significant failure of all of the potentials tested here is that they do not describe the correct ground-state for some of the binary phases.

The new potential presented here as a mix between the Cu potential of Mishin et al. (2001) and the Au potential of Grochola et al. (2005) gives a good description of both SFEs and the phase diagram. In particular, this new potential gives reasonable energies for planar defects energies (stacking faults and surfaces), with the exception of the CuAu $L1_0$ phase where the SFE is underestimated by 85% with respect to DFT calculations. Its thermodynamic properties (enthalpy of mixing) for the binary Cu-Au system are consistent with DFT data. The melting temperature is predicted within a 100 K of the experimental values across the full concentration range. Disordered solid solution to ordered phase transitions exist for all concentrations. Lattice constants deviate by 0.3%-3% from experimental values and the c/a ratio for the $L1_0$ tetrahedral CuAu phase is below unity. Elastic constants are in good agreement with experiment for the pure phases and within a 5%-30% error range for the binary phases.

7. Monocrystalline layers: Structure

7.1 Introduction

In this chapter the EAM potential developed and described in the previous chapter is used. The structure of dislocation networks at the Cu|Au interfaces is studied as a function of the width of the intermixing between two layers. Then the influence of intermixing on the mechanical properties is investigated.

For non-miscible metals such as Cu and Ni, the heterointerface is often semi-coherent, consisting of a network of Shockley partial dislocations separated by stacking faults (Cheng et al., 2007, Shao et al., 2013). The structure for heterointerfaces of miscible compounds such as Cu|Au is less clear because of the tendency of the interface to diffusively intermix. The concentration then varies continuously from one side to the other.

Phase separated films of Cu-Au have been prepared experimentally for decades (Borders, 1973, Paulson and Hilliard, 1977, Li et al., 2010). Cu and Au both crystallize in the face-centered cubic (FCC) structure. They are miscible and form stable intermetallic phases as shown in the CuAu binary phase diagram (Fig. 1.3). The phase separated state is therefore an example of a material far from equilibrium. Intermixing of the two species can experimentally occur for several reasons. The first one being intermixing during the growth of a Cu|Au multilayer system. Chambliss and Chiang (1992) have shown that a half monolayer of Au deposited on Cu(110) substrate would form a $Cu_3Au(100)$ surface. Similarly, Chistjakov et al. (1988) have observed CuAu intermixing width up to tens of nanometer using a thermal deposition method. This intermixing can be further amplified

by aging the sample, e.g. annealing or irradiating (Chistjakov et al., 1988, Myagkov et al., 2009).

7.2 Interface model

Atomistic simulations were used to study the interface between Cu and Au in these multilayers. The initial system was composed of two perfect crystals of Cu and Au stacked along the $[\bar{1}\bar{1}1]$ directions (Fig. 7.1(a)). The height of each crystal was approximately 25 nm. The two other axes of the orthorhombic simulation cell were oriented along the $[112]$ and the $[\bar{1}10]$ directions for both crystals. The simulation box was periodic along the $[112]$ and $[\bar{1}10]$ directions, with a free boundary in the $[\bar{1}\bar{1}1]$ direction.

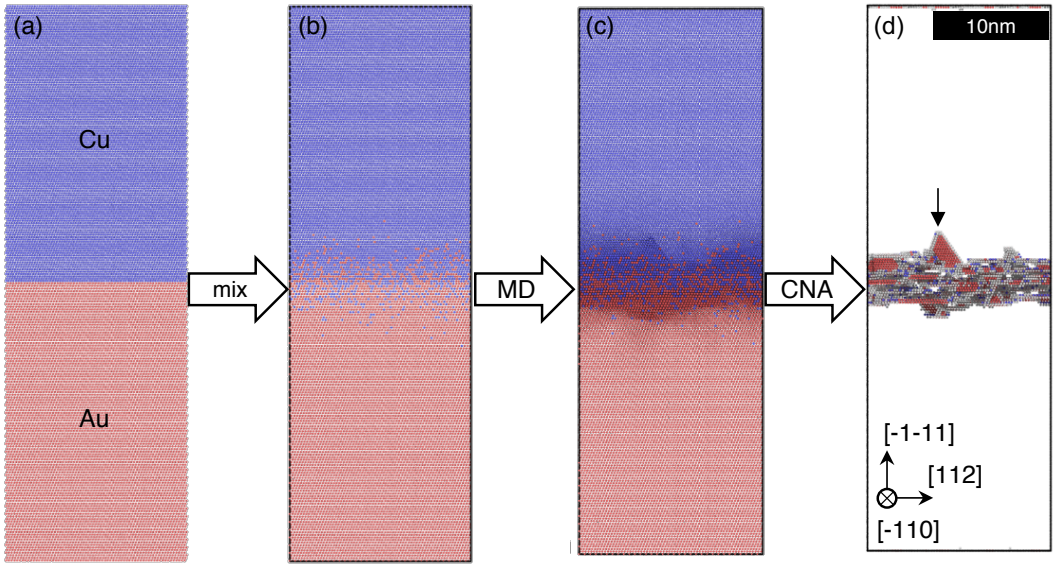

Figure 7.1: Illustration of the simulation procedure. Starting with (a) an initial perfect Cu|Au system composed of two single crystals and then (b) intermix the interface region by randomly swapping atoms to achieve the concentration profile given by Eq. (7.1). (c) This system then annealed and and aged. (d) Then a common neighbor analysis (CNA) is used to identify atoms not in their ideal face-centered cubic (FCC) environment. Atoms are colored according to their chemical element in figures (a-c) with Cu in blue and Au in red. Atoms in (d) are colored according to their local lattice structure with hexagonal close packed (HCP) atoms in red, body-centered cubic (BCC) atoms in blue and structures unidentified by the CNA in white.

In order to minimize the stresses arising from the large lattice mismatch ($\delta \approx 12\%$) between the Cu and Au crystals, the lateral cell size needed to be commensurate with the lattice constant of both Cu and Au. $n_{\mathrm{Au}} = 33$ and $m_{\mathrm{Cu}} = 37$ were used resulting in a residual mismatch of $\Delta\varepsilon = 0.08\%$ while keeping the overall size small enough for the simulation methods. The total number of atoms in the simulation cell was $\sim 10^6$.

The intermixing process that occurs between the Cu and Au crystal involves processes at a timescale not readily accessible by molecular dynamics methods, such as interdiffusion of Cu and Au atoms at the interface during the deposition process. In order to mimic this process, the interface between Cu and Au layers was manually intermixed by randomly flipping Cu and Au atoms over the interface to arrive at a specific concentration profile $c_w(z)$. The coordinate z here denotes the distance from the ideal interface and w is a measure for the initial width of the interface. The functional form of $c_w(z)$ was obtained by solving Fick's diffusion equations for interdiffusion in two semi-infinite bodies,

$$c_w(z) = \frac{1}{2} + \frac{1}{2}\,\mathrm{erf}\left(\frac{x}{w}\right). \tag{7.1}$$

The final atomic system with such a manually intermixed layer is shown in Fig. 7.1(b).

After artificially intermixing the two crystals, the system was annealed at 1000 K for a total of 2 ns in molecular dynamics (MD) and then quenched it down to 300K at a rate of $350\,\mathrm{K.ns^{-1}}$. This was followed by further aging the system at 300 K for 1 ns. The resulting atomic configuration is shown in Fig. 7.1(c). During these MD simulations, the temperature was controlled using a Langevin thermostat with a relaxation time of 1 ps. An anisotropic Berendsen barostat (Berendsen et al., 1984) with a relaxation time of ~ 5 ps was used to maintain zero stress along the $[112]$ and $[110]$ directions. All calculation steps were performed with a timestep of 5 fs.

Then the adaptive common neighbors analysis (CNA) (Honeycutt and Andersen, 1987, Stukowski, 2010) was used to identify and isolate defects in the crystal. The result of this analysis is exemplarily shown in Fig. 7.1(d), where all atoms except for those being in an ideal face-centered cubic (FCC) structure are shown. This analysis characterize the resulting interface with respect to the defects formed at or near it.

Finally, simple shear deformation was applied on four samples with different intermixing distances $w = 0, 1, 2, 4$ nm. In this case a smaller periodic simulation cell was used, with a layer thickness of 5 nm and $n_{\mathrm{Au}} = 33$ and $m_{\mathrm{Cu}} = 37$. The same annealing sequence as previously described was used to relax the systems. Direct deformation was performed at a temperature of 300 K. A strain rate of $10^8\,\mathrm{s^{-1}}$ was used in all cases. Simple shear strain was applied along $[112]\,\left(\bar{1}\bar{1}1\right)$ directions for shear parallel to the multilayer interfaces.

7.3 Results

Fig. 7.2(a) shows the fraction of atoms that are not FCC in slices of constant thickness parallel to the $(\bar{1}\bar{1}1)$ plane. This quantity is referred to as the defect concentration in what

follows. While there are slight fluctuations with position, the defect concentration appears rather homogeneous throughout the volume even though the initial atomic concentration had a gradient. Clearly, the width of the interface grows with increasing intermixing width w.

Fig. 7.2(b) shows the interface width as a function of the initial intermixing width w. The interface width is defined as the distance between topmost and bottommost hexagonal close packed (HCP) atom perpendicular to the interface plane. The figure shows that the defect zone grows monotonously with increasing intermixing parameter w. For $w < 4$ nm the interface width is roughly $w/2$, while for $w > 4$ nm a larger fraction of the intermixed region develops stacking faults. The maximum width of the defected region along the $[\bar{1}\bar{1}1]$ axis is about 7 nm when the intermixing width of the two crystal is $w = 10$ nm, the maximum value investigated here.

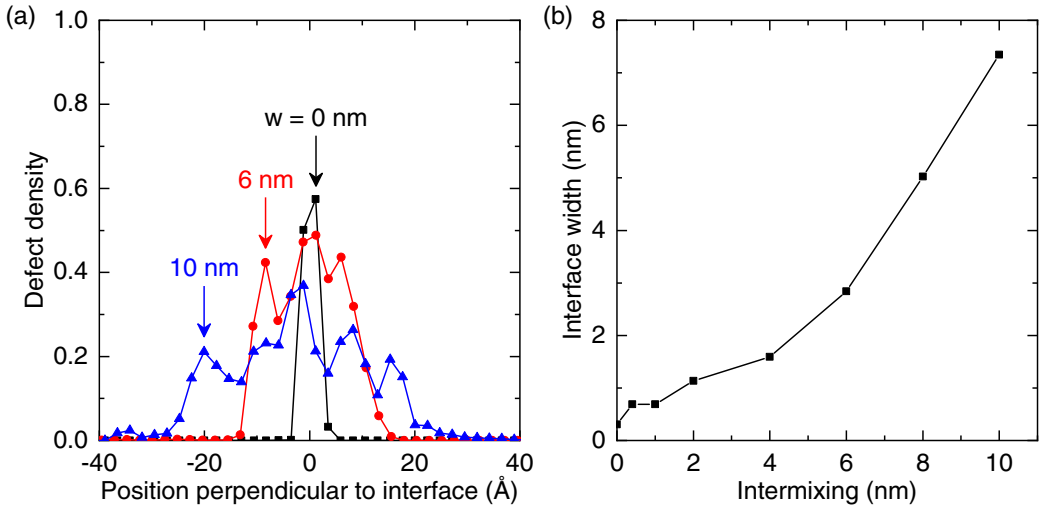

Figure 7.2: (a) Defect density, the fraction of atoms not in an FCC environment in slices parallel to the heterointerface, as a function of distance from the initial interface. (b) Interface width, measured as the distance between top- and bottommost HCP atom perpendicular to the heterointerface, as a function of the width of the initial intermixed layer w.

Figure 7.3 shows a series of views onto the interfacial plane. Shown are defects, i.e. all atoms except for those locally in an FCC neighborhood, in the interfacial atomic region ± 0.5 nm around the initial interface. The sequence of panels (a) to (h) represents the structure of the interface for intermixing parameters from $w = 0$ nm to $w = 10$ nm. Figure 7.3(a) ($w = 0$ nm) shows a perfect triangular network of HCP atoms. These are stacking faults that are bounded by Shockley partial dislocations. This network becomes distorted at $w = 0.4$ nm (Fig. 7.3(b)). The interfacial stacking faults are at this point no longer located exactly at the initial Cu|Au interface but start spreading into the material away from the interfacial plane. The regular structure of the network becomes even more distorted for $w = 1$ nm and 2 nm (Figs. 7.3(c) and (d)). At $w = 4$ nm (Fig. 7.3(e)) the regular pattern is no longer visible. The stacking faults follow a seemingly random pattern. At larger intermixing parameters, $w = 6$ nm, 8 nm

and 10 nm (Figs. 7.3(f), (g) and (h)) the interface is covered by large continuous patches of stacking faults with geometries reminiscent of slit islands (Mandelbrot, 1983). A side view of the defects at $w = 10$ nm, the largest intermixing width, is shown in Fig. 7.1(d). Figure 7.1(d) directly illustrates that stacking faults do form not only on the $(\bar{1}\bar{1}1)$ plane perpendicular to the heterointerface but spread into the bulk of the material on the three other $\{111\}$ planes. The triangular stacking fault indicated by an arrow in this figure is one side of a stacking fault tetrahedron.

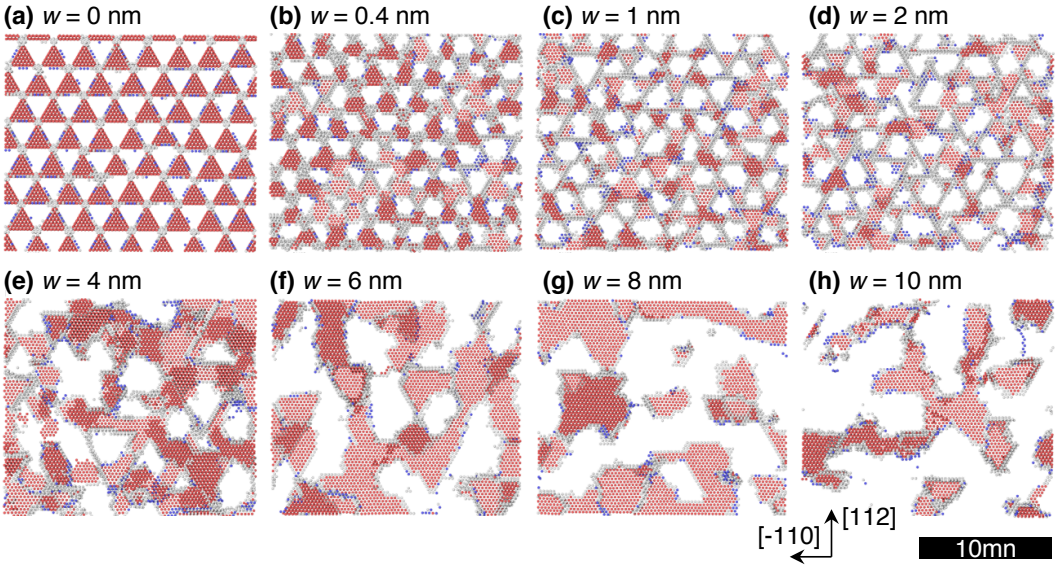

Figure 7.3: Atoms not in an FCC environment within a central slice of 1 nm thickness for intermixing width w of (a) 0 nm, (b) 0.4 nm, (c) 1 nm, (d) 2 nm, (e) 4 nm, (f) 6 nm, (g) 8 nm and (h) 10 nm. Atoms are color coded according to their local lattice structure with HCP atoms in red, BCC atoms in blue and structures not identified in the common neighbor analysis in white.

The interface structure is now characterized using two statistical measures. First, the two-dimensional structure factor of all HCP atoms in a region ± 0.25 nm around the initial interface. The structure factor is given by

$$S(q_x, q_y) \propto \sum_{i,j} f_i f_j e^{i\vec{q}\cdot(\vec{r}_i - \vec{r}_j)} \tag{7.2}$$

where $\vec{q} = (q_x, q_y, 0)$ is the wavevector inside the interface plane, $\vec{r}_i$ is the position of atom i and the sum runs over all atoms in the system. The form factor f_i is unity for HCP atoms and zero otherwise. The two-dimensional map of $S(q_x, q_y)$ is shown in Fig. 7.4 for $w = 0$ nm (panel a) and $w = 10$ nm (panel b). Both figures show the underlying symmetry of the (111) plane with respective peaks at $2\pi/a_0$, where a_0 is the lattice constant. The ideal interface (Fig. 7.4(a)) shows individual peaks with a spacing of $\Delta q \sim 3$ nm^{-1} corresponding to ~ 2 nm

wavelength. This structure is no longer visible for the disordered interface with $w = 10$ nm (Fig. 7.4b).

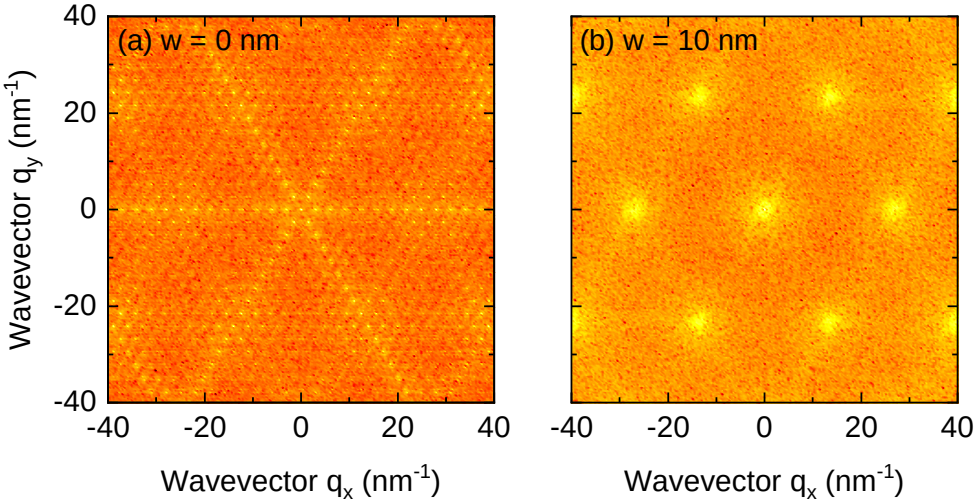

Figure 7.4: Two-dimensional structure factor of HCP atoms in a 0.5 nm slice around the heterointerface for (a) intermixing width $w = 0$ nm and (b) $w = 10$ nm.

The conjugate measure to the structure factor is the radial distribution function (RDF),

$$g_2(r) \propto \sum_{ij} f_i f_j \delta \left(r - \sqrt{(x_i - x_j)^2 + (y_i - y_j)^2} \right), \tag{7.3}$$

where x_i and y_i are the x- and y-positions of atom i, respectively. The xy-plane is the plane of the heterointerface. Fig. 7.5 shows the RDF for four interface width. The sharp interface (Fig. 7.5(a)) shows pronounced oscillations with a first minimum as ~ 1.5 nm. As the interface width increases, the period of oscillation increases and for $w = 10$ nm, the first minimum has moved to ~ 3 nm.

The mechanical response is now examined. For this matter smaller bilayer systems with a layer thickness of 5 nm are used. Simple shear deformation parallel to the heterointerface are carried out to evaluate the influence of difference intermixing width and annealing. Here an annealed system refers to a system having been through the 1000 K annealing procedure describe in section 7.2, while a non annealed system refers to a system that has simply been relaxed at 300 K. The defects were less present in the layers volume for the non annealed systems compare with the annealed systems for the same initial intermixing width. Figure 7.6 shows the stress strain curves obtained for the atomically sharp interface and three intermixing width ($w = 1, 2.5, 5nm$) for both non annealed and 1000 K annealed systems. Figure 7.6(a) reveals that atomically flat interface without annealing has a interface shear strength of a few MPa. The three intermixed systems show relatively similar response to the applied strain with a yield stress of 0.3 to 0.4 GPa and an averaged flow stress of 0.3 GPa.

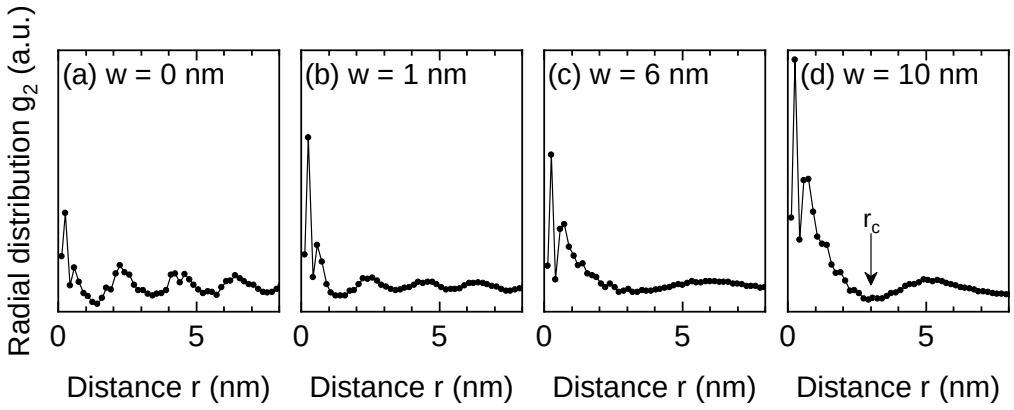

Figure 7.5: Two-dimensional radial distribution function of HCP atoms in a 0.5 nm slice around the heterointerface for intermixing with of (a) $w = 0$ nm, (b) 1 nm, (c) 6 nm and (d) 10 nm.

The data for the annealed systems in Fig. 7.6(b) are more scattered. The yield stresses vary from 0.45 to 0.25 GPa with the intermixing width going from 0 to 5 nm. The average flow stress is still oscillating around 0.3 GPa for the annealed system with a intermixing width $w = 0, 1, 2.5$ nm. The annealed system with an intermixed width of 5 nm shows a slightly lower average flow stress value of approximately 0.25 GPa.

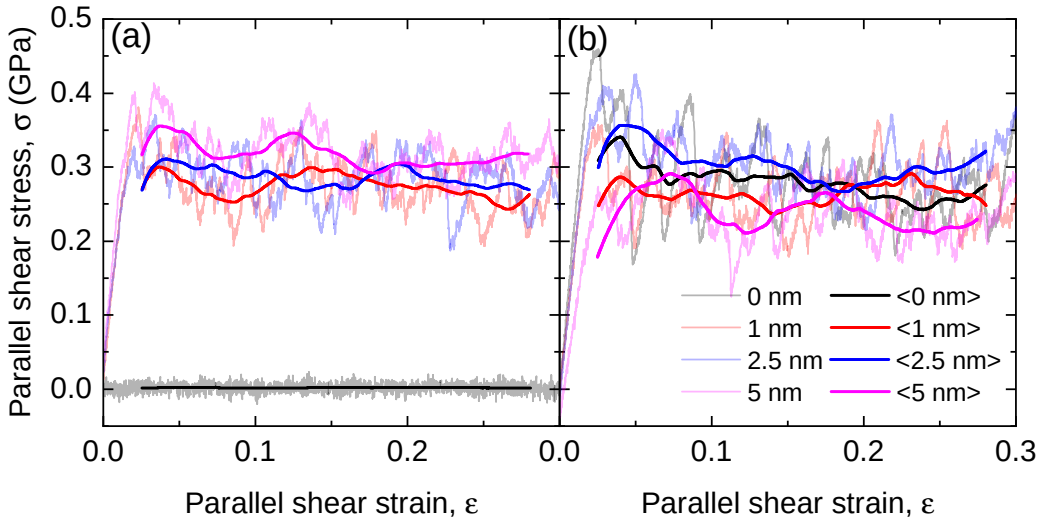

Figure 7.6: Stress-strain curves during simple shear at 300K parallel to the heterointerface of the Cu|Au multilayer system with a layer thickness of 5 nm and intermixing width $w = 0, 1, 2.5, 5$ nm (a) without annealing and (b) after annealing at 1000 K. Thick lines are a moving averages over a strain interval ± 0.025 around the respective data point, thin lines show the full data.

7.4 Discussion

The perfectly sharp Cu|Au interface shown in Fig. 7.3(a) is a realization of a semi-coherent interface, such as those found between immiscible compounds such as Cu|Ni. (Shao et al., 2013) The structure factor (Fig. 7.4(a)) and RDF (Fig. 7.5(a)) both show the periodicity of the triangular lattice of stacking faults. The first minimum in the RDF characterizes the typical spacing between the triangles.

The semi-coherent character of the interface is lost as it become more disordered by intermixing. The primary defect at the interface is still the stacking fault, but the fault is no longer located at exactly the midplane between the two phases. The triangular structure of the stacking fault lattice is also lost at larger intermixing width. Fig. 7.1(d) illustrates that the majority of these faults are located on the interfacial $(\bar{1}\bar{1}1)$ plane, but that at larger width w the interfaces has a tendency to form stacking fault tetrahedra. Since these tetrahedra are sessile, they are often responsible for hardening, embrittlement or plastic instabilities. (Martínez and Uberuaga, 2015)

The spacing of faulted and ideal crystalline regions can be estimated from the RDFs presented in Fig. 7.5. The minimum of the RDF corresponds to the distance from an HCP atom where the likelihood of finding another HCP atom is minimal. For the semi-coherent interface (Fig. 7.5(a)), this corresponds to the size of spacing between the triangular faults. For the disordered interfaces, this gives an approximated measure of the spacing between faulted regions. At $w = 10$ nm, the distance (indicated by an arrow in Fig. 7.5(d)) is around 3 nm, about half the total interface width of 7 nm (see Fig. 7.2(b)) and about double the spacing of ~ 1.5 nm between the triangles of the sharp interface ($w = 0$ nm).

The multilayers stress response to simple shear parallel of a few MPa for the atomically sharp interface (Fig. 7.6(a)) is a clear sign that the system reacts by gliding along the heterointerface as observed for the CuAg|Ni system in chapter 5. If one focuses on the non annealed system (Fig. 7.6(a)), one can see that for any intermixing width greater than 0 nm the yield stress is approximately constant. This shows that the intermixing width has only a small impact on the yield stress and interface shear strength which means that most of the strengthening comes from the heterogeneities introduced next to the heterointerface acting as pinning point to the dislocation network. Experimental results of Cu|Au nanopillar compression with a tilted interface in relation to the compression axis (Schwaiger, 2015) gave a value for interface shear strength approximately equal to 0.3 GPa. The averaged flow stress obtained here (Fig. 7.6) for any disturbed interfaces is in good agreement with the experiments.

As is was just shown a small disturbance next to the interface greatly impact the stress-strain response of the system. In Fig. 7.6(b) the originally sharp interface annealed at 1000 K has a yield stress orders of magnitude greater than its non annealed counter part (Fig. 7.6(a)). This means that even a short annealing at 1000 K is enough to disturb the heterointerfaces by atomic interdiffusion. After annealing the defect density out of the heterointerface plane increases (Fig. 7.2(a)) which lead to a greater number of dislocation nucleation points. As a result the the yield stress decreases with intermixing width (Fig. 7.6(b)) but a large flow stress value is still observed, indicating that dislocations are still hindered by the heterogeneity of the system.

7.5 Summary

This chapter shows that as a diffusive intermixed region develops at the heterointerface in the miscible Cu|Au system, the interface develops from an ordered two-dimensional network of triangular stacking faults to a three-dimensional network spreading in both crystals. This transformation increases the spacing of dislocations at the interface and gives rise to dislocation self-organization into stacking fault tetrahedra. These changes in interface structure will have an influence on dislocations interacting with the interface and therefore the mechanical property of Cu|Au multilayers.

The mechanical tests have shown that the smallest perturbation at the atomic scale at the heterointerface leads to an increase of the interface shear strength as those perturbation act as pinning point of the dislocation network. The observed value of 0.3 GPa using the EAM potential fitted in chapter 6 is in good agreement with experimentally measured interface shear strength (Schwaiger, 2015). This provides a supplementary validation point to the EAM potential developed in this thesis.

8. Scratching the surface with nanoscale tips

8.1 Introduction

Multilayers are interesting because deformation can be quantified in experiments by looking at the layer structure post-mortem. This works because the initial structure, parallel straight layers, is known and the different materials can have good contrast in microscopy.

In this chapter the evolution of the Cu|Au interfaces under tribological load is investigated at the nanoscale. Significant plastic deformation takes place when indenting or scratching a surface. Indeed, plastic deformation is responsible for part of the material loss during abrasive (Khruschov, 1974, Mishra and Szlufarska, 2012, Mishra et al., 2012) and sliding (Rigney and Hirth, 1979) wear and the plowing motion of asperities on the counter body contribute to the friction between two materials (Rigney and Hirth, 1979) . It is therefore interesting to study how multilayers behave under such conditions.

Recently, Luo et al. (2015) and Pouryazdan et al. (2017) have experimentally shown that multilayers intermix during sliding. Luo et al. (2015) have observed an interesting interface roughening mechanism under tribological loading at the nanoscale. This mechanism eventually leads to intermixing and formation of vortices at the interfaces between the Cu and Au layers as seen in Fig. 8.1. The average layer thickness in the system was 100 nm, with layers deposited by physical vapor deposition. This method creates, as described in chapter 4, a columnar polycrystal structure. Pouryazdan et al. (2017) have observed similar vortex formation for the Cu|Al multilayer system. The system was here build out of a stack of 25 μm thick layers. This technique leads to a random polycrystalline structure, and allows the formation of oxides at the interfaces. This system have a smaller lattice misfit but Cu and Al, similarly to the Cu-Au binary system, are fully miscible and form some stable binary alloys. They have observed the vortex formation at the micrometer scale under high-pressure torsion deformations. The process leading to the formation of vortices shown in Fig. 8.1 is still unclear and debated (Kim et al., 2009, Rigney and Karthikeyan, 2010, Luo et al., 2015, Pouryazdan et al., 2017).

MD work by Kim et al. (2009) and Rigney and Karthikeyan (2010) using Lennard-Jones potential to describe the atomic interactions showed vortex forming at the sliding contact between two crystalline bodies. The vortex formation in these calculations leads to local intermixing, and was attributed to Kelvin-Helmholtz-like instabilities in fluids. Kelvin-Helmholtz instabilities are known from fluid dynamics in the turbulent regime, i.e. large Reynolds number (Thorpe, 1971). These instabilities are responsible, for example, for vortex formation in clouds. Pouryazdan et al. (2017) pointed out that the velocities required to be in a turbulent regime at the contact of two metallic crystals are unrealistic (hundreds of km s^{-1}). The Kelvin-Helmholtz instabilities are therefore unlikely to occur in such multilayers. Instead, Pouryazdan et al. (2017) proposed a fluid-mechanics model involving solely viscosity contrast between the constituents of a multilayer stack at the microscale. While this model does not require unrealistic flow velocities, it requires strain values going up to 400. These extremely high applied shear strains are easily achievable using high-pressure torsion as the shear strain scales linearly with the sample diameter and the number of revolutions. This is a plausible explanation for micro- and macroscale to explain vortex formation and layer folding in multilayered materials. However, these strain values are much larger than the one achieved under the sliding track. At the nanoscale other deformation mechanisms have been observed involving dislocations, such as shear banding (Li et al., 2010), which could trigger such vortex formation.

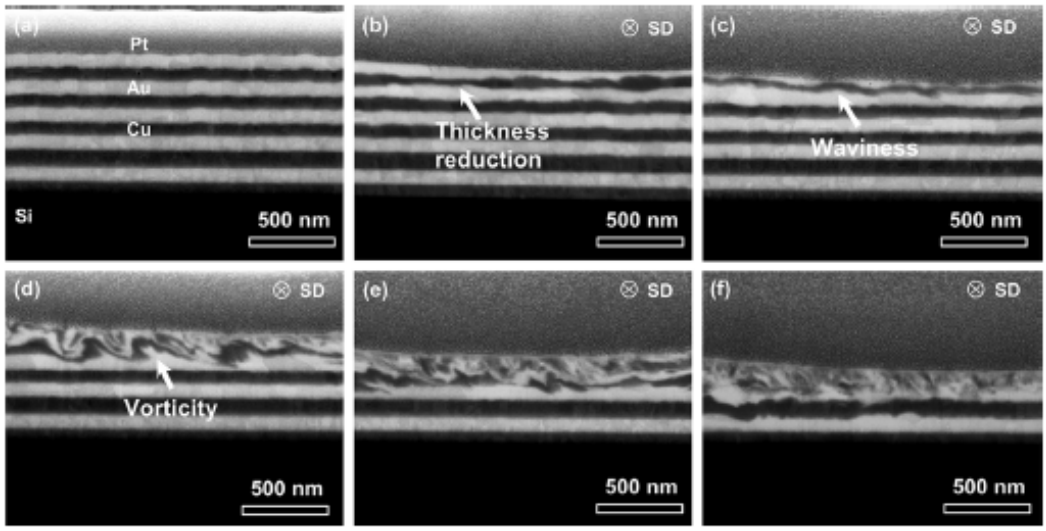

Figure 8.1: SEM picture of the CuAu system before (left) and after (right) cyclic sliding showing evidence of layer mixing with vortices formation. Figure 1 from Luo et al. (2015).

This chapter aims at reproducing these vortex structures in large scale molecular dynamics (MD) simulations to gain insights into their formation mechanism. The system consist of a replica of the experimental system in Fig. 8.1. This allows to investigate the importance of the heterogeneity of the stress field coming from the spherical indenter. Even though this

system presents a realistic geometry, the correct (experimental) ratio between indenter radius and layer thickness is not reachable in MD.

8.2 Methods

Figure 8.2 shows the atomistic system used here. It is comprised of a stack of 8 Cu and Au layers of 5 nm thickness each with Au facing top. A few rows of atoms at the bottom were kept fixed to anchor the atomistic model in space. The two bottom layers of the system were thermostatted at 300 K using a using a Langevin thermostat with a damping constant of 10 ps. The layers were stacked along the $[\bar{1}\bar{1}1]$ direction. Similarly to the method employed in chapter 7 the interface between Cu and Au layers were manually intermixed by randomly flipping Cu and Au atoms over the interface to arrive to a specific concentration profile over a total width of 2.5 nm across the interfaces. Periodic boundary conditions were applied along the $[112]$ and $[\bar{1}10]$ directions. The EAM potential developed in chapter 6 was employed to model the interactions in the multilayer slab. Table 8.1 gives the exact dimensions of the multilayer system.

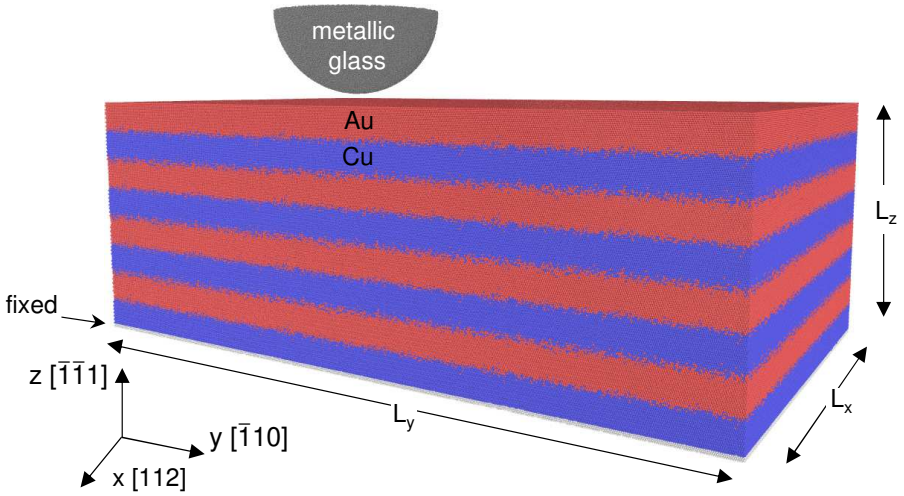

Figure 8.2: Illustration of the atomistic setup for the nano-scratch MD calculations. Atoms are color coded according to their type and mobility with mobile Au atoms in red and mobile Cu in blue, fixed Cu atoms are in white and indenter atoms in gray.

A rigid spherical indenter of 30 nm in diameter was used. This diameter is typical for atomic-force microscopy (AFM) type experiments that are often regarded as a model for a single asperity on a rough surface (Szlufarska et al., 2008). The indenter was obtained by freezing the structure of a $Cu_{0.50}Zr_{0.50}$ metallic glass obtained by melting a random solid solution of $Cu_{0.50}Zr_{0.50}$ at 2500 K and then quenching it down to 0 K at a rate of 6 K/ps. A purely repulsive with $r_{cut} = 2^{\frac{1}{6}}\sigma$ Lennard-Jones potential acted between atoms in the multilayer slab

Table 8.1: Dimensions of the Cu|Au multilayer system used in the sliding contact calculations.

	x, $[112]$	y, $\left[\bar{1}10\right]$
n_{Au}	130	438
m_{Cu}	145	390
Size (nm)	65	113

and the indenter. The interaction parameters with Cu and Au are $\varepsilon_{Cu} = 0.4093$, $\sigma_{Cu} = 2.338$, $\varepsilon_{Au} = 0.4251$, $\sigma_{Au} = 2.485$ (Halicioğlu and Pound, 1975). Compared with a perfectly smooth mathematical representation of a hemisphere, the amorphous structure introduced finite friction between indenter and metallic surface (Luan and Robbins, 2005, Klemenz et al., 2018). This model was chosen because most real-world tip will exhibit some sort of surface disorder: The most common material for AFM tips is Silicon which typically has an amorphous silica at its surface (Jacobs et al., 2016).

The calculation was performed in two stages. The first step consists in lowering the spherical indenter along $\left[\bar{1}\bar{1}1\right]$ axis. The indenter was lowered with a downward velocity of 0.15 Å/ps until the force acting on the rigid indenter atoms reached 1000 eV/Å. Then the indenter was moved along the $\left[\bar{1}10\right]$ sliding direction over a distance of 40 nm from the indentation point. The normal force acting on the indenter was monitored and maintained at the control value of 1000 eV/Å by adjusting the indenter depth on the fly. The sliding velocity was set to 0.5 Å/ps and instantly reversed upon reaching the dead centers. A maximum of 5 reciprocating passes was performed.

8.3 Results

The initial structure (Fig. 8.2) of the simulation setup is a stack of perfectly flat Cu|Au multilayers terminated with an Au layer on top. The only defects present are introduced by the intermixed regions at the heterointerfaces. The different panels in Fig. 8.3 show a sliced view of the system parallel to the sliding direction at the different calculation stages. Figure 8.3(b) shows the final configuration after indentation with a normal load of 1000 eV/Å. The indenter sinks into the soft terminating Au layer, but does not sink all the way to the next Cu layer.

Starting from the configuration shown in Fig. 8.3(b) the indenter is moved at constant velocity of 0.5 Å/ps in a reciprocating motion. During the whole motion the external force on the indenter is held constant. The true force experienced by the indenter also includes a component from the inertia of the tip and fluctuates slightly around this value. Figure 8.4(a)

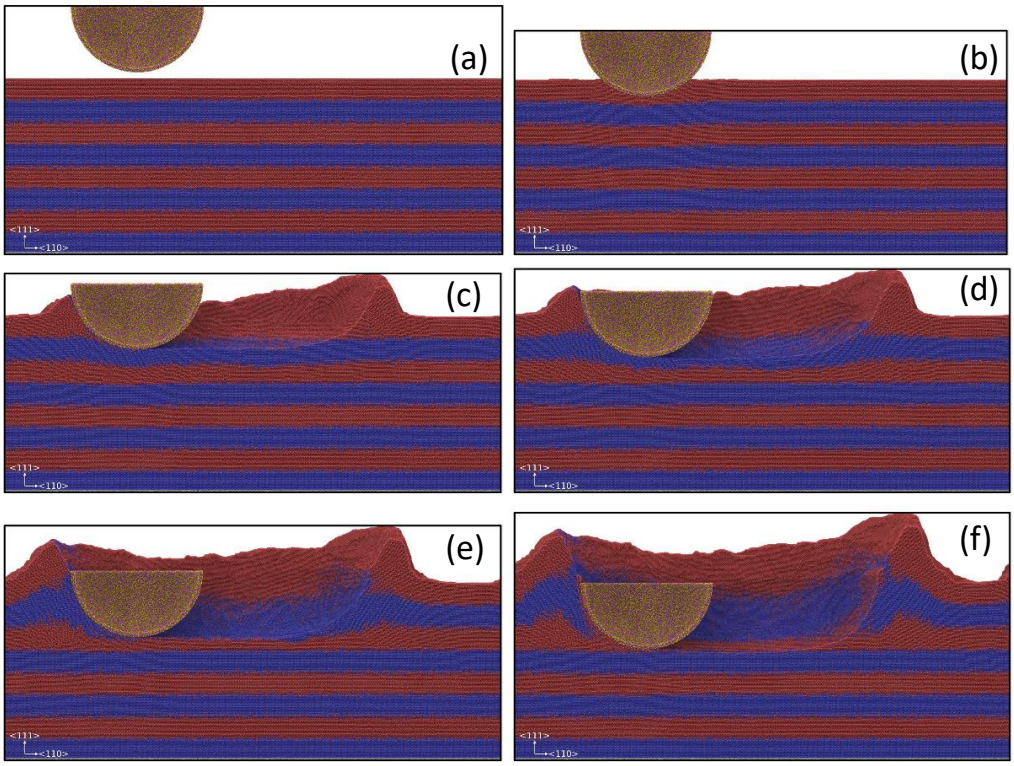

Figure 8.3: Snapshots of the reciprocating sliding contact simulation at a normal force of 1000 eV/Å. Each panel shows a 3D view of the system sliced parallel to the sliding direction for clarity. Panel (a) shows the initial simulation setup, (b) the final stage of the indentation at 1000 eV/Å, and panels (c-f) show the final snapshot after cycles 1 to 4, respectively. Cu atoms are in shown blue and Au atoms are in shown in red.

shows that the fluctuation is on the order of ± 23 eV/Å. The lateral force required to move the indenter is shown in Fig. 8.4(b). At every inversion of the direction of movement, the force jumps to a value of approximately 250 eV/Å over a distance of 10 nm. The force then rises roughly linearly with sliding distance. In the later strokes the force rises again sharply towards the end of the wear track.

The progression in geometry after each subsequent sliding cycles is shown in Fig. 8.3(c-f). The indenter progressively sinks into the substrate, accompanied by transfer of material to the edge of the wear track where it piles up. Figure 8.3 also shows that the indenter sinks quickly into an Au layer while it requires multiple cycles to break through the harder Cu layer. Note that in Fig. 8.3(d) both the terminating Cu and the Au layer underneath have thinned.

In addition to thinning of the softer Au layer, the interface between Au and Cu roughens. This is particularly evident in Figs. 8.3(c-e) for the interface just below the sliding indenter.

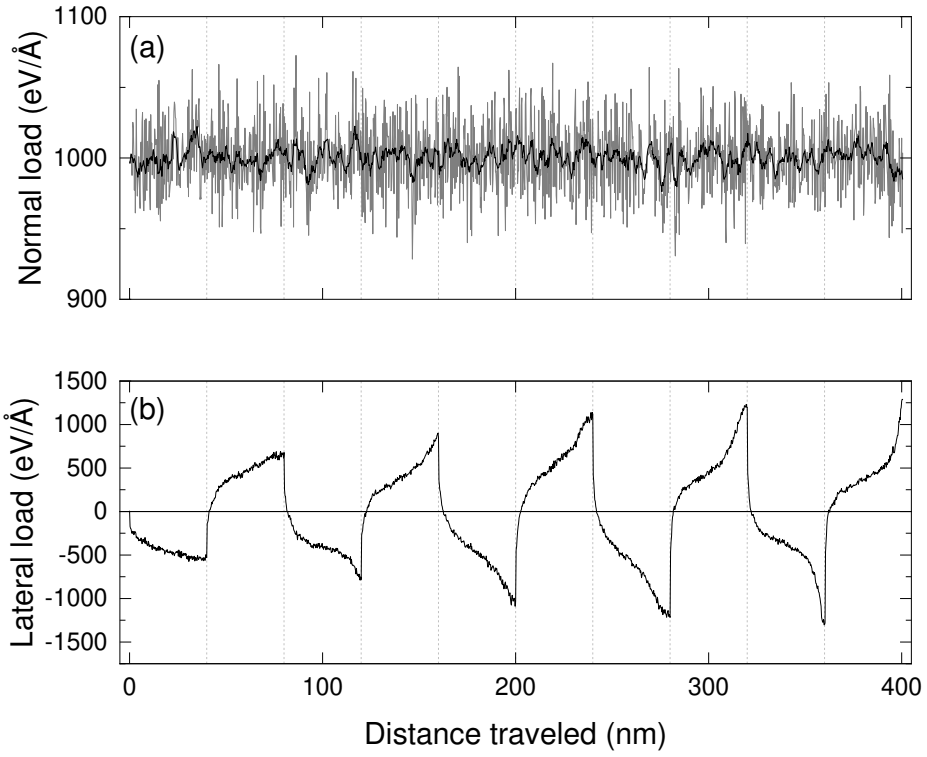

Figure 8.4: Normal (a) and lateral (b) load on the indenter over the sliding cycles. The black line shows the floating overage of the normal load over a period of 50 ps (black). The average normal load is $F_N = 1000 \pm 23$ eV/Å.

Roughening extends to regions outside the wear track just under the pileup that have not yet been reached by the indenter.

Figure 8.5 shows details of where the strain is accumulated during the first stroke. Panels (a)-(c) display just atoms that have accumulated more that 20% of atomic strain. During indentation, most strain is localized within the topmost Au layer with the exception of a small region just underneath the tip apex, where dislocations have passed into the underlying Cu layer. The corresponding common neighbor analysis of this snapshot (Fig. 8.5(d)) clearly shows stacking faults in the Cu layer in that region and within the Au layer. The top view of the deformation during indentation reflects the threefold symmetry of the $\{111\}$ slip planes outside of the main indenter depression. Dislocations nucleate underneath the indenter and then escape on the respective slip planes; this shields some regions from accumulating strain.

The strain accumulated in the first layer and the corresponding density of defects increase after the first stroke (Figs. 8.5(b-c)). Interestingly, damage in the lower-lying Cu layer (and the next Au layer) can only be seen at the point of indentation and the end of the wear track.

After the first cycle, deformation and defect structure has extended from the topmost Au layer to the next Cu and the subsequent Au layer (Figs. 8.5(e-f)). Figure 8.3(c) shows that the indenter has at this point already penetrated the harder Cu layer; the soft Au underneath then immediately accommodates some of the deformation introduced into the layer.

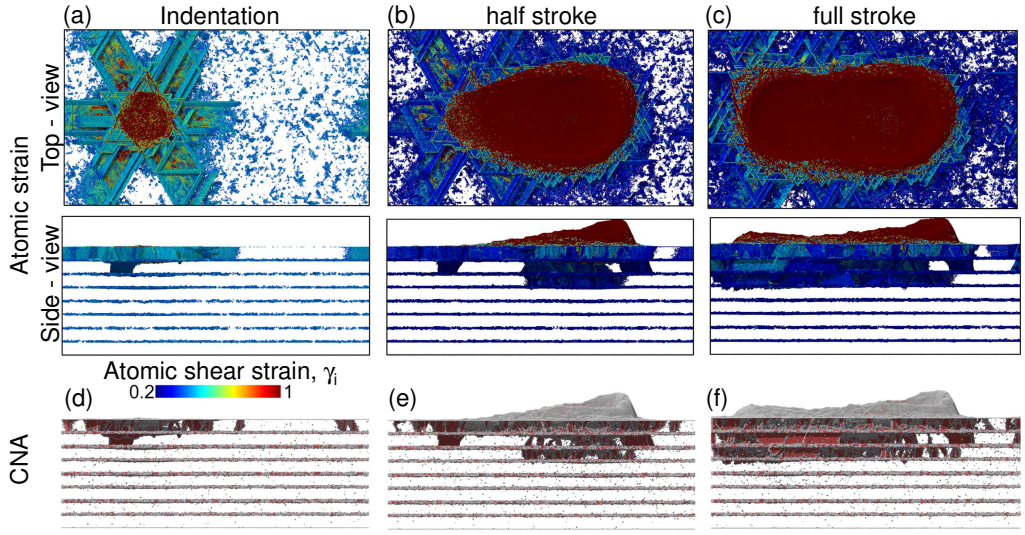

Figure 8.5: Reciprocating sliding simulation snapshots with a force of 1000 eV/Å after (a,d) indentation, (b,e) half a stroke and (c,f) one full stoke. Atoms in panels (a)-(c) are colored after their local atomic shear strain values. Atoms with a atomic shear strain value lower than 0.2 are removed for clarity. The atomic strains are computed taking for reference the relaxed undeformed state of the system. Panels (d)-(f) shows the corresponding common neighbor analysis (CNA). Atoms in red are in an HCP local environment, atoms in blue are in a BCC local environment, atoms in white are in an undefined local environment. In the CNA snapshots, all the FCC atoms have been removed for clarity.

8.4 Discussion

During the initial indentation (Fig 8.3(a)) the indenter does not cross entirely the first Au layer. This can be related to Fig. 8.5(a) showing a significant density of stacking faults right underneath the indenter and pilling up against the first Cu-Au interface. As expected by the various models exposed in section 1.2, at such a small scale the interface plays a critical role blocking dislocations and thus responsible for the hardening of the single crystal Au layer.

The lateral force increase observed in Fig. 8.4(b) can be rationalize by the indenter hitting material piling up in front of the indenter. This material is then pushed against the pileups of the previous strokes at the edge of the wear track where the material has significantly hardened. The range of forces seen during the first two strokes corresponds to a friction coefficient of 0.25 to 0.75 which are typical values for dry contact sliding of metals (Bhushan,

2002). The sharp rise in friction force towards the end of a stroke can be explained by a similar pileups mechanism, i.e. the indenter pushes against more and more piled-up material. The fold just outside the wear track in Fig. 8.3(f) appears to nucleate from a pronounced interface roughness in the previous cycles. Similar folds are often observed on machined surfaces, their explanation in the case of machining is a heterogeneity in material properties, such as elastic modulus (Sundaram et al., 2012) or grain orientation (Beckmann et al., 2014). This would indicate that the material piled up outside of the wear track present some heterogeneity.

The difference in penetration rate in Cu and Au is consistent with common measures of hardness for Au and Cu films where Cu is measured as being the harder of the two materials (Li et al., 2017). This increased resistance to the penetration of the indenter can also be seen in the increased resistance towards sliding. Friction forces shown in Fig. 8.4(b) are significantly higher for the strokes that plow within the Cu layer than those that displace mainly Au atoms.

8.5 Summary

This chapter has shown and discussed a set of scratching simulations of Cu|Au multilayers with indenters of sizes typically used in atomic-force microscopy (AFM). The simulation does not show the formation of vortex instabilities observed experimentally on much larger scales and for loads with much larger indenters. Most likely this is because the indenter radius is on the order of the multilayer thickness, while the experiments of Luo et al. (2015) used 100 nm thick layers and an indenter of size 16 μm, two orders of magnitude larger than the layer thickness. However, the results can in principle be directly compared to recent efforts using AFMs for indentation and scratching (Egberts and Bennewitz, 2011, Egberts et al., 2012, Caron and Bennewitz, 2015) that have not yet been applied to metallic multilayers.

9. Tribological loading of Cu|Au

9.1 Introduction

This chapter starts from the observation that reproducing the vortex formation with MD as shown in the previous chapter was not possible. The ratio between layer thickness λ and indenter radius R, λ/R, was approximately equal to 2×10^{-1} in the calculations of chapter 8 and 6×10^{-3} in the experiments of interest (Luo et al., 2015). Such a large ratio in the calculations leads to an inhomogeneous stress field underneath the indenter across the thickness of the first layer (Hamilton, 1983). For the smaller experimental ratio, the stress field can be approximated to an homogeneous stress field over the thickness of a few layers. This leads to a complete redesign of the system in this chapter where the calculations are ran considering a representative volume. This system emulates the loading conditions a representative volume of the multilayer stack would feel underneath the indenter.

Earlier work on simple shear of Cu|Au multilayers, e.g. in chapter 7, did not show any precursory signs of vortex formation. Therefore, one possible hypothesize is that some heterogeneity in the system is necessary to trigger vortex formation. As mentioned in chapter 4, FCC multilayer materials grown experimentally tend to form columnar grains with a grain size on the order of the layer thickness, i.e. in the 100 nm range in the experiments of interest (Luo et al., 2015). Zhang et al. (2017) showed that nanocrystalline surfaces are unlikely to be perfectly flat, consequently some misorientation between layers can occur during the preparation of a multilayered structure experimentally. With this simpler system this chapter aims at investigating one specific hypothesis regarding vortex

formation: what is the influence of the misalignment of the $[111]$ axis with the multilayer growth direction?

9.2 Methods

The representative volume element used in this chapter, shown in Fig. 9.1, was designed for an abstraction of the indenter itself. The simulation cell represents a volume element that would lie underneath a spherical indenter of a radius much larger than the layer thickness, similarly to the experimental setup describe by Luo et al. (2015). Implicit in the use of a representative volume element is the assumption that stress gradients are small and that the stress in the volume element can be approximated as homogeneous. To test the hypothesis on $\{111\}$ planes misorientation compared with the interfaces, the calculations were initially performed on a system having initially perfectly parallel $\{111\}$ planes with the interfaces. Then the $\{111\}$ planes were tilted around the y, $[\bar{1}10]$ axis. Because of the final size of the volume elements (linked to the lattice mismatch between Cu and Au) only a final number of tilting angles were accessible in order to keep the periodicity of the system. The initial system shown in Fig. 9.1 was composed of 10 layers of 5 nm thickness each, with an in-plane size of approximately 30×30 nm^2. A possible size effect was also investigated by running a similar calculation on a "supercell" system nine times larger (replicating the undeformed system cell in the x and z directions for $\theta = 5°$) comprised of 30 layers. Table 9.1 gives the exact number of Au and Cu unit cell used in the in-place directions and the corresponding tilting angles. Periodic boundary conditions were applied for all the simulation cell directions.

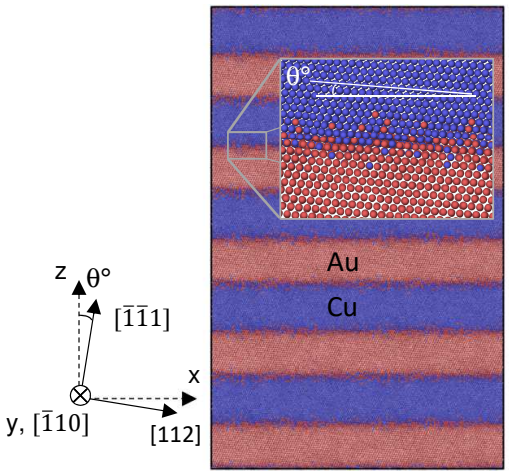

Figure 9.1: Illustration of the atomistic setup for the Cu|Au slab deformation MD calculations. Atoms are color coded according to their type with Au atoms in red and Cu in blue.

Table 9.1: Minimum simulation cell size used for the simulations. The numbers n and m denote the number of unit cells of the Au and Cu layer, respectively. A ratio $m/n \neq 1$ and different tilting angles θ are necessary to accommodate the nominal lattice mismatch and comply with the periodic boundary conditions. All systems are composed of 10 layers, except the supercell containing 30 layers.

Setup name	$\theta_{Au}/\theta_{Cu}\,(^\circ)$	$n_{[112]}/m_{[112]}$	$n_{[\bar{1}10]}/m_{[\bar{1}10]}$
0°	$0/0$	$66/74$	$125/140$
2.5°	$2.45/2.19$	$66/74$	$125/140$
5°	$4.90/4.37$	$66/74$	$125/140$
$5^\circ(supercell)$	$4.90/4.37$	$198/222$	$125/140$
10°	$10.0/8.93$	$64/72$	$125/140$

The systems were initially annealed at 1000 K and then relaxed at 300 K following the procedure described in chapter 7. The systems then underwent two successive deformation steps, the first one consisted in an equi-biaxial tensile deformation. Then the resulting system was deformed using simple shear. The deformations were carried out at 300 K with a strain rate of $10^8\,\mathrm{s}^{-1}$. The temperature was controlled using a Nosé-Hoover thermostat with a relaxation time of 1 ps applied only in the direction perpendicular to the deformation. The biaxial tensile deformation was imposed by changing the simulation box size along the x and y, $[\bar{1}10]$ directions according to the defined strain rate. The pressure perpendicular to the deformation (i.e. z direction) was kept at zero using a using the Parinello-Rahman barostat with a relaxation time constant of 10 ps. Simple shear deformation was then applied along the interface planes, i.e. along $[112](\bar{1}\bar{1}1)$ for $\theta = 0^\circ$, by homogeneously deforming the box at the prescribed strain rate.

9.3 Results

Equi-biaxial deformation. The initial systems with 10 layers and misalignment ranging from $\theta = 0^\circ$ to 10° with interfaces parallel to the xy-plane are deformed by equi-biaxial deformation along the x and y axis. Figure 9.2(a) shows the evolution of the averaged root mean square width (w^l_{RMS}) for each Cu-type and Au-type layers. The root mean square width for each type is defined as

$$w^l_{\mathrm{RMS}} = \sqrt{\frac{1}{N_l}\sum_{i\in l}\left(z_i(t) - \frac{1}{N_l}\sum_{j\in l} z_j(t)\right)^2} \tag{9.1}$$

with l a given layer in the system, N_l the total number of atom in this layer and $z_i(t)$ the z-component of atom i at time step t. Each atom is assigned to a single layer at the beginning of the calculation. This assignment stays fix during the course of the calculation. This measure allows to track down layer thinning and broadening. During the equi-biaxial deformation, w^l_{RMS} shows a similar behavior for all the systems independently of their misorientation. w^l_{RMS} linearly decreases to reach a minimum at strain value of approximately 20% before showing a small increase after 25% strain. Both Cu-type and Au-type layers are thinning down at the same rate. Figures 9.3(a,c) show the systems after equi-biaxial deformation at 25% strain. Both $\theta = 0°$ and 5° systems show clear shear bands crossing several layers which create the most pronounced roughness at the interfaces.

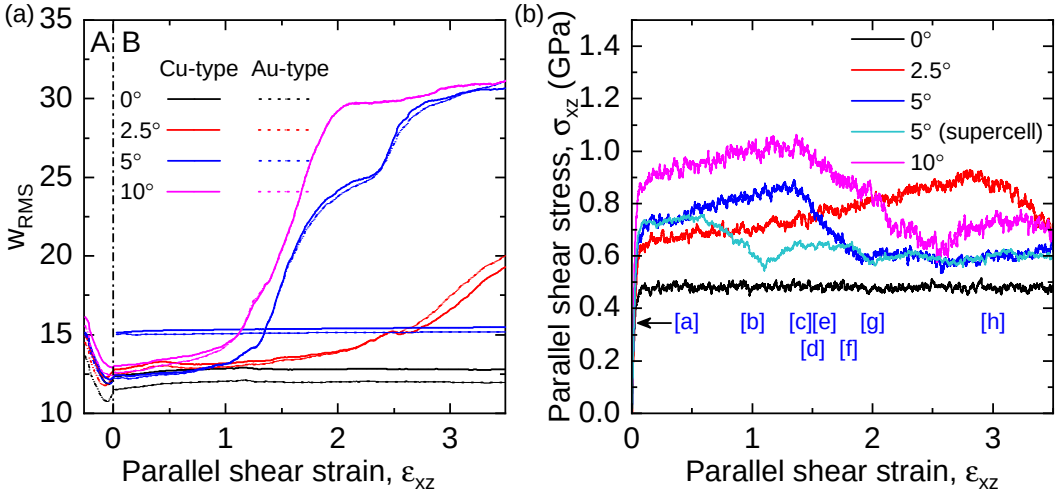

Figure 9.2: (a) Averaged root mean square of the layer width, w^l_{RMS} (Eq. (9.1)), over the course of the biaxial (subplot A) and simple shear deformation (subplot B). (b) Stress strain curve obtained during the simple shear calculation of the misoriented $\{111\}$ planes for $\theta = 0°, 2.5°, 5°, 10°$. The blue letters in square brackets indicates the strain values corresponding to the snapshots shown in Fig. 9.4 for the $\theta = 5°$ calculation.

Simple shear deformation. After the equi-biaxial deformation the systems are deformed by applying simple shear. Figure 9.2(b) shows the stress-strain curves obtained for this deformation on the four systems of interest. The system without misorientation ($\theta = 0°$) shows a stress strain curve similar to the ones shown in Fig. 7.6 for the simple shear deformation of Cu|Au bilayer parallel to the interface. The system yields at around 0.5 GPa and then enters a flow regime with a flow stress fluctuating around 0.5 GPa. The systems with a misorientation show yield stresses that increase with θ. The systems yield between 0.6 GPa for $\theta = 2.5°$ and 0.88 GPa for $\theta = 10°$. All misoriented systems then show strain hardening leading to a point where the stress lowers. The strain values at which this stress reduction occurs varies with the misorientation. It occurs at $\varepsilon \approx 2.9$ for $\theta = 2.5°$ and $\varepsilon \approx 1.3$ for $\theta = 5°$ and 10°. The shear stress eventually lowers to approximately the same value for all the misoriented systems, about 0.6 GPa. Figure 9.2(a) shows that the sudden stress

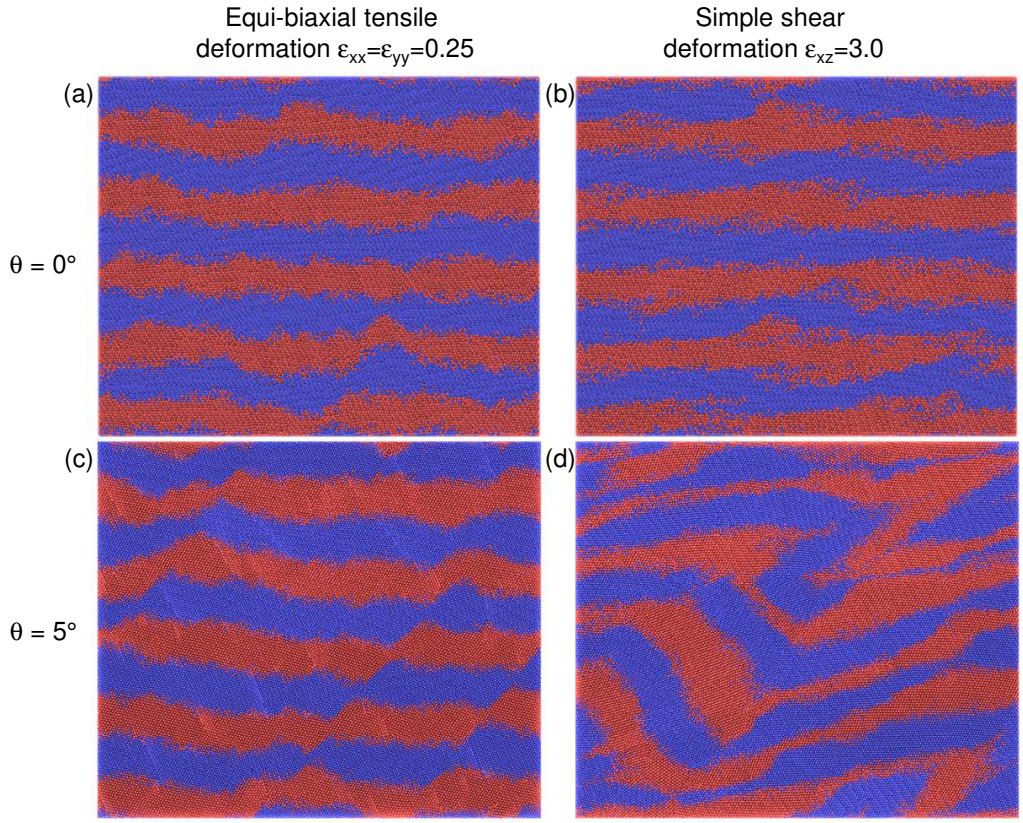

Figure 9.3: Snapshots of the multilayer stack with (a,b) aligned $\left[\bar{1}\bar{1}1\right]$ planes with the interface and (c,d) $\theta = 5^\circ$ misoriented planes. (a,c) snapshots taken after equi-biaxial deformation along the x and y axis to $\varepsilon_{xx}, \varepsilon_{yy} = 0.25$, and (b,d) after subsequent simple shear deformation to $\varepsilon_{xz} = 3.0$ (right).

decrease for the misoriented systems occurs at the same strain as the rapid increase of the averaged w^l_{RMS} values. For $\theta = 0^\circ$ the averaged w^l_{RMS} value stays relatively constant over the whole shear deformation. Figure 9.3(b,d) shows the systems obtained at shear strain value of $\varepsilon = 3.0$ for $\theta = 0^\circ$ and 5°. One can see that for $\theta = 5^\circ$, the layered structure is severely deformed with noticeable folding pattern, while for $\theta = 0^\circ$ the deformation is localized at the interfaces.

In order to better understand what happens with the misorientation, the calculations now focus on the $\theta = 5^\circ$ misoriented system. Figure 9.4 shows snapshots of the system with FCC atoms color coded according to their local lattice orientation along the z-axis. Additionally, Fig. 9.5 shows density maps of these local lattice orientations in inverse pole figures. The lattice orientation is obtained using the polyhedral template matching method (Larsen et al., 2016, Stukowski, 2010) (PTM). The orientation was determined along the z-axis (multilayer growth axis) and an equal-area projection was used to assign a color to each atom according to the color map in Fig. 9.4.

Before shear, one can see that almost all the FCC atoms are oriented in similar directions, with the $[\bar{1}\bar{1}1]$ direction along the z-axis. As the applied shear strain increases to $\varepsilon = 1.0$, some curvature is introduced on the interface planes. At shear strain value of $\varepsilon = 1.4$, i.e. right after the stress decrease, dislocations traces are seen across three layers marked by the two white arrows in Fig. 9.4(c). As the strain increases, this interlayer region widens up to a shear strain of $\varepsilon = 1.8$. The system now has a large twinned area with a $[111]$ orientation along the z-axis (in purple in Fig. 9.4). As the shear strain continues to increase and raises above $\varepsilon = 1.8$, this zone is now shrinking and assimilated back to the bulk of the system by rotating back to a similar orientation. This rotation lead to the creation of two slightly misoriented zones in the system as the green color of half of the system in Fig. 9.4 is fading away. The separation between these two zones is highlighted in Fig. 9.4 with red dashed lines. At the final shear strain value of $\varepsilon = 3.0$ one can see that there is now two distinct orientations in the system, $[\bar{1}\bar{1}1]$ (original) and $[1\bar{1}1]$ (rotated), separated by a boundary. Further analysis quantifies a misorientation of approximately 58° between the two grains. The rotation process is clearly shown in Figs. 9.5(c-h). First, there is a distribution of orientations between the $[111]$ and $[011]$ area of the standard stereographic triangle after the stress decrease (Fig. 9.5(c)), followed by the appearance of two distinct orientations in Figs. 9.5(c-g), and finally at shear strain value of $\varepsilon = 3.0$ (Fig. 9.5(h)) the rotation is complete with the atoms in the system reverting to a $[111]$ orientation along the z-axis.

A possible size effect on this rotation mechanism is investigated by running a similar calculation on a larger supercell of the system shown in Figs. 9.3- 9.5. Figure 9.6(a) shows the result obtained after equi-biaxial deformation. Similar shear bands are observed as in the smaller system. This system is then deformed using the aforementioned simple shear protocol. Figure 9.2(b) shows the stress-strain curve obtained for the supercell system. Compared with the smaller system the large system yields at the same point but does not show as much strain hardening after yielding. Instead the system enters in a flow regime until a stress decreases at a shear strain of $\varepsilon = 0.55$, the stress then reaches values similar to the one encountered for the smaller system. At larger shear strain the two systems behave similarly and the two stress-strain curves collapse onto each other. At a shear strain of $\varepsilon = 3.0$ the larger system shows similar folding patterns (Fig. 9.6(b)). The analysis of the local lattice orientation on Figs. 9.6(c-d) shows that a similar misoriented area is present at the end of the calculation.

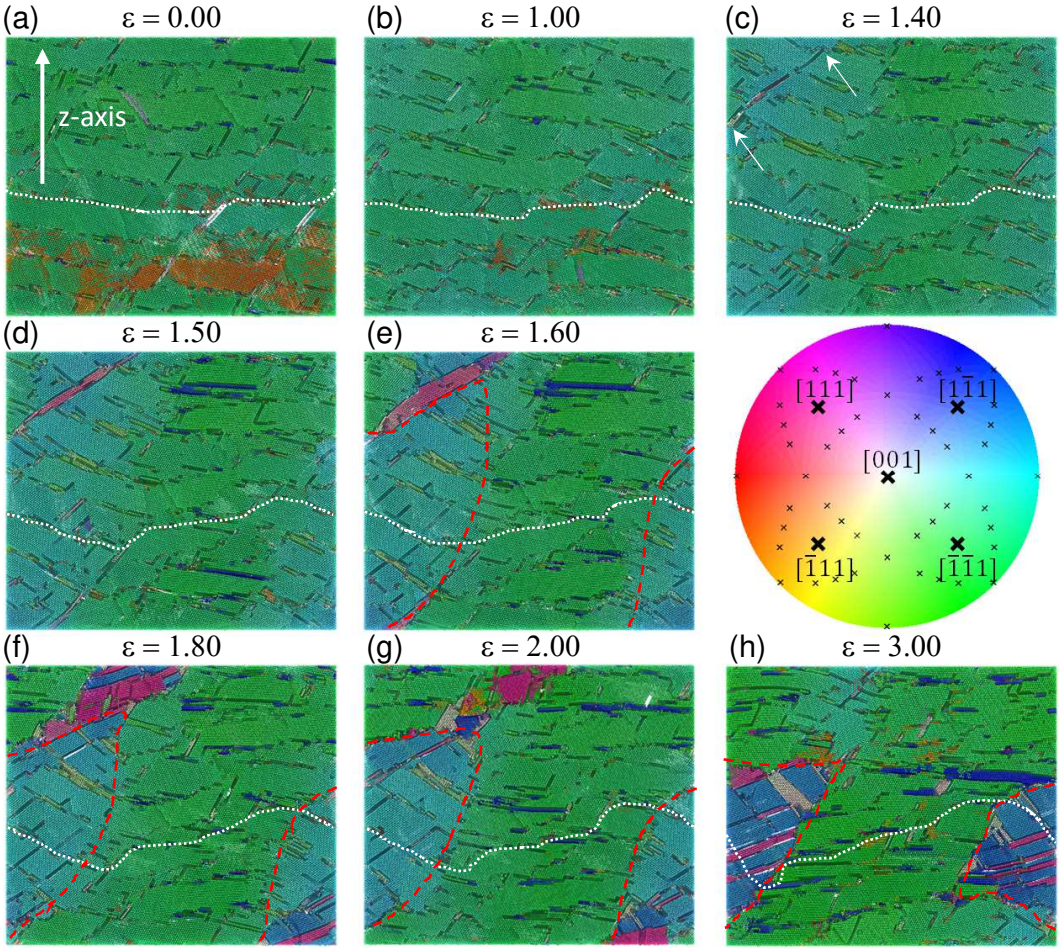

Figure 9.4: Orientation maps of the system with a misorientation of $\theta = 5°$ during simple shear deformation. Non-FCC atoms have been removed, FCC atoms are color coded after their local lattice orientations along the z-axis. The interfaces are still visible as darker contrasted atoms. For clarity one interface is marked up with a white dashed line. The arrows in (c) indicate the boundaries of the twinning event. The red dashed line highlight the separation between two misoriented zones as discussed in the text. $\{111\}$ directions are shown on the colormap, the remaining crosses on the colormap correspond to the main low index directions in cubic symmetry.

9.4 Discussion

The initial reduction of the averaged w^l_{RMS} values in Fig. 9.2(a) during the equi-biaxial tensile deformation can easily be connected to the layers co-deforming homogeneously. Even though co-deformation is here dictated by the periodic boundary conditions applied on the system, such behavior is observed experimentally under indentation for Cu|Au at the nanoscale (Li et al., 2017). The inversion of the averaged w^l_{RMS} slope in Fig. 9.2(a) corresponds to the appearance of roughness at the interfaces. Indeed during equi-biaxial tensile deformation, where layers should thin down due to mass conservation, the only way

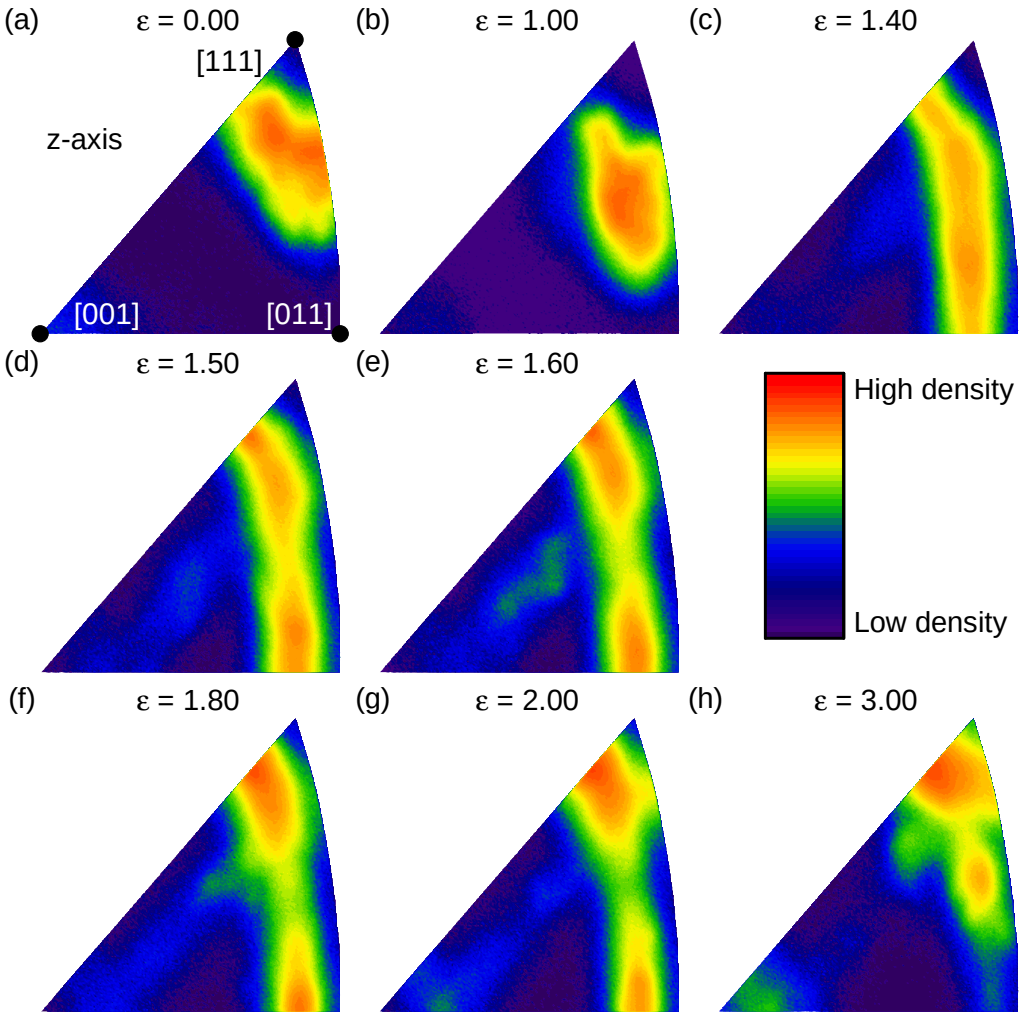

Figure 9.5: Inverse pole figures showing the local lattice orientation density along the z-axis of the simulation cell in the standard stereographic triangle. The quadrants correspond to different shear strain ε applied on the system with a misorientation of $\theta = 5°$. Each quadrant has its corresponding snapshot in Fig. 9.4. The black dots in (a) show the position of the [001], [011] and [111] poles in the standard stereographic triangle representation.

to increase the averaged w^l_{RMS} value is for the layer to shear. Such shear bands are visible in Fig. 9.3. The equi-biaxial deformation outcome seems to be independent from the $\{111\}$ misorientation. Similar shear banding have been observed in multiple multilayered system under indentation (Li et al., 2010, Yan et al., 2013b).

The first noticeable difference regarding the $\{111\}$ misorientation is the increase of yield stress with increasing misorientation θ during the simple shear deformation (parallel to the initial interface plane, xy) in Fig. 9.2(b). These higher values translate into an increase of the interfacial shear strength. Indeed, in order to accommodate for misorientation, steps must be

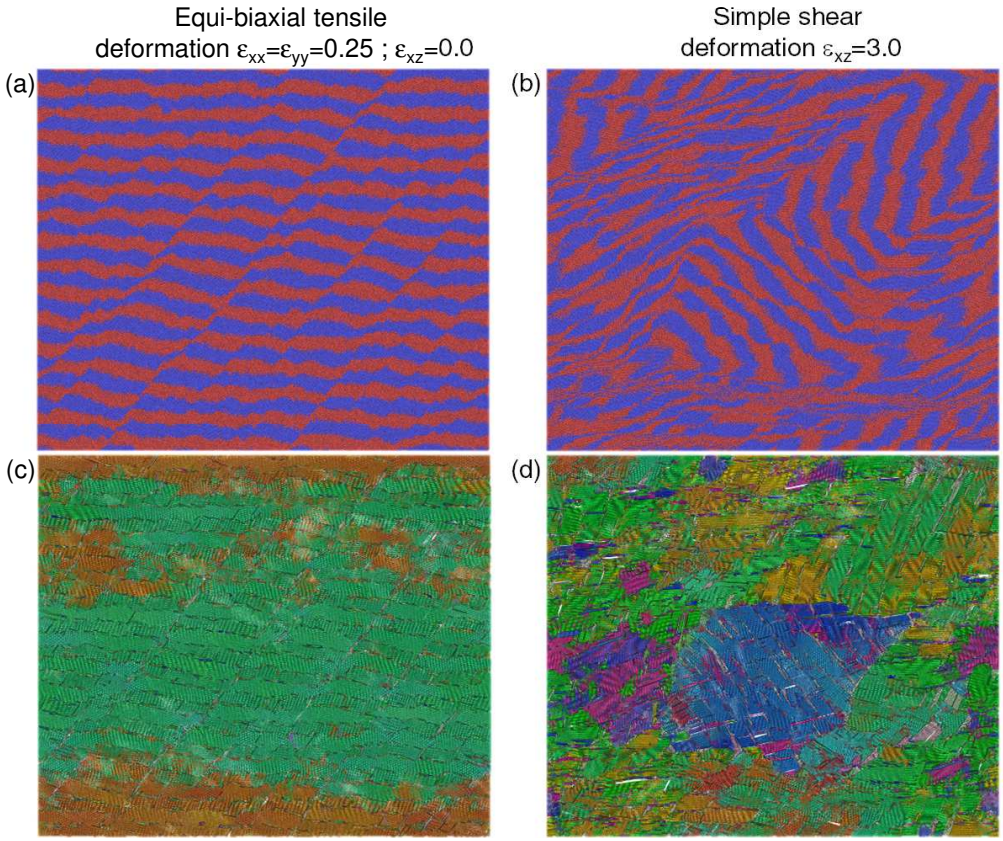

Figure 9.6: Snapshots of the $\theta = 5°$ misoriented system with 10 and 30 layers (supercell) after simple shear deformation up to $\varepsilon = 3.0$. (a,b) Atoms color coded after their type, Cu atoms are in shown blue and Au atoms are in shown in red. (c,d) Atoms are color coded according to their local orientation along the z-axis. The corresponding colormap is shown in Fig. 9.4.

created at the interfaces. The spacing between the steps is proportional to the misorientation angle θ. As described in the previous chapters under parallel shear to the interface, FCC multilayers accommodate the deformation by interface sliding. Thus the steps here disrupt the flat dislocation network at the interfaces and act as obstacles the dislocation have to climb to allow for interface sliding. This translates into an increase of the interfacial shear strength. Zhang et al. (2016) noted a similar behavior for the Cu|Nb system under simple shear parallel to the interface.

The second difference with lattice misorientation happens at larger shear strain with a stress reduction for $\theta \neq 0°$ in Fig. 9.2(b). This stress reduction corresponds to the sudden increase of the slope of the averaged w^l_{RMS} as a function of strain in Fig. 9.2(a). The slope increase can be traced down to the appearance of waviness in the layer shapes as seen in Figs. 9.4(a-h). At larger strain, $\varepsilon > 2$, the plateau observed for the w^l_{RMS} value is attributed to the layers folding as shown in Fig. 9.3(d). The stress reduction corresponds to a burst of dislocations

crossing several layers with the two nucleation points shown by white arrows in Fig. 9.4(c). As the strain increases, the growth of a twinned area is observed, in purple in Figs. 9.4(c-g). This growth mechanism is compatible with twin growth from grain boundary with successive emission of partial dislocation on successive $\{111\}$ planes (Anderson et al., 2017).

At the point where the twin appears (Fig. 9.4(c)), one can already note that the local lattice orientation starts to shift toward the [011] direction (Fig. 9.5(c)). Further shearing rotates the twinned area back into the main matrix orientation.

The relevance of the biaxial deformation on the overall mechanism is tested by shearing directly the $\theta = 5^\circ$ system. As Fig. 9.2(a) shows, just misaligning the lattice by an angle θ is not enough to trigger layer rotation and folding. This indicates that the shear bands created during biaxial tensile deformation are necessary to create stress concentration points. The biaxial deformations, via the formation of shear bands, introduce some misalignment on both side of the sheared areas as indicated by the spread orientations in Fig. 9.5(a). This misalignment across the system could be a starting point for the rotation observed during simple shear and the vortex formation observed experimentally.

The supercell calculations revealed that strain hardening is drastically reduced, which indicates that the strain hardening is mostly the result of a size effect acting only on “small” systems. Indeed the system starts first to respond to the shear deformation by creating a large wavy structure as seen in Figs. 9.4(a-c). Due to image forces acting across the periodic boundaries, such wavy structure formation can be hindered.

9.5 Summary

Compared to the previous chapter that described calculations of sliding on surfaces of metallic multilayers, the model described here made abstraction of the indenter by deforming a representative volume. This model successfully reproduce the formation of vortex structures at strain much smaller than the one discussed by Pouryazdan et al. (2017). This preliminary work show that the misorientation of the $[111]$ axis with the direction growth combined with the presence of shear bands crossing the interfaces is critical regarding multilayer deformation at the nanoscale. It can modify the response of the multilayer under shear deformation, from deformation accommodated at the interfaces by sliding to vortex formation with drastic lattice rotation.

10. Compression of Cu|Au nanopillars

10.1 Introduction

In this chapter the evolution leading to the failure of the Cu|Au multilayer system under compression is investigated. Metallic multilayers, while showing higher strength compared to their bulk counterparts, suffer from catastrophic failure (Zhang et al., 2014). As seen in the previous chapters, multilayer materials at the nanoscale exhibit a wide range of different deformation behaviors, which depend on the loading conditions, structure of the interfaces and composition of the layers. Under compression shear-banding is the primary failure mechanism in multilayered materials at the nanoscale (Li et al., 2009). These instabilities were observed for several crystalline systems, including Cu|Au, and attributed to a reduced strain hardening ability (Wei et al., 2002, Li et al., 2010, Wang et al., 2011).

Earlier work by Schwaiger et al. (2012) shows how valuable information can emanate from the collaboration between experiments and simulations, such as the effect of experimental procedures on the shape of a nanopillar after compression. Therefore, in this chapter the models are motivated and validated on input from experiments in order to provide a quantitative comparison between experiments and MD simulations. Thanks to the collaboration with Ruth Schwaiger (KIT) precise information and results about experiments on Cu|Au nanopillar compression were accessible. Figure 10.1(a-d) shows the typical outcome of such an experiment. The diamond indenter first contacted the pillar somewhere on the its flat top (Fig. 10.1(a)). Deformation then lead to the gradual compression of the pillar and eventually to the nucleation of a shear band (indicated by a “1” in Fig. 10.1(b) and (c)). Shear banding localized further deformation and lead to the extrusion of a wedge shaped region near the top of the pillar. Further compression nucleated a second shear band, initiated right where the wedge has slid enough to create a surface step that concentrated stress (position “2” in Fig. 10.1(c) and (d)). Deformation then continued along this secondary shear band and eventually to the extrusion of a larger wedge shaped region.

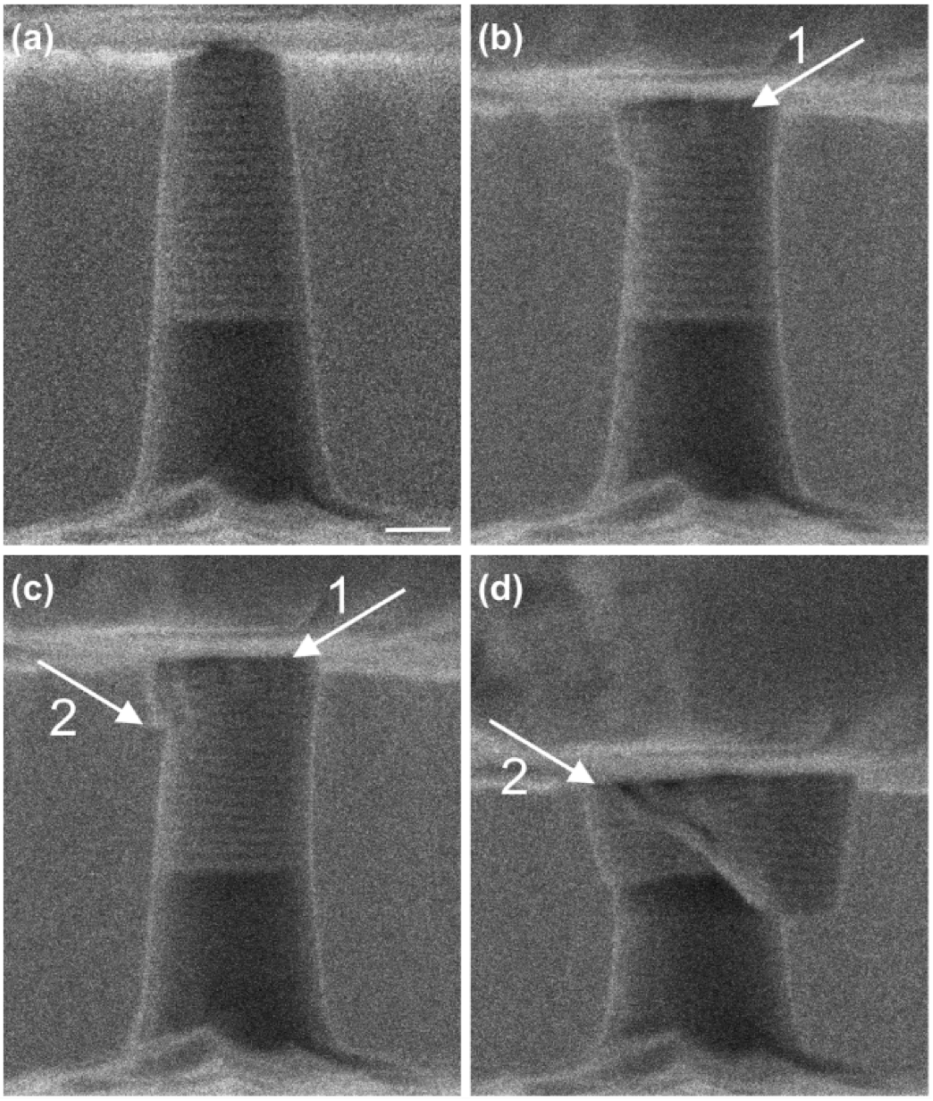

Figure 10.1: Scanning electron microscope images of deformation and failure during compression of a nanolaminate pillar comprised of 40 layers of 25 nm thickness. (a) Initial pillar. (b) The deformation localizes at the top of the pillar and (c) forms a step on the top half (d) followed by failure through an interlayer shear-band.(Schwaiger, 2015)

10.2 Methods

To rationalize these observations molecular dynamics (MD) calculations were carried out with varying monocrystalline layer thickness from 5 nm to 25 nm, resulting in systems of up to 380 million atoms with a total pillar height of 300 nm (Fig. 10.2(a)). These pillars are smaller than their experimental counterparts (Fig. 10.1(a)) but have identical layer thickness and aspect ratio. The interaction between Cu and Au was modeled using the embedded atom method potential described in chapter 6. The flat, rigid indenter was obtained similarly to the spherical indenter in chapter 8. This rigid indented was obtained by freezing the structure of a $Cu_{50}Zr_{50}$ metallic glass obtained by melting a random solid solution at 2500K and quenching it down to 0 K at a rate of 6 K.ps^{-1}. A purely repulsive Lennard-Jones potential with interaction parameters $\varepsilon_{Cu} = 0.4093$, $\sigma_{Cu} = 2.338$, $\varepsilon_{Au} = 0.4251$, $\sigma_{Au} = 2.485$ acted between pillar and indenter (Halicioğlu and Pound, 1975). Note that the disordered nature of the indenter introduced finite friction between indenter and pillar. The indenter was pressed onto the pillar by displacing it at a constant strain rate of 0.8×10^8 s^{-1}. The whole pillar was kept at 300K using a Nosé-Hoover thermostat (Shinoda et al., 2004) with a relaxation time constant of 0.5 ps. A few rows of atoms at the bottom were fixed in space to anchor the pillar to the substrate.

To facilitate comparison with experiments, the MD simulations were evaluated in the same way the experiments were evaluated: Stress $\sigma = F/A$ is computed by dividing the force F on the indenter by the cross-sectional area A at a position $1/5$ along the pillar from its top. Since experiments only have access to a side view (Fig. 10.1) and must assume rotational symmetry, the influence of this assumption on the stress-strain curves was investigated. The exact area A was computed from the convex hull of the cross section at the given height (Fig. 10.2(c)). The smallest and the largest diameters of the pillar were also computed. These measurements were used to estimate error in the determination of A (as shown by the dashed lines in Fig. 10.2(c)). The lateral strain in the pillar was determined with these measurements, $\varepsilon = \ln(1 + (d - d_0)/d_0)$ where d_0 is the initial diameter.

The response to deformation of an MD system strongly depends on the initial defects present in the system (Zepeda-Ruiz et al., 2017). In order to build a reasonable MD model, the influence of the introduction of different sources of defects on the MD model was first assessed: 1) Interface defects: as seen in chapter 7, the structure of defects at the interface is heavily influenced by intermixing. Therefore the interfaces between Cu and Au layers were mixed over a finite interface width of 15 Å. 2) Surface defects: surface roughness on the pillar as introduced by cutting atoms above a plane that follows random self-affine scaling (Persson et al., 2005) with Hurst exponent 0.8 and root-mean square (rms) slope of 0.1 (Fig. 10.2(b)). 3) Bulk defects: as a representative volume defect, five screw dislocations were introduced

at random positions and orientations crossing the entire system. The dislocation lines were introduced using the isotropic elastic solution (Anderson et al., 2017), all the atoms were displaced by a distance u_3 parallel to the dislocation line direction:

$$u_3 = \frac{\mathbf{b}}{2\pi}\text{atan}\left(\frac{x_2}{x_1}\right)$$

Where x_1 and x_2 are the atomic positions in a plane perpendicular to the dislocation line direction, and $\mathbf{b}$ is the Burgers vector of the dislocation. As dislocations cross both Cu and Au layers the Burgers vector norm $||\mathbf{b}||$ was set as:

$$||\mathbf{b}|| = \frac{||\mathbf{b}_{Cu}|| + ||\mathbf{b}_{Au}||}{2}$$

Where $||\mathbf{b}_{Cu}||$ and $||\mathbf{b}_{Au}||$ are the Burgers vector norms in Cu and Au, respectively.

10.3 Results

Figure 10.3(a) shows the influence of initial defects on the plasticity response of the nanopillar systems under compression for $\lambda = 5$ nm. All the systems reach a similar flow stress around 2.4 to 2.8 GPa. The most significant difference observed concerns the yield stresses. The perfect system yields at $\sigma \sim 6.1$ GPa with a significant drop to the aforementioned flow stress. The introduction of defect at the interface via intermixing the Cu and Au elements already reduced the yield stress overshoot down to $\sigma \sim 4.6$ GPa. The addition of defect at the surface of the nanopillar reduces the overshoot even more to $\sigma \sim 4.0$ GPa. A minimum value for the yield stress is observed at $\sigma \sim 3.2$ GPa after the introduction of screw dislocations in the system. From these observations, all the subsequent systems in this chapter will be modeled with defects at the interfaces and at the surface.

Figure 10.4 shows the results obtained for the different definitions of the cross-section area A (smallest and largest cross-section, exact convex hull). In all the cases it was observed that systems yield at $\sigma \sim 4$ GPa and ε ranging from 0.1% to 1%, followed by some strain softening. The maximal lateral strain is achieved for the largest cross-section definition with $\varepsilon \sim 25\%$, the smallest cross-section reaches $\varepsilon \sim 22\%$ and the exact convex hull area $\varepsilon \sim 19\%$. In all the cases the final stress value is around $\sigma \sim 2.3$ GPa.

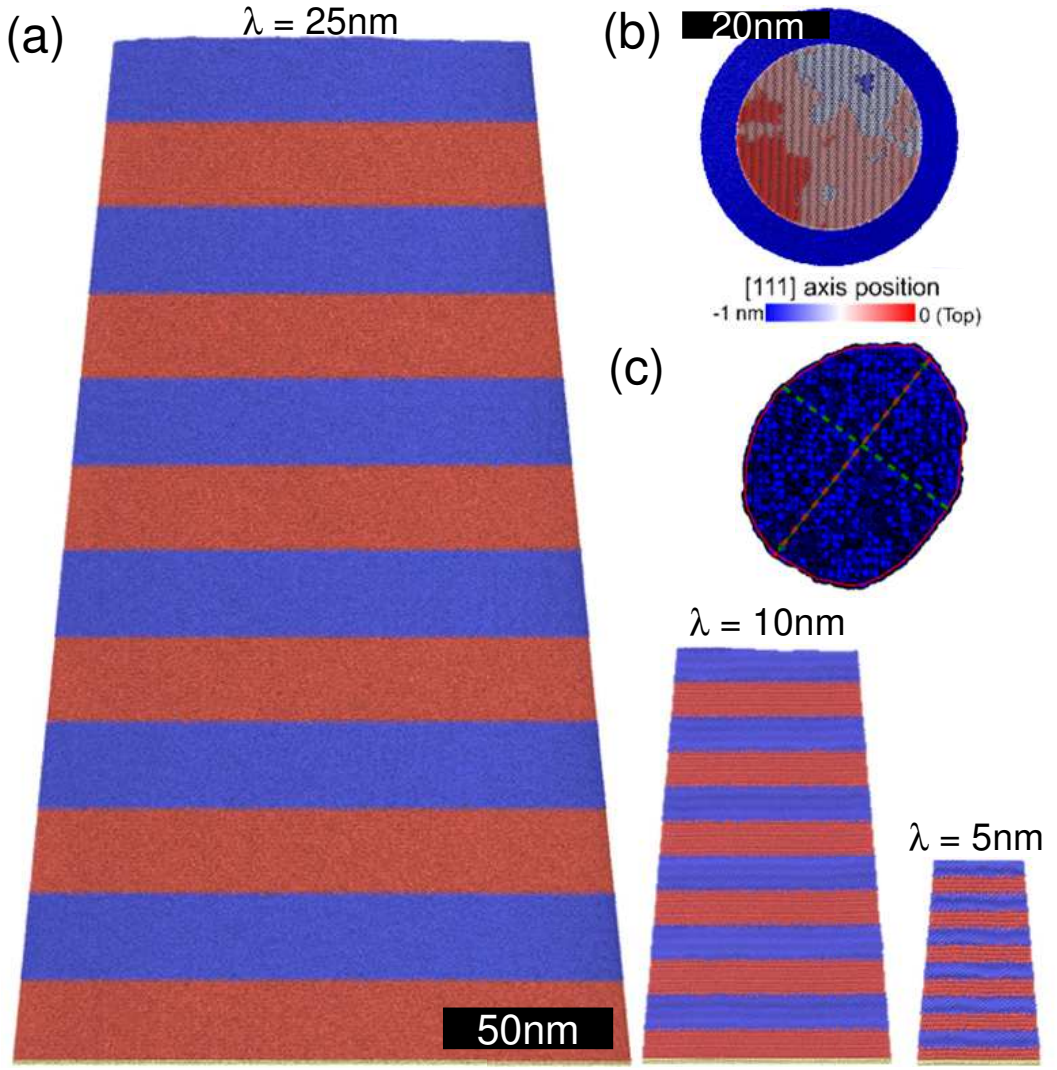

Figure 10.2: (a) Side view of the pillar models with layer thickness of $\lambda = 25$, 10 and 5 nm used in the MD simulations. Atoms are color coded according to their type and mobility with mobile Cu atoms in blue and Au atoms in red, fixed Au atoms in yellow. (b) Top view of the pillar model with $\lambda = 5$ nm showing a realization of random surface roughness. Atoms are colored after their position along the $[111]$ axis. (c) Cross-section at $1/5$ of the pillar height during compression used to compute the cross-sectional area from the MD calculations. Red and green dashes lines show the longest and shortest half-axes of the cross-section.

The models are now compared with the experimental dataset. The open symbols in Fig. 10.3(b) show that, for the experimental setup, the stress rose to a maximum of $\sigma \sim 1.8$ GPa at $\varepsilon \sim 4\%$ strain and then dropped during subsequent deformation. The material hence softened during deformation.

The stress-strain curves in Fig. 10.3(b) clearly show that the overall magnitude of the yield and flow stress depends on the thickness λ of the layers. The model at experimental scales

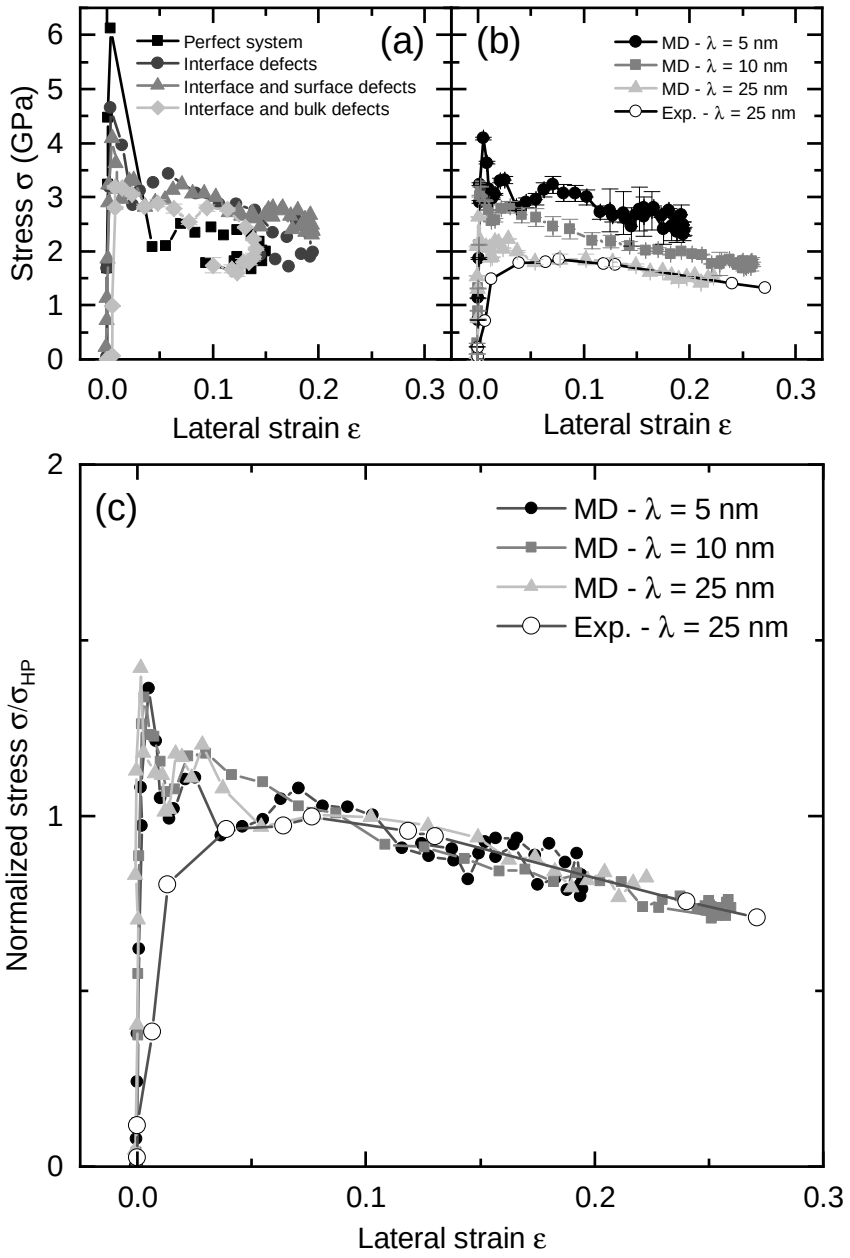

Figure 10.3: (a) Stress-strain curves obtained from MD simulations with controlled defects (see text). (b) Stress-strain curves of pillar compression obtained in experiments and through MD simulations for different layer thickness λ. The lateral true strain and the area require to compute σ are determined from reference cross-sections at $1/5$ of the pillar height from the top of the pillar in all cases. (c) Stress-strain curves from panel (b) normalized by the Hall-Petch flow stress, $\sigma_{HP} = \sigma_0 + k_y \lambda^{-1/2}$, fitted to the yield stress obtained in the MD simulations. The error bars of the simulated data are obtained by repeating the area measurement at distances ± 1 nm of the reference cross-section.

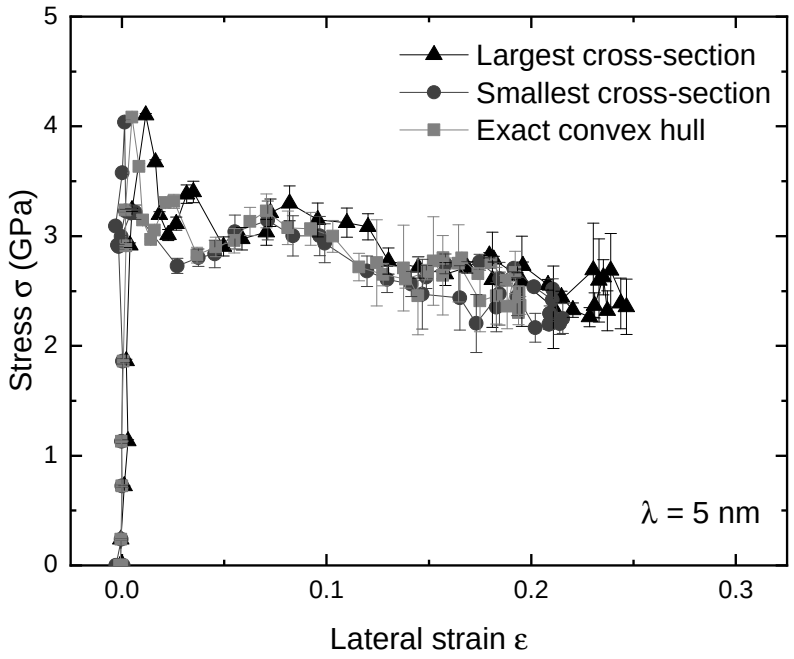

Figure 10.4: Stress-strain curves of pillar compression obtained with different approximations for the area determination (see text). The error bars are obtained by repeating the area measurement at distances ± 1 nm of the reference cross-section.

($\lambda = 25$ nm) exactly reproduces the experimental curves in the flow region, given that at least surface roughness is introduced into the system. To test whether the system could follow the Hall-Petch relationship, the stress σ was normalized by $\sigma_{\mathrm{HP}} = \sigma_0 + k_y \lambda^{-1/2}$. The parameters σ_0 and k_y were obtained from performing a linear fitting on the yield stresses obtained with the simulations (ignoring the stress overshoot). Figure 10.3(c) shows that the normalization $\sigma/\sigma_{\mathrm{HP}}$ collapses the data of all of the calculations in the flow region.

The deformation in the simulations can be classified as occurring homogeneously (Fig. 10.5(a)) or heterogeneously through the formation of a shear band (Fig. 10.5(b,c)). Formation of a shear band eventually leads to a failure-mode similar to the one observed experimentally (Fig. 10.1). A key observation in the simulations is that perfectly flat surfaces always lead to homogeneous deformation (Fig. 10.5(a)) while rough surfaces show heterogeneous deformation and failure (Fig. 10.5(b)).

To clarify the role played by roughness pillars with the simplest model for "roughness" were created, a single atomic step on their surface (Fig. 10.5(c), left column). This model "roughness" already lead to a deformation mechanism dramatically different from perfectly flat surfaces. A shear band is clearly visible already at an applied strain of $\varepsilon = 0.20$, manifested by a series of kinks in the Cu|Au heterointerfaces and extrusion of a wedge shaped part of the pillar (Fig. 10.5(c), right column). Similarly, compressing a nanopillar

with a flat surface using a misaligned indenter (Fig. 10.5(d)) also yield to the formation of a shear band. Figure 10.6 shows the deformation stages of the model "roughness" nanopillar under compression. One can see that the first dislocations nucleate at the junction of the interface and the free surface in the uppermost Au layer (Fig. 10.6(b)). These dislocations cross several interfaces and glide on one given plane (Figs. 10.6(c-e)). At this stage the shear band is not visible on the pillar. At a compressive strain of $\varepsilon = 0.05$, the dislocation activity is concentrated in the three uppermost Au layers and the aforementioned glide plane crossing the interfaces (Fig. 10.6(f)). There is now a clear kink present at the interfaces, signs of the shear band formation. Further compression accentuate the shear band and dislocation activity along this plane (Figs. 10.6(g-i)), leading to the extrusion of a wedge shape section of the pillar.

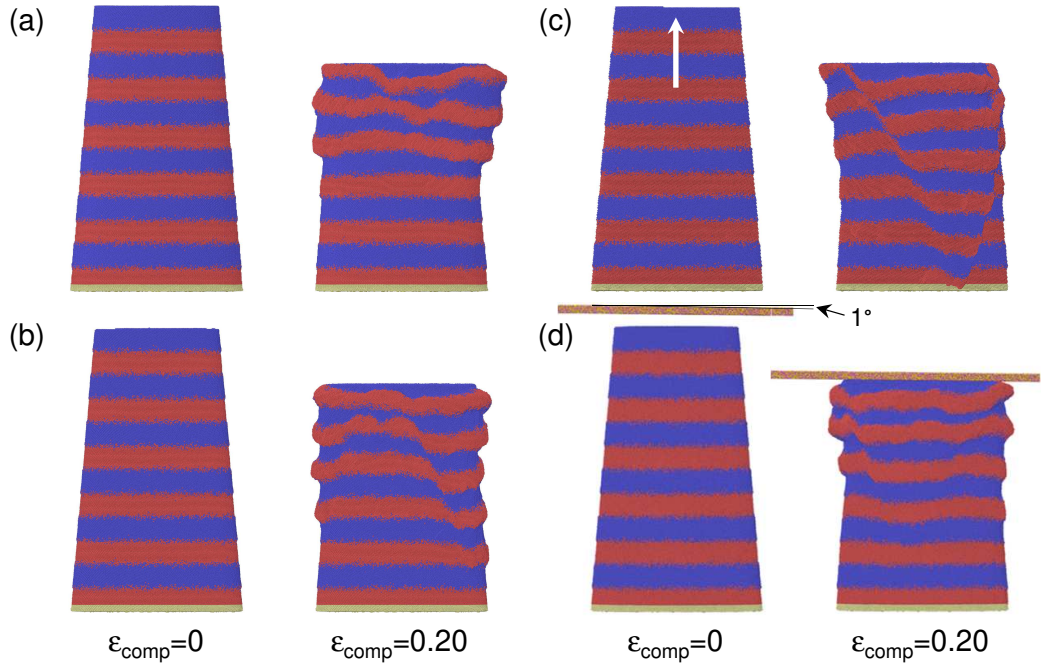

Figure 10.5: Comparison of deformation mechanism for (a) an atomically flat nanopillar, (b) a nanopillar with a random roughness on the top with a RMS slope value of 0.1, (c) a nanopillar with an atomic step at the surface and (d) an atomically flat indenter using an indenter tilted by 1°. The left column correspond to the undeformed stage of the systems, while the right column correspond to the system after at normal compressive strain value of 0.2. Layer thickness in set to 5nm, the indenter have been removed for clarity in (a-c). Atoms are color coded after their type and mobility, Cu are in blue, Au are in red and fixed atoms are in yellow. Arrow in (c) shows the initial position of step at the surface.

Finally, control calculations were carried out using single crystal Au pillars of 60 nm (total pillar height in the $\lambda = 5$ nm case). Figure 10.7 show that the pillar deforms homogeneously even in the presence of surface steps (or self-affine roughness, not shown here). After a

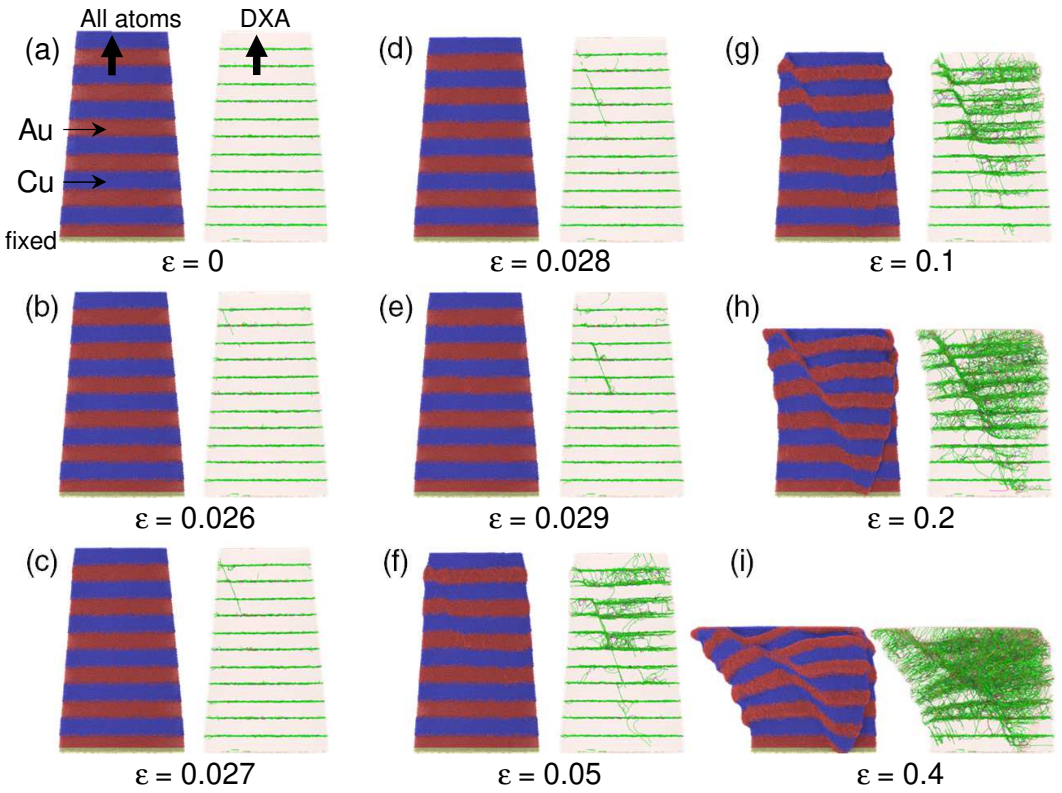

Figure 10.6: Deformation stages of a Cu|Au nanopillar with layer thickness λ=5 nm under compression. The arrows in (a) mark the location of the single atomic step at the surface. Atoms are color coded after their type and mobility with red atoms being Au and blue Cu, the yellow atoms are fixed. The dislocation extraction algorithm (DXA) was used to display the dislocations at each deformation stage. The shaded surface represents the nanopillar surface, Shockley partial dislocations are in green and stair-rod dislocations in purple.

dislocation nucleates at the surface (Fig. 10.7(b)) it then crosses the full pillar, vanishing at the side wall and leaving behind a complementary step (Fig. 10.7(c-d)). Unlike in multilayers, this dislocation do not imprint its signature into the bulk of the material. Further compression lead to new dislocations nucleating from the top pillar surface (Fig. 10.7(e)). While some dislocations escape the pillar, other react in the bulk or pill up against the fixed layer at the bottom (Fig. 10.7(f-i)).

10.4 Discussion

Consistent with previous observation from calculations of bulk or surface deformation (Zepeda-Ruiz et al., 2017, Klemenz et al., 2018), the defect-free system (Fig. 10.3(a)) yielded at a stress roughly double the flow stress of the material. The introduction of interface defects

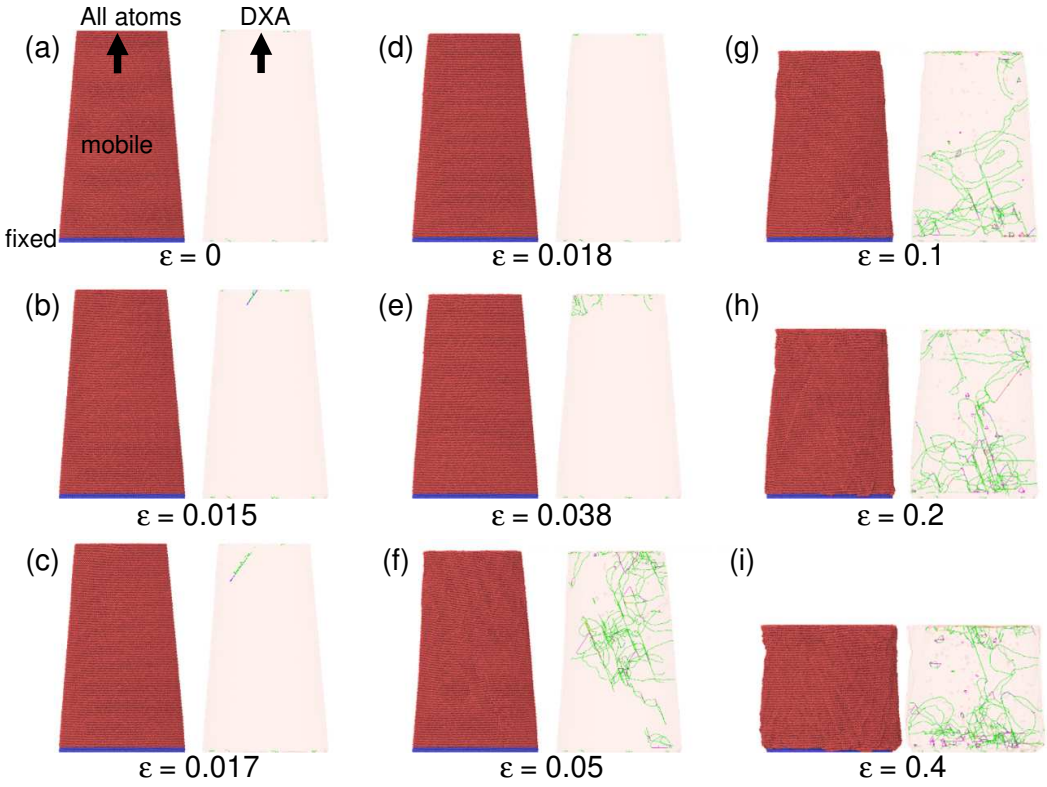

Figure 10.7: Deformation of a 60 nm Au single crystal nanopillar under compression. The arrows in (a) mark the location of the single atomic step at the surface. Atoms are color coded after their mobility with red atoms being mobile and blue fixed. The dislocation extraction algorithm (DXA) was used to display the dislocations at each deformation stage. The shaded surface represents the nanopillar surface, Shockley partial dislocations are in green and stair-rod dislocations in purple.

reduces this value and adding surface defects or bulk defects lead to smoother stress-strain curve qualitatively comparable to the one obtained in experiments. The choice was made to only use interface and surface defects as the insertion of full dislocation lines artificially creates preferential strain accommodation path. Eventually leading to artificial premature deformation at the bottom of the nanopillar in the earlier stage of deformation. A solution would be to use dislocation loop instead of dislocation line crossing the whole model, but such small dislocation are difficult to stabilize in system with a small layer thickness as they would be attracted to the free surfaces or interfaces (Yamakov et al., 2001). Another solution would involve the introduction of stable prismatic loops.

The area definition does not have a big impact on the stress values, while it shifts significantly the strain values due to the definition employed for the strain. These results indicate that using the apparent diameter to define the cross-section area is a valid approximation, although a second measurement perpendicular to the first one could improve the accuracy in experiments.

The results (Fig. 10.3(c)) show that even down to a layer thickness of $\lambda = 5$ nm the behavior of the system could follow Hall-Petch relationship. Due to the small number of data points used in the fitting procedure, it is still hard to differentiate between a $1/r^2$ and $1/r$ scaling for this system. This behavior may depend on the deformation mode induced by the external load.

Regarding the catastrophic failure mechanism, it is remarkable that the single step is sufficient to nucleate a shear-band. This is because edges, or indenter misalignment, concentrate stress that trigger the emission of a single dislocation into the bulk. This dislocation leaves behind steps at the Cu|Au heterointerfaces, essentially imprinting the surface structure into the bulk of the material. Once a shear band has nucleated it will accommodate all subsequent deformation since the steps or kink created by the band themselves concentrate stress. Figures 10.5(c) and 10.6 also shows that the individual pillar can host more than one shear band. The final snapshot of these figures clearly shows an extruded, wedge-shaped region of the pillar that is bounded by two shear bands.

The explanation for shear banding relies on the existence of domains with varying elastic modulus affecting the dislocation motions in the multilayer systems. While the surface flaws are the reasons for the nucleation of an initial dislocation that constitutes the onset of the shear band, the existence of alternating sequences of hard and soft materials is the fundamental reason for its stabilization (Knorr et al., 2013).

10.5 Summary

In summary, the strength of multilayer nanopillars was obtained from atomic-scale simulations and showed excellent agreement with experiments. The pillar localized shear in shear bands that lead to catastrophic failure of the material. This chapter demonstrated that the nucleation process is extremely sensitive to surface flaws but the stabilization of the shear band is a result of the imprinting of the surface flaws into the interface structure of the multilayers. Surface flaws associated with multilayer materials that present contrast in their mechanical properties lead to stress concentration. Fine tunning the barrier strength of interfaces to avoid imprinting the interfaces is thus a route that could solve the issue of catastrophic failure.

Part IV.

Conclusion

11. Conclusion

Two systems having semi-coherent interfaces were studied here. Their structures were systematically characterized, with a strong focus on the interface structures. Their deformation and failure mechanisms were then monitored under various loading conditions. The two systems represent two approaches to fine tune the interface properties. The first approach, described in part II, used two partly miscible FCC elements, Cu and Ni, with a small lattice mismatch. A third larger metallic element, Ag, was alloyed in the Cu layers in order to fine tune the lattice mismatch. The effect on the mechanical properties was monitored. The second path, detailed in part III, used two fully miscible FCC elements, Cu and Au, with a large lattice mismatch. The interface defects were strongly influenced by the layers interdiffusion as shown in chapter 7 which greatly affect the mechanical properties. With this later system, the impact of surface defects on the mechanical response was studied in chapter 10.

The use of molecular dynamics combined with Monte Carlo in chapters 3 and 4 allowed to bring toward thermodynamic equilibrium the $Cu_{1-x}Ag_x|Ni$. Specific segregation patterns of Ag were noticed, mainly in the Cu layers at the interfaces. Ag segregation was observed in zones of larger free volume or under hydrostatic tensile stress, such as the dislocation network nodes at the interface or at the grain boundaries for the polycrystalline system. These areas have been linked to zones of lower solute energy using an EAM averaged method that introduced a synthetic averaged element. This method allowed to efficiently compute solute energy of Ag at the interface with only one calculation per position instead of several calculations for a large number of solid solution state. These calculations also showed that the segregation follows a chain reaction as the solute energy becomes increasingly favorable with increasing number of Ag atoms at the dislocation nodes. In the case of the polycrystalline system, a preferential segregation path of Cu in the Ni layer was noticed, with the Cu atoms following the grain boundaries. From these equilibrated systems the dislocation network nodes were identified as nucleation points for dislocations when the system is under load. The dislocations bow out of these nodes in the Cu layers on three different $\{111\}$ planes which can then intersect to form sessile tetrahedron lock. Alloying Ag in Cu translated in an increase of the lattice mismatch between the two layers and thus an increase of the density of dislocation nodes at the interface. The increase of node density

translates in a higher probability to form tetrahedrons. Interfaces were also more opaque to dislocations with Ag content increasing. Lastly, the Ag aggregates pinned the dislocation network at the interfaces leading to an increase of the interface shear strength.

Contrary to the CuAg|Ni system, the study of the Cu|Au system started with the development of an EAM potential. Chapter 6 started with the observation that none of the pre-existing EAM potentials in the literature could describe the thermodynamic and mechanical properties of both unary and binary Cu-Au phases. During the fitting procedure several binary EAM potentials were benchmarked, leading to a comprehensive comparison of the mechanical and thermodynamic properties for each of them. Chapter 7 showed that the miscibility in the Cu-Au system had a strong influence on the interfacial shear strength. Indeed, as soon as the first atomic layer on each side of the interface were intermixed, the interface shear strength increased by an order of magnitude. Further intermixing did not have such a strong impact on the interface shear strength. As the intermixing distance across the interface increased, the defect network (i.e. dislocations and stacking faults) changed from a quasi 2D regular structure to a 3D complex structure that hindered dislocation motion in the interfacial planes. A parallel can easily be drawn between this mechanism and the one observed with the Ag aggregates in chapter 5.

In Chapter 8, 9 and 10 the systems setup investigated were directly related to experiments such as nanoscratching and nanopillar compression. Defects that experimentally occur (i.e. growth misalignment, tool misalignment, surface roughness) were modeled and their effect on the different deformation mechanisms were assessed. Using molecular dynamics a nano scratching setup was reproduced at the expense of some unphysical dislocation interactions due to simulation cell size limitation. This led to a complete redesign of the calculation setup in order to make abstraction of the indenter itself. With this new system a mechanism and the necessary conditions to form vortexes at the nanoscale on metallic multilayers were proposed. The misalignment between the $[\bar{1}\bar{1}1]$ axis and the growth axis lead to $\{111\}$ glide planes in the multilayers slightly tilted toward the interface planes. This caused the dislocations to pile up against the roughness at the interfaces and eventually led to a rotation of the structure, i.e. a vortex embryo.

Finally the impact of defects on nanopillar structures were investigated. It was first noticed that in order to properly model these nanopillar and be able to compare those results with experimental ones, some initial defect had to be inserted in the system. The failure of the nanopillar by shear banding was found to be sensitive to the roughness of pillar top surface. With a perfectly flat surface the nanopillar deform uniformly without any catastrophic event. On the other hand any roughness (or indenter misalignment) can act as stress concentration point and lead to failure via shear banding in the Cu|Au nanopillar setup.

Overall the two systems, CuAg|Ni and Cu|Au, showed that the usage of specific defects, both chemical and crystallographic, is a route to explore to fine tune properties of interfaces in order to build multilayer materials and meet specific requirements. Over the course of this dissertation several large scale simulations have shown that MD calculations could provide some information at length scale accessible experimentally. The best example is the polycrystalline structure in chapter 4 that can readily be compared with atom probe experiment results. The nanopillar calculations in chapter 10 showed that similar layer thickness could be reached while the total number of layer in the nanopillar is still too large for the actual computational power available.

As shown in this dissertation, the interfaces play a major role in metallic multilayers. In most of the existing literature, MD models use flat interfaces that do not grasps the complexity of the interactions between dislocations and interfaces. By using MC/MD methods or artificial intermixing systems that are closer to the experimental ones have been created. Descriptions of the interfaces at the atomic scale from the experimental point of view is thus important to properly model and validate systems via MD.

Part V.

Appendix

A. Comparison of MC/MD methods

In this section we compare the atom-swap MC/MD and VC-SGC MC/MD methods described in sections 2.3.2 and 2.3.3, respectively. We ran simulations using both methods on the minimum simulation cell size describe in Tab. 3.2 for the $Cu_{0.90}Ag_{0.10}$|Ni system containing approximately 50,000 atoms.

The VC-SGC MC/MD method only allow for the usage of a limited number of processors for such small system. Because this method is parallelized, the cell volume is split in domains that must be independent from each other, and each of these domains is then allocated to a processors. In order to achieve this division, each domain dimensions must be at least four times the potential cutoff length. In our case, the VC-SGC MC/MD method can only run on 12 processors for the minimum cell. Thus, we reduced the length of each MD run to 50 fs to be able to run enough MC/MD sequence within a reasonable amount of computing time.

We ran calculations using the atom-swap MC/MD method with both 20 ps and 50 fs MD runs and 650 MC/MD sequences. Figures A.1(a) and (b) do not show any noticeable difference regarding Ag segregation in the Cu layer with the variation of the MD runs time. For the VC-SGC MC/MD method we used a constraining value $\kappa = 1000$ to keep the fluctuation of concentration to a minimum. Table A.1 the initial and final concentrations (after 650 MC/MD sequences) of Cu, Ag and Ni. With the applied constrain, the concentrations stayed within 0.2 at.% of their initial values. Figures A.1(b) and (c) compare the atom-swap MC/MD and VC-SGC MC/MD methods. We can see that the overall results are the same, with Ag segregating in the Cu layer without diffusing in the Ni layer. The interface between the Cu and Ni layer is smoothed out with the interdiffusion of Cu and Ni over a distance of about 1 nm.

Table A.1: Concentration of the species in the $Cu_{0.90}Ag_{0.10}$|Ni system before and after VC-SGC MC/MD calculation.

Element	initial (at.%)	final, after 650 MC/MD sequences (at.%)
Cu	42	42.1
Ag	4.6	4.4
Ni	53.4	53.5

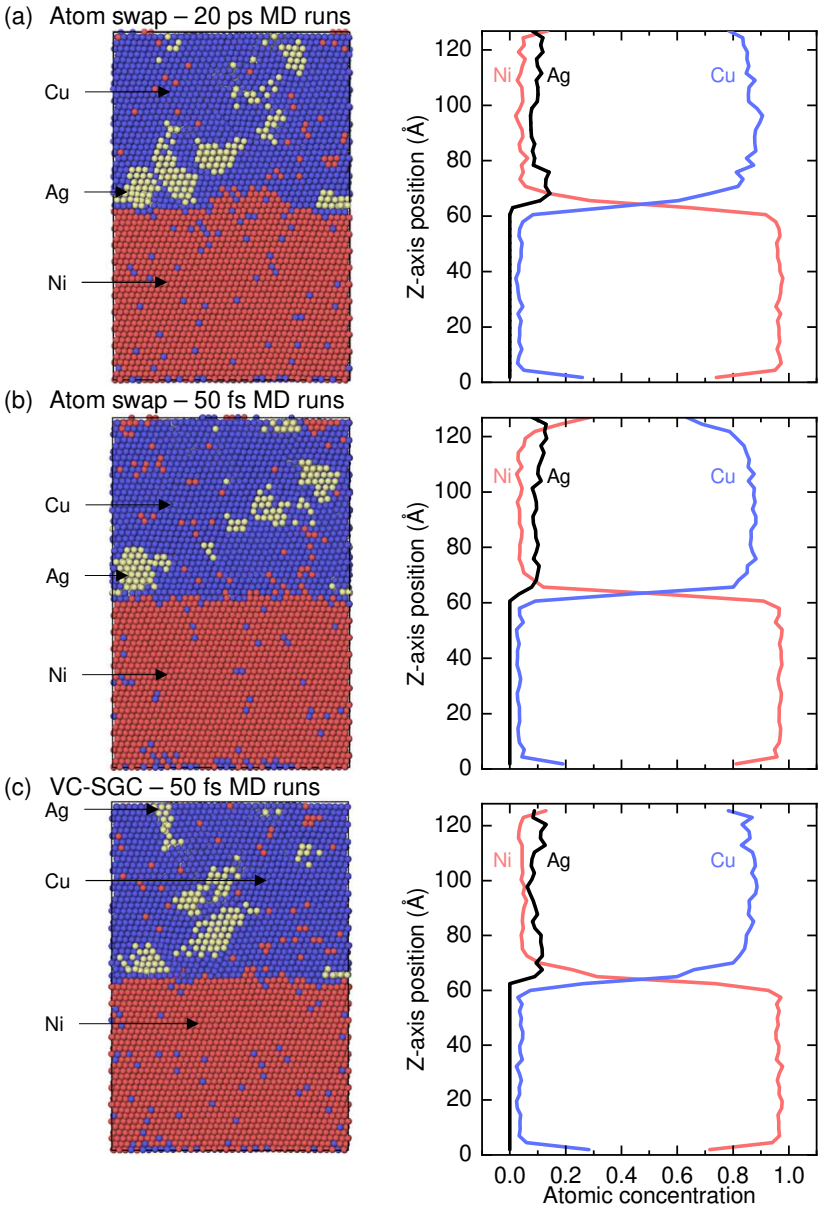

Figure A.1: $Cu_{0.90}Ag_{0.10}|Ni$ systems and concentration profiles along the $[\bar{1}\bar{1}1]$ axis after 650 MC/MD steps using (a) the atom-swap method with MD runs of 20 ps, (b) the atom-swap method with MD runs of 50 fs, (c) the VC-SGC method with MD runs of 50 fs.

Symbols and Abbreviations

Abbreviations

AEAM Average Embedded-Atom Method

BCC Body-Centered Cubic

CNA Common Neighbors Analysis

DFT Density Functional Theory

DXA Dislocation eXtraction Algorithm

EAM Embedded-Atom Method

FCC Face-Centered Cubic

HCP Hexagonal Closed Packing

MC Monte Carlo

MD Molecular Dynamics

NS Nested Sampling

PTM Polyhedral Template Matching

SEM Scanning Electron Microscope

SGC Semi-Grand Canonical

VC Variance-Constrained

Symbols

ε Applied strain

$\mathbf{k_B}$ Boltzmann's constant

b Burgers vector

β Inverse temperature

λ Layer thickness

γ Local atomic strain

h Planck's constant

Acknowledgments

First of all, I would like to express my sincere gratitude to Peter Gumbsch for giving me the opportunity to work at the Institute for Applied Materials - Computational Materials Science (IAM-CMS). I also would like to thank him for all the discussions and constructive comments that helped this work.

I am grateful to Lars Pastewka for his excellent and motivating supervision all along this journey, for sharing his knowledge and seeking opportunities to promote the work of the people under his supervision.

I am thankful for the Karlsruhe House of Young Scientists (KHYS) travel grant, and William Curtin for welcoming me during my scientific stay in his group as well as helpful scientific discussions. During this stay at the Laboratoire de modélisation mécanique multi-échelle (LAMMM), I had the opportunity to meet amongst others Satish Rao, Francesco Maresca and Wolfram Nöhring whom I would like to thanks for the various fruitful exchange we had.

I had the chance to work in collaboration with Ruth Schwaiger and Thomas Kreuter who were conducting the experimental counterpart of the project, I would like to thank them here for all their valuable inputs.

Next, I would like to thank the developers of the scientific codes that allowed me to conduct my researches. Particularly, Paul Crozier for sharing the atom-swap MC/MD code in a development stage back in 2014, Alexander Stukowski for the variance-constrained MC/MD code and more generally for the development and support of OVITO. Lastly, Gàbor Csànyi and Noam Bernstein for their help on sharing and setting up the nested sampling code they developed. Similarly, I would like to thank the several super computing centers for their support and computing time that allowed me to run the calculations for this thesis: Jülich Supercomputing Centre (projects hka18 and hfr13), ForHLR I and ForHLR II (project "MULTILAYER"), and the bwForCluster NEMO. I further thank the Helmholtz/CAS joint research group funding (HCJRG-217) for the financial support all along this thesis.

Last but not least, I would like to add that working at the IAM-CMS has been a real pleasure and for that I would like to thank all the persons I interacted with over the course of this thesis.

Karlsruhe, February 14, 2019 Adrien Gola

Bibliography

G. J. Ackland and V. Vitek. Many-body potentials and atomic-scale relaxations in noble-metal alloys. *Phys. Rev. B*, 41(15):10324–10333, 1990.

D. P. Adams, M. Vill, J. Tao, J. C. Bilello, and S. M. Yalisove. Controlling strength and toughness of multilayer films: A new multiscalar approach. *J. Appl. Phys*, 74(2): 1015–1021, 1993.

M. P. Allen and D. J. Tildesley. *Computer Simulation of Liquids: Second Edition*. Oxford University Press, 2017.

P. Anderson, T. Foecke, and P. Hazzledine. Dislocation-Based Deformation Mechanisms in Metallic Nanolaminates. *MRS Bull.*, 24(02):27–33, 1999.

P. M. Anderson and C. Li. Hall-Petch relations for multilayered materials. *Nanostruct. Mater.*, 5(3):349–362, 1995.

P. M. Anderson, J. P. Hirth, and J. Lothe. *Theory of Dislocations*. John Wiley & Sons, 2017.

R. J. N. Baldock, L. B. Pártay, A. P. Bartók, M. C. Payne, and G. Csányi. Determining pressure-temperature phase diagrams of materials. *Phys. Rev. B*, 93(17):174108, 2016.

G. D. Barrera, R. H. de Tendler, and E. P. Isoardi. Structure and energetics of Cu-Au alloys. *Modelling Simul. Mater. Sci. Eng.*, 8(3):389, 2000.

C. A. Becker, F. Tavazza, Z. T. Trautt, and R. A. Buarque de Macedo. Considerations for choosing and using force fields and interatomic potentials in materials science and engineering. *Curr. Opin. Solid State Mater. Sci.*, 17(6):277–283, 2013.

N. Beckmann, P. A. Romero, D. Linsler, M. Dienwiebel, U. Stolz, M. Moseler, and P. Gumbsch. Origins of Folding Instabilities on Polycrystalline Metal Surfaces. *Phys. Rev. Applied*, 2(6):064004, 2014.

R. Béjaud, J. Durinck, and S. Brochard. Twin-interface interactions in nanostructured Cu/Ag: Molecular dynamics study. *Acta Mater.*, 144:314–324, 2018.

H. J. C. Berendsen, J. P. M. Postma, W. F. van Gunsteren, A. DiNola, and J. R. Haak. Molecular dynamics with coupling to an external bath. *J. Chem. Phys.*, 81(8):3684–3690, 1984.

B. Bhushan. *Introduction to Tribology*. Wiley, New York, 2002.

K. Binder and D. W. Heermann. *Monte Carlo Simulation in Statistical Physics : An Introduction*. Springer Series in Solid State Sciences ; 80. Springer, Berlin, 4th, enl. ed. edition, 2002.

P. Blöchl. PE Blöchl, Phys. Rev. B 50, 17953 (1994). *Phys. Rev. B*, 50:17953, 1994.

G. Bonny, R. C. Pasianot, N. Castin, and L. Malerba. Ternary Fe–Cu–Ni many-body potential to model reactor pressure vessel steels: First validation by simulated thermal annealing. *Philos. Mag.*, 89(34-36):3531–3546, 2009.

J. A. Borders. Ion back-scattering analysis of interdiffusion in Cu-Au thin films. *Thin Solid Films*, 19(2):359–370, 1973.

V. Borovikov, M. I. Mendelev, and A. H. King. Effects of solutes on dislocation nucleation from grain boundaries. *Int. J. Plast.*, pages 146–155, 2017.

N. S. Burkoff, R. J. N. Baldock, C. Várnai, D. L. Wild, and G. Csányi. Exploiting molecular dynamics in Nested Sampling simulations of small peptides. *Comput. Phys. Commun*, 201:8–18, 2016.

A. Caron and R. Bennewitz. Lower nanometer-scale size limit for the deformation of a metallic glass by shear transformations revealed by quantitative AFM indentation. *Beilstein J. Nanotechnol.*, 6:1721–1732, 2015.

C. B. Carter and S. M. Holmes. The stacking-fault energy of nickel. *Philos. Mag. J. Theor. Exp. Appl. Phys.*, 35(5):1161–1172, 1977.

C. B. Carter and I. L. F. Ray. On the stacking-fault energies of copper alloys. *Philos. Mag. J. Theor. Exp. Appl. Phys.*, 35(1):189–200, 1977.

D. D. Chambliss and S. Chiang. Surface alloy formation studied by scanning tunneling microscopy: Cu(100) + Au-c(2x2). *Surf. Sci.*, 264(1):L187–L192, 1992.

S. D. Chen, Y. K. Zhou, and A. K. Soh. Molecular dynamics simulations of mechanical properties for Cu(001)/Ni(001) twist boundaries. *Comput. Mater. Sci.*, 61:239–242, 2012.

X. Y. Chen, X. F. Kong, A. Misra, D. Legut, B. N. Yao, T. C. Germann, and R. F. Zhang. Effect of dynamic evolution of misfit dislocation pattern on dislocation nucleation and shear sliding at semi-coherent bimetal interfaces. *Acta Mater.*, 143:107–120, 2018.

D. Cheng, Z. J. Yan, and L. Yan. Misfit dislocation network in Cu/Ni multilayers and its behaviors during scratching. *Thin Solid Films*, 515(7–8):3698–3703, 2007.

S. A. Chistjakov, A. M. Gagarin, R. G. Koishibaev, Y. Y. Krjuchkov, V. A. Kuzminikh, V. M. Milutin, V. A. Pirogov, V. A. Petrov, A. D. Pogrebnjak, S. V. Plotnikov, G. E. Remnev, Y. G. Rusin, and V. P. Janovskii. Ion mixing of near surface layers in Au-Cu, Cu-Mo systems irradiated by HPIB. *Phys. Lett. A*, 131(1):73–77, 1988.

B. M. Clemens, H. Kung, and S. A. Barnett. Structure and Strength of Multilayers. *MRS Bull.*, 24(2):20–26, 1999.

F. Cleri and V. Rosato. Tight-binding potentials for transition metals and alloys. *Phys. Rev. B*, 48(1):22–33, 1993.

W. H. Cullen, M. J. Marcinkowski, and E. S. P. Das. A study of the interphase boundary between ilmenite and hematite. *Surface Science*, 36(2):395–413, 1973.

J. D. Currey. Mechanical properties of mother of pearl in tension. *Proc. R. Soc. Lond. B*, 196(1125):443–463, 1977.

M. S. Daw and M. I. Baskes. Embedded-atom method: Derivation and application to impurities, surfaces, and other defects in metals. *Phys. Rev. B*, 29(12):6443–6453, 1984.

F. Delogu and G. Cocco. Molecular dynamics investigation on the role of sliding interfaces and friction in the formation of amorphous phases. *Phys. Rev. B*, 71(14):144108, 2005.

B. N. Dey. Interpretation of the damping behavior of copper-nickel alloys: Existence of a miscibility gap. *Scripta Mater.*, 2(9):501–506, 1968.

B. W. Dodson. Atomistic analysis of the enhanced-modulus effect in metallic superlattices. *Phys. Rev. B*, 37(2):727–730, 1988.

T. M. Donovan and K. Heinemann. High-Resolution Electron Microscope Observation of Voids in Amorphous Ge. *Phys. Rev. Lett.*, 27(26):1794–1796, 1971.

P. Egberts and R. Bennewitz. Atomic-scale nanoindentation: Detection and identification of single glide events in three dimensions by force microscopy. *Nanotechnology*, 22(42): 425703, 2011.

P. Egberts, R. Gralla, and R. Bennewitz. Temporal development of indentation plasticity on the atomic scale revealed by force microscopy. *Phys. Rev. B*, 86(3):035446, 2012.

F. Ercolessi and J. B. Adams. Interatomic Potentials from First-Principles Calculations: The Force-Matching Method. *Europhys. Lett.*, 26(8):583, 1994.

M. L. Falk and J. S. Langer. Dynamics of viscoplastic deformation in amorphous solids. *Phys. Rev. E*, 57(6):7192–7205, 1998.

Q. Feng, X. Song, H. Xie, H. Wang, X. Liu, and F. Yin. Deformation and plastic coordination in WC-Co composite — Molecular dynamics simulation of nanoindentation. *Mater. Des.*, 120:193–203, 2017.

M. W. Finnis and J. E. Sinclair. A simple empirical N-body potential for transition metals. *Philos. Mag. A*, 50(1):45–55, 1984.

S. M. Foiles, M. I. Baskes, and M. S. Daw. Embedded-atom-method functions for the fcc metals Cu, Ag, Au, Ni, Pd, Pt, and their alloys. *Phys. Rev. B*, 33(12):7983–7991, 1986.

F. C. Frank. LXXXIII. Crystal dislocations.—Elementary concepts and definitions. *Lond. Edinb. Dublin Philos. Mag. J. Sci.*, 42(331):809–819, 1951.

F. C. Frank and J. H. V. D. Merwe. One-dimensional dislocations. II. Misfitting monolayers and oriented overgrowth. *Proc. R. Soc. Lond. A*, 198(1053):216–225, 1949.

D. Frenkel and B. Smit. *Understanding Molecular Simulation : From Algorithms to Applications*. Computational Science Series ; 1. Academic Press, San Diego [i.a.], 2. ed. edition, 2002.

L. H. Friedman and D. C. Chrzan. Scaling Theory of the Hall-Petch Relation for Multilayers. *Phys. Rev. Lett.*, 81(13):2715–2718, 1998.

B. Gault, M. P. Moody, J. M. Cairney, and S. P. Ringer. *Atom Probe Microscopy*. Springer Series in Materials Science. Springer New York, 2012.

J. I. Goldstein, D. E. Newbury, J. R. Michael, N. W. M. Ritchie, J. H. J. Scott, and D. C. Joy. *Scanning Electron Microscopy and X-Ray Microanalysis*. Springer New York, 2017.

A. J. Griffin, F. R. Brotzen, and C. F. Dunn. Mechanical properties and microstructures of Al-1%Si thin film metallizations. *Thin Solid Films*, 150(2):237–244, 1987.

G. Grochola, S. P. Russo, and I. K. Snook. On fitting a gold embedded atom method potential using the force matching method. *J. Chem. Phys.*, 123(20):204719, 2005.

C. Gu, F. Wang, P. Huang, T. J. Lu, and K. W. Xu. Altering strength and plastic deformation behavior via alloying and laminated structure in nanocrystalline metals. *Mater. Sci. Eng. A*, 640:24–32, 2015.

P. Gumbsch. Atomistic Study of Misfit Accommodation in Cube-on-cube Oriented Ag/Ni Heterophase Boundaries. *Z. Metallkd.*, 83(7):499–508, 1992.

P. Gumbsch and M. S. Daw. Interface stresses and their effects on the elastic moduli of metallic multilayers. *Phys. Rev. B*, 44(8):3934–3938, 1991.

R. P. Gupta. Lattice relaxation at a metal surface. *Phys. Rev. B*, 23(12):6265–6270, 1981.

T. Halicioğlu and G. M. Pound. Calculation of potential energy parameters form crystalline state properties. *phys. stat. sol. (a)*, 30(2):619–623, 1975.

E. O. Hall. The Deformation and Ageing of Mild Steel: III Discussion of Results. *Proc. Phys. Soc. B*, 64(9):747, 1951.

G. M. Hamilton. Explicit Equations for the Stresses beneath a Sliding Spherical Contact , Explicit Equations for the Stresses beneath a Sliding Spherical Contact. *Proc. Inst. Mech. Eng. C*, 197(1):53–59, 1983.

P. Hirel. Atomsk: A tool for manipulating and converting atomic data files. *Comput. Phys. Commun.*, 197:212–219, 2015.

R. G. Hoagland, T. E. Mitchell, J. P. Hirth, and H. Kung. On the strengthening effects of interfaces in multilayer fee metallic composites. *Philos. Mag. A*, 82(4):643–664, 2002.

R. G. Hoagland, J. P. Hirth, A. Misra, and D. Mitlin. Influence of surface steps on glide of threading dislocations during layer growth. *Appl. Phys. Lett.*, 84(25):5136–5138, 2004.

R. G. Hoagland, J. P. Hirth, and A. Misra. On the role of weak interfaces in blocking slip in nanoscale layered composites. *Philos. Mag.*, 86(23):3537–3558, 2006.

J. D. Honeycutt and H. C. Andersen. Molecular dynamics study of melting and freezing of small Lennard-Jones clusters. *J. Phys. Chem.*, 91(19):4950–4963, 1987.

M. F. Horstemeyer, M. I. Baskes, and S. J. Plimpton. Length scale and time scale effects on the plastic flow of fcc metals. *Acta Mater.*, 49(20):4363–4374, 2001.

J. M. Howe. *Interfaces in Materials : Atomic Structure, Thermodynamics and Kinetics of Solid Vapor, Solid Liquid and Solid Solid Interfaces*. A Wiley-Interscience Publication. Wiley, New York, 1997.

D. Hull and D. Bacon. Chapter 5 - Dislocations in Face-centered Cubic Metals. In D. Hull and D. Bacon, editors, *Introduction to Dislocations (Fifth Edition)*, pages 85–107. Butterworth-Heinemann, Oxford, fifth edition edition, 2011.

J. N. Israelachvili. *Intermolecular and Surface Forces*. Elsevier, Amsterdam, Heidelberg [i.a.], 3. ed. edition, 2011.

T. D. B. Jacobs, G. E. Wabiszewski, A. J. Goodman, and R. W. Carpick. Characterizing nanoscale scanning probes using electron microscopy: A novel fixture and a practical guide. *Rev. Sci. Instrum.*, 87(1):013703, 2016.

T. Jøssang and J. P. Hirth. The energies of stacking-fault teirahedra in f.c.c. metals. *Philos. Mag. J. Theor. Exp. Appl. Phys.*, 13(124):657–670, 1966.

S. Kamran, K. Chen, and L. Chen. Ab initio examination of ductility features of fcc metals. *Phys. Rev. B*, 79(2):024106, 2009.

G. Kaupp. Mechanochemistry: The varied applications of mechanical bond-breaking. *CrystEngComm*, 11(3):388–403, 2009.

M. M. Khruschov. Principles of abrasive wear. *Wear*, 28(1):69–88, 1974.

K. Kikuchi, M. Yoshida, T. Maekawa, and H. Watanabe. Metropolis Monte Carlo method as a numerical technique to solve the Fokker—Planck equation. *Chem. Phys. Lett.*, 185(3): 335–338, 1991.

K. Kikuchi, M. Yoshida, T. Maekawa, and H. Watanabe. Metropolis Monte Carlo method for Brownian dynamics simulation generalized to include hydrodynamic interactions. *Chem. Phys. Lett.*, 196(1):57–61, 1992.

H. J. Kim, S. Karthikeyan, and D. Rigney. A simulation study of the mixing, atomic flow and velocity profiles of crystalline materials during sliding. *Wear*, 267(5):1130–1136, 2009.

C. Kittel. *Introduction to Solid State Physics*. Wiley, New York, 8. ed. edition, 2005.

A. Klemenz, A. Gola, M. Moseler, and L. Pastewka. Contact mechanics of graphene-covered metal surfaces. *Appl. Phys. Lett.*, 112(6):061601, 2018.

I. Knorr, N. M. Cordero, E. T. Lilleodden, and C. A. Volkert. Mechanical behavior of nanoscale Cu/PdSi multilayers. *Acta Mater.*, 61(13):4984–4995, 2013.

J. S. Koehler. Attempt to Design a Strong Solid. *Phys. Rev. B*, 2(2):547–551, 1970.

G. Kresse and J. Furthmüller. Efficient iterative schemes for ab initio total-energy calculations using a plane-wave basis set. *Phys. Rev. B*, 1996, 54(16):11169–11186, a.

G. Kresse and J. Furthmüller. Efficiency of ab-initio total energy calculations for metals and semiconductors using a plane-wave basis set. *Comput. Mater. Sci*, 1996, 6(1):15–50, b.

G. Kresse and J. Hafner. Ab initio molecular dynamics for liquid metals. *Phys. Rev. B*, 47 (1):558–561, 1993.

F. C. Larché and J. W. Cahn. Overview no. 41 The interactions of composition and stress in crystalline solids. *Acta Metall.*, 33(3):331–357, 1985.

P. M. Larsen, S. Schmidt, and J. Schiøtz. Robust structural identification via polyhedral template matching. *Modelling Simul. Mater. Sci. Eng.*, 24(5):055007, 2016.

A. Li and I. Szlufarska. Morphology and mechanical properties of nanocrystalline Cu/Ag alloy. *J. Mater. Sci*, 52(8):4555–4567, 2017.

P. Li, S. X. Li, Z. G. Wang, and Z. F. Zhang. Fundamental factors on formation mechanism of dislocation arrangements in cyclically deformed fcc single crystals. *Prog. Mater. Sci*, 56(3):328–377, 2011.

X. Li, T. Kreuter, X. M. Luo, R. Schwaiger, and G. P. Zhang. Detecting co-deformation behavior of Cu–Au nanolayered composites. *Mater. Res. Lett.*, 5(1):20–28, 2017.

Y. P. Li and G. P. Zhang. On plasticity and fracture of nanostructured Cu/X (X=Au, Cr) multilayers: The effects of length scale and interface/boundary. *Acta Mater.*, 58(11): 3877–3887, 2010.

Y. P. Li, X. F. Zhu, J. Tan, B. Wu, W. Wang, and G. P. Zhang. Comparative investigation of strength and plastic instability in Cu/Au and Cu/Cr multilayers by indentation. *J. Mater. Res.*, 24(3):728–735, 2009.

Y. P. Li, X. F. Zhu, G. P. Zhang, J. Tan, W. Wang, and B. Wu. Investigation of deformation instability of Au/Cu multilayers by indentation. *Philos. Mag.*, 90(22):3049–3067, 2010.

X. Liu, R. Hao, S. Mao, and S. J. Dillon. Shear strengths of FCC-FCC cube-on-cube interfaces. *Scripta Mater.*, 130:178–181, 2017.

Y. Liu, D. Bufford, H. Wang, C. Sun, and X. Zhang. Mechanical properties of highly textured Cu/Ni multilayers. *Acta Mater.*, 59(5):1924–1933, 2011.

B. Luan and M. O. Robbins. The breakdown of continuum models for mechanical contacts. *Nature*, 435(7044):929–932, 2005.

Z.-P. Luo, G.-P. Zhang, and R. Schwaiger. Microstructural vortex formation during cyclic sliding of Cu/Au multilayers. *Scripta Mater.*, 107:67–70, 2015.

O. Madelung, editor. *Ac-Au – Au-Zr and Cr-Cs – Cu-Zr*, volume 5a and 5d of *Landolt-Börnstein - Group IV Physical Chemistry*. Springer-Verlag, Berlin/Heidelberg, 1991.

B. B. Mandelbrot. *The Fractal Geometry of Nature*, volume 173. WH freeman, New York, 1983.

R. M. Martin. *Electronic Structure: Basic Theory and Practical Methods*. Cambridge University Press, 2004.

E. Martínez and B. P. Uberuaga. Mobility and coalescence of stacking fault tetrahedra in Cu. *Sci. Rep.*, 5:9084, 2015.

T. B. Massalski, H. Okamoto, P. Subramanian, and L. Kacprzak. *Binary Alloy Phase Diagrams*. ASM International, Materials Park, Ohio, 1990.

I. N. Mastorakos, A. Bellou, D. F. Bahr, and H. M. Zbib. Size-dependent strength in nanolaminate metallic systems. *J. Mater. Res.*, 26(10):1179–1187, 2011.

J. W. Matthews and A. E. Blakeslee. Defects in epitaxial multilayers: I. Misfit dislocations. *J. Cryst. Growth*, 27:118–125, 1974.

A. E. Mattsson, R. Armiento, P. A. Schultz, and T. R. Mattsson. Nonequivalence of the generalized gradient approximations PBE and PW91. *Phys. Rev. B*, 73(19):195123, 2006.

M. Methfessel and A. T. Paxton. High-precision sampling for Brillouin-zone integration in metals. *Phys. Rev. B*, 40(6):3616–3621, 1989.

N. Metropolis, A. W. Rosenbluth, M. N. Rosenbluth, A. H. Teller, and E. Teller. Equation of State Calculations by Fast Computing Machines. *J. Chem. Phys.*, 21(6):1087–1092, 1953.

I. Meunier, G. Tréglia, B. Legrand, R. Tétot, B. Aufray, and J.-M. Gay. Molecular dynamics simulations for the Ag/Cu (111) system: From segregated to constitutive interfacial vacancies. *Appl. Surf. Sci.*, 162:219–226, 2000.

P. B. Mirkarimi, M. Shinn, and S. A. Barnett. An ultrahigh vacuum, magnetron sputtering system for the growth and analysis of nitride superlattices. *J. Vac. Sci. Technol. A*, 10(1): 75–81, 1992.

Y. Mishin, M. J. Mehl, D. A. Papaconstantopoulos, A. F. Voter, and J. D. Kress. Structural stability and lattice defects in copper: Ab initio, tight-binding, and embedded-atom calculations. *Phys. Rev. B*, 63(22):224106, 2001.

M. Mishra and I. Szlufarska. Analytical Model for Plowing Friction at Nanoscale. *Tribol. Lett.*, 45(3):417–426, 2012.

M. Mishra, P. Egberts, R. Bennewitz, and I. Szlufarska. Friction model for single-asperity elastic-plastic contacts. *Phys. Rev. B*, 86(4):045452, 2012.

A. Misra and H. Krug. Deformation Behavior of Nanostructured Metallic Multilayers. *Adv. Eng. Mater.*, 3(4):217–222, 2001.

A. Misra, M. Verdier, Y. C. Lu, H. Kung, T. E. Mitchell, M. Nastasi, and J. D. Embury. Structure and mechanical properties of Cu-X (X = Nb,Cr,Ni) nanolayered composites. *Scripta Mater.*, 39(4):555–560, 1998.

A. Misra, H. Kung, and J. D. Embury. Preface to the viewpoint set on: Deformation and stability of nanoscale metallic multilayers. *Scripta Mater.*, 50(6):707–710, 2004.

A. Misra, J. P. Hirth, and R. G. Hoagland. Length-scale-dependent deformation mechanisms in incoherent metallic multilayered composites. *Acta Mater.*, 53(18):4817–4824, 2005.

D. Mitlin, A. Misra, V. Radmilovic, M. Nastasi, R. Hoagland, D. J. Embury, J. P. Hirth, and T. E. Mitchell. Formation of misfit dislocations in nanoscale Ni–Cu bilayer films. *Philos. Mag.*, 84(7):719–736, 2004.

H. J. Monkhorst and J. D. Pack. Special points for Brillouin-zone integrations. *Phys. Rev. B*, 13(12):5188–5192, 1976.

J. R. Morris, C. Z. Wang, K. M. Ho, and C. T. Chan. Melting line of aluminum from simulations of coexisting phases. *Phys. Rev. B*, 49(5):3109–3115, 1994.

V. G. Myagkov, Y. N. Mikhlin, L. E. Bykova, V. K. Mal'tsev, and G. N. Bondarenko. Long-range chemical interaction in solid-state synthesis: The formation of a CuAu alloy in Au/β-Co(001)/Cu(001) epitaxial film structures. *J. Exp. Theor. Phys. Lett.*, 90(2):111–115, 2009.

J. A. Nelder and R. Mead. A Simplex Method for Function Minimization. *Comput J*, 7(4): 308–313, 1965.

E. C. Neyts and A. Bogaerts. Combining molecular dynamics with Monte Carlo simulations: Implementations and applications. *Theor. Chem. Acc.*, 132(2):1320, 2013.

W. G. Nöhring and W. A. Curtin. Thermodynamic properties of average-atom interatomic potentials for alloys. *Modelling Simul. Mater. Sci. Eng.*, 24(4):045017, 2016.

S. Ogata, J. Li, and S. Yip. Ideal Pure Shear Strength of Aluminum and Copper. *Science*, 298(5594):807–811, 2002.

V. Ozoliņš, C. Wolverton, and A. Zunger. Cu-Au, Ag-Au, Cu-Ag, and Ni-Au intermetallics: First-principles study of temperature-composition phase diagrams and structures. *Phys. Rev. B*, 57(11):6427–6443, 1998.

V. Paidar and V. Vitek. Stacking-Fault-Type Interfaces and their Role in Deformation. *Intermet. Compd. - Princ. Pract.*, 2002.

L. Palatnik and A. Il'Inskii. Stabilization of High-Strength Vacuum-Deposited Films. *Sov. Phys. Dokl.*, 9:93, 1964.

L. B. Pártay, A. P. Bartók, and G. Csányi. Efficient Sampling of Atomic Configurational Spaces. *J. Phys. Chem. B*, 114(32):10502–10512, 2010.

L. B. Pártay, A. P. Bartók, and G. Csányi. Nested sampling for materials: The case of hard spheres. *Phys. Rev. E*, 89(2):022302, 2014.

W. M. Paulson and J. E. Hilliard. Interdiffusion in composition-modulated copper-gold thin films. *J. Appl. Phys.*, 48(6):2117–2123, 1977.

A. T. Paxton. Point, line and planar defects. In *Electron Theory in Alloy Design*, pages 158–190. The Institute of Materials, London, D.G. pettifor and A.H. cottrell edition, 1992.

A. T. Paxton and Y. Q. Sun. The role of planar fault energy in the yield anomaly in L12 intermetallics. *Philos. Mag. A*, 78(1):85–104, 1998.

J. P. Perdew, J. A. Chevary, S. H. Vosko, K. A. Jackson, M. R. Pederson, D. J. Singh, and C. Fiolhais. Atoms, molecules, solids, and surfaces: Applications of the generalized gradient approximation for exchange and correlation. *Phys. Rev. B*, 46(11):6671–6687, 1992.

J. P. Perdew, K. Burke, and M. Ernzerhof. Generalized Gradient Approximation Made Simple. *Phys. Rev. Lett.*, 77(18):3865–3868, 1996.

J. P. Perdew, A. Ruzsinszky, G. I. Csonka, O. A. Vydrov, G. E. Scuseria, L. A. Constantin, X. Zhou, and K. Burke. Restoring the Density-Gradient Expansion for Exchange in Solids and Surfaces. *Phys. Rev. Lett.*, 100(13):136406, 2008.

B. N. J. Persson, O. Albohr, U. Tartaglino, A. I. Volokitin, and E. Tosatti. On the nature of surface roughness with application to contact mechanics, sealing, rubber friction and adhesion. *J. Phys.: Condens. Matter*, 17(1):R1, 2005.

N. Petch. The cleavage strength of polycrystals. *J. Iron Steel Inst.*, 174:25–28, 1953.

M. A. Phillips, B. M. Clemens, and W. D. Nix. A model for dislocation behavior during deformation of Al/Al3Sc (fcc/L12) metallic multilayers. *Acta Mater.*, 51(11):3157–3170, 2003.

J. M. Pitarke and A. G. Eguiluz. Jellium surface energy beyond the local-density approximation: Self-consistent-field calculations. *Phys. Rev. B*, 63(4):045116, 2001.

M. Pouryazdan, B. J. P. Kaus, A. Rack, A. Ershov, and H. Hahn. Mixing instabilities during shearing of metals. *Nat. Commun.*, 8(1):1611, 2017.

S. I. Rao and P. M. Hazzledine. Atomistic simulations of dislocation–interface interactions in the Cu-Ni multilayer system. *Philos. Mag. A*, 80(9):2011–2040, 2000.

R. C. Reed. *The Superalloys : Fundamentals and Applications*. Cambridge University Press, Cambridge, digital printed version edition, 2008.

T. Riedl, A. Kirchner, K. Eymann, A. Shariq, R. Schlesiger, G. Schmitz, M. Ruhnow, and B. Kieback. Elemental distribution, solute solubility and defect free volume in nanocrystalline restricted-equilibrium Cu–Ag alloys. *J. Phys.: Condens. Matter*, 25(11): 115401, 2013.

D. A. Rigney and J. P. Hirth. Plastic deformation and sliding friction of metals. *Wear*, 53(2): 345–370, 1979.

D. A. Rigney and S. Karthikeyan. The Evolution of Tribomaterial During Sliding: A Brief Introduction. *Tribol. Lett.*, 39(1):3–7, 2010.

N. M. Rosengaard and H. L. Skriver. Ab initio study of antiphase boundaries and stacking faults in L12 and DO22 compounds. *Phys. Rev. B*, 50(7):4848–4858, 1994.

B. Sadigh, P. Erhart, A. Stukowski, A. Caro, E. Martinez, and L. Zepeda-Ruiz. Scalable parallel Monte Carlo algorithm for atomistic simulations of precipitation in alloys. *Phys. Rev. B*, 85(18):184203, 2012.

T. Schneider and E. Stoll. Molecular-dynamics study of a three-dimensional one-component model for distortive phase transitions. *Phys. Rev. B*, 17(3):1302–1322, 1978.

R. Schwaiger. Private Communications. 2015.

R. Schwaiger, M. Weber, B. Moser, P. Gumbsch, and O. Kraft. Mechanical assessment of ultrafine-grained nickel by microcompression experiment and finite element simulation. *J. Mater. Res.*, 27(1):266–277, 2012.

K. O. Schweitz, J. Chevallier, J. Bøttiger, W. Matz, and N. Schell. Hardness in Ag/Ni, Au/Ni and Cu/Ni multilayers. *Philos. Mag. A*, 81(8):2021–2032, 2001.

S. Shao, J. Wang, A. Misra, and R. G. Hoagland. Spiral Patterns of Dislocations at Nodes in (111) Semi-coherent FCC Interfaces. *Sci. Rep.*, 3:2448, 2013.

S. Shao, J. Wang, I. J. Beyerlein, and A. Misra. Glide dislocation nucleation from dislocation nodes at semi-coherent $\{111\}$ Cu–Ni interfaces. *Acta Mater.*, 98:206–220, 2015.

F. Shimizu, S. Ogata, and J. Li. Theory of Shear Banding in Metallic Glasses and Molecular Dynamics Calculations. *Mater. Trans.*, 48(11):2923–2927, 2007.

W. Shinoda, M. Shiga, and M. Mikami. Rapid estimation of elastic constants by molecular dynamics simulation under constant stress. *Phys. Rev. B*, 69(13):134103, 2004.

G. Simmons, H. Wang, et al. *Single Crystal Elastic Constants and Calculated Aggregate Properties*. Mass., M.I.T. Press, Cambridge, 1971.

J. Skilling. Nested Sampling. *AIP Conf. Proc.*, 735(1):395–405, 2004.

J. Skilling. Nested sampling for general Bayesian computation. *Bayesian Anal.*, 1(4): 833–859, 2006.

D. O. Smith, M. S. Cohen, and G. P. Weiss. Oblique-Incidence Anisotropy in Evaporated Permalloy Films. *J. Appl. Phys.*, 31(10):1755–1762, 1960.

R. W. Smith and G. S. Was. Application of molecular dynamics to the study of hydrogen embrittlement in Ni-Cr-Fe alloys. *Phys. Rev. B*, 40(15):10322–10336, 1989.

J. Solca, A. J. Dyson, G. Steinebrunner, B. Kirchner, and H. Huber. Melting curve for argon calculated from pure theory. *Chem. Phys.*, 224(2):253–261, 1997.

D. J. Srolovitz, S. M. Yalisove, and J. C. Bilello. Design of multiscalar metallic multilayer composites for high strength, high toughness, and low CTE mismatch. *Metall. Mater. Trans. A*, 26(7):1805–1813, 1995.

A. Stukowski. Visualization and analysis of atomistic simulation data with OVITO–the Open Visualization Tool. *Modelling Simul. Mater. Sci. Eng.*, 18(1):015012, 2010.

A. Stukowski. Structure identification methods for atomistic simulations of crystalline materials. *Modelling Simul. Mater. Sci. Eng.*, 20(4):045021, 2012.

A. Stukowski, V. V. Bulatov, and A. Arsenlis. Automated identification and indexing of dislocations in crystal interfaces. *Modelling Simul. Mater. Sci. Eng.*, 20(8):085007, 2012.

P. R. Subramanian and J. H. Perepezko. The ag-cu (silver-copper) system. *J. Phase Equilibria*, 14(1):62–75, 1993.

N. K. Sundaram, Y. Guo, and S. Chandrasekar. Mesoscale Folding, Instability, and Disruption of Laminar Flow in Metal Surfaces. *Phys. Rev. Lett.*, 109(10):106001, 2012.

J. C. W. Swart, P. van Helden, and E. van Steen. Surface Energy Estimation of Catalytically Relevant fcc Transition Metals Using DFT Calculations on Nanorods. *J. Phys. Chem. C*, 111(13):4998–5005, 2007.

I. Szlufarska, M. Chandross, and R. W. Carpick. Recent advances in single-asperity nanotribology. *J. Phys. D: Appl. Phys.*, 41(12):123001, 2008.

J. Tersoff. New empirical approach for the structure and energy of covalent systems. *Phys. Rev. B*, 37(12):6991–7000, 1988.

A. P. Thompson, S. J. Plimpton, and W. Mattson. General formulation of pressure and stress tensor for arbitrary many-body interaction potentials under periodic boundary conditions. *J. Chem. Phys.*, 131(15):154107, 2009.

S. A. Thorpe. Experiments on the instability of stratified shear flows: Miscible fluids. *J. Fluid Mech.*, 46(2):299–319, 1971.

D. Tománek, A. A. Aligia, and C. A. Balseiro. Calculation of elastic strain and electronic effects on surface segregation. *Phys. Rev. B*, 32(8):5051–5056, 1985.

K. N. Tu and B. S. Berry. X-ray study of interdiffusion in bimetallic Cu–Au films. *J. Appl. Phys.*, 43(8):3283–3290, 1972.

W. R. Tyson and W. A. Miller. Surface free energies of solid metals: Estimation from liquid surface tension measurements. *Surf. Sci.*, 62(1):267–276, 1977.

C. Varvenne, A. Luque, W. G. Nöhring, and W. A. Curtin. Average-atom interatomic potential for random alloys. *Phys. Rev. B*, 93(10):104201, 2016.

R. Venkatraman and J. C. Bravman. Separation of film thickness and grain boundary strengthening effects in Al thin films on Si. *J. Mater. Res.*, 7(8):2040–2048, 1992.

V. Vítek. Intrinsic stacking faults in body-centred cubic crystals. *Philos. Mag. J. Theor. Exp. Appl. Phys.*, 18(154):773–786, 1968.

G. Voronoi. Nouvelles applications des paramètres continus à la théorie des formes quadratiques. Deuxième mémoire. Recherches sur les parallélloèdres primitifs. *J. Für Reine Angew. Math.*, 134:198–287, 1908.

A. F. Voter and S. P. Chen. Accurate Interatomic Potentials for Ni, Al and Ni3Al. *MRS Online Proc. Libr. Arch.*, 82, 1986.

F. Wang, P. Huang, M. Xu, T. J. Lu, and K. W. Xu. Shear banding deformation in Cu/Ta nano-multilayers. *Mater. Sci. Eng. A*, 528(24):7290–7294, 2011.

G.-S. Wang, E. K. Delczeg-Czirjak, Q.-M. Hu, K. Kokko, B. Johansson, and Levente Vitos. The effect of long-range order on the elastic properties of Cu3Au. *J. Phys.: Condens. Matter*, 25(8):085401, 2013.

J. Wang and A. Misra. An overview of interface-dominated deformation mechanisms in metallic multilayers. *Curr. Opin. Solid State Mater. Sci.*, 15(1):20–28, 2011.

J. Wang, R. G. Hoagland, J. P. Hirth, and A. Misra. Atomistic simulations of the shear strength and sliding mechanisms of copper–niobium interfaces. *Acta Mater.*, 56(13): 3109–3119, 2008.

G. S. Was and T. Foecke. Deformation and fracture in microlaminates. *Thin Solid Films*, 286(1):1–31, 1996.

Q. Wei, D. Jia, K. T. Ramesh, and E. Ma. Evolution and microstructure of shear bands in nanostructured Fe. *Appl. Phys. Lett.*, 81(7):1240–1242, 2002.

X.-Z. Wu, R. Wang, S.-F. Wang, and Q.-Y. Wei. Ab initio calculations of generalized-stacking-fault energy surfaces and surface energies for FCC metals. *Appl. Surf. Sci.*, 256 (21):6345–6349, 2010.

H. Xie, T. Yu, and F. Yin. Tension–compression asymmetry in homogeneous dislocation nucleation stress of single crystals Cu, Au, Ni and Ni3Al. *Mater. Sci. Eng. A*, 604:142–147, 2014.

V. Yamakov, D. Wolf, M. Salazar, S. R. Phillpot, and H. Gleiter. Length-scale effects in the nucleation of extended dislocations in nanocrystalline Al by molecular-dynamics simulation. *Acta Mater.*, 49(14):2713–2722, 2001.

J. W. Yan and G. P. Zhang. Revealing the tunable twinning/detwinning behavior in 25 nm Cu/Au multilayers. *Appl. Phys. Lett.*, 102(21):211905, 2013.

J. W. Yan, G. P. Zhang, X. F. Zhu, H. S. Liu, and C. Yan. Microstructures and strengthening mechanisms of Cu/Ni/W nanolayered composites. *Philos. Mag.*, 2013, 93(5):434–448, a.

J. W. Yan, X. F. Zhu, G. P. Zhang, and C. Yan. Evaluation of plastic deformation ability of Cu/Ni/W metallic multilayers. *Thin Solid Films*, 2013, 527:227–231, b.

Z. Yan, J. P. Perdew, and S. Kurth. Density functional for short-range correlation: Accuracy of the random-phase approximation for isoelectronic energy changes. *Phys. Rev. B*, 61 (24):16430–16439, 2000.

L. Yuan, Z. Xu, D. Shan, and B. Guo. Molecular dynamics study on the equal biaxial tension of Cu/Ag bilayer films. *Appl. Surf. Sci.*, 282:450–455, 2013.

L. A. Zepeda-Ruiz, A. Stukowski, T. Oppelstrup, and V. V. Bulatov. Probing the limits of metal plasticity with molecular dynamics simulations. *Nature*, 550(7677):492–495, 2017.

G. P. Zhang. Private Communications. 2014.

J. Y. Zhang, J. Li, X. Q. Liang, G. Liu, and J. Sun. Achieving optimum mechanical performance in metallic nanolayered Cu/X (X = Zr, Cr) micropillars. *Sci. Rep.*, 4:4205, 2014.

R. F. Zhang, I. J. Beyerlein, S. J. Zheng, S. H. Zhang, A. Stukowski, and T. C. Germann. Manipulating dislocation nucleation and shear resistance of bimetal interfaces by atomic steps. *Acta Mater.*, 113:194–205, 2016.

X. Zhang, J. Han, J. J. Plombon, A. P. Sutton, D. J. Srolovitz, and J. J. Boland. Nanocrystalline copper films are never flat. *Science*, 357(6349):397–400, 2017.

Y. Zhang and E. J. Maginn. A comparison of methods for melting point calculation using molecular dynamics simulations. *J. Chem. Phys.*, 136(14):144116, 2012.

X. W. Zhou, R. A. Johnson, and H. N. G. Wadley. Misfit-energy-increasing dislocations in vapor-deposited CoFe/NiFe multilayers. *Phys. Rev. B*, 69(14):144113, 2004.

J. A. Zimmerman, H. Gao, and F. F. Abraham. Generalized stacking fault energies for embedded atom FCC metals. *Modelling Simul. Mater. Sci. Eng.*, 8(2):103, 2000.